Supporting Information for

Titan's Global Radiant Energy Budget During the Cassini Epoch (2004-2017)

Ellen C. Creecy[1], Liming Li[2*], Xun. Jiang[1], Robert A. West[3], Patrick. M. Fry[4], Conor A. Nixon[5], Matthew E. Kenyon[3], Benoît Seignovert[6]

[1] Department of Earth and Atmospheric Sciences, University of Houston, Houston, TX, 77004.

[2] Department of Physics, University of Houston, Houston, TX, 77004.

[3] Jet Propulsion Laboratory, California Institute of Technology, Pasadena, CA, 91109.

[4] Space Science and Engineering Center, University of Wisconsin-Madison, Madison, WI, 53706.

[5] NASA Goddard Space Flight Center, Greenbelt, MD, 20771.

[6] Université de Nantes, Univ Angers, CNRS, LPG, UMR 6112, F-44000 Nantes, France

*To whom all correspondence should be addressed. E-mail: lli7@central.uh.edu

Contents of this file

1. Text S1 to S11
2. Figures S1 to S48
3. Table S1

S1. Theoretical Methodology

To determine the radiant energy budget for a planet or a moon, we have to measure the absorbed solar energy and the emitted thermal energy (Conrath et al., 1989). We have estimated Titan's emitted thermal energy with the observations recorded by the Cassini Composite Infrared Spectrometer (Creecy et al., 2019). In this study, we focus on measuring Titan's absorbed solar energy with the observations obtained by the Cassini Imaging Science Sub-system and Visual and Infrared Mapping Spectrometer. The methodology of computing the absorbed solar energy is provided in some previous studies (Conrath et al., 1989), and discussed in detail in one of our previous studies (Li et al., 2018). Here, we briefly introduce the main idea of the methodology. Generally, we measure the reflected solar energy and then subtract the reflected solar energy from the total solar energy to get the absorbed solar energy. The key parameter of computing the reflected solar energy is the Bond albedo A. The Bond albedo at each wavelength is called the monochromatic Bond albedo (A_m). It is defined as $A_m = A_0 q$, where A_0 and q are the monochromatic geometric albedo and the monochromatic phase integral, respectively. The monochromatic geometric albedo A_0 is defined as the full-disk albedo at 0° phase angle for a given wavelength. The phase integral q is the integral of the reflected solar irradiance over phase angle (Li et al., 2018). Once the monochromatic Bond albedo A_m at each wavelength is measured, we can compute the Bond albedo A for a planet or a moon by weighting the monochromatic Bond albedo with the solar spectral irradiance (see sections as below).

S2. Summary of Observational Data Sets

Based on the methodology we discussed in "Methods", we know the monochromatic Bond albedo (A_m) is computed by the product of the monochromatic geometric albedo (A_0) and the monochromatic phase integral (q). Both qualities are related to the ratios between the reflected solar irradiance and the incoming solar irradiance at each wavelength. Therefore, the incoming solar irradiance at each wavelength, which is also named as the solar spectral irradiance (SSI), provides the reference for computing the monochromatic Bond albedo. In this study, we also investigate the temporal variations of Titan's Bond albedo and the radiant energy budget during the Cassini epoch (2004-2017). So the first data set is the time-varying SSI for the Cassini epoch. To compute the total reflected solar irradiance, we need integrate the reflected solar irradiance over the phase angle from 0° to 180° (i.e., phase function or phase integral). The observations of phase function and the reflected spectra are mainly provided by the Cassini Imaging Science Subsystem (ISS) (14) and the Visual and Infrared Mapping Spectrometer (VIMS) (15). The Cassini ISS and VIMS do not cover the complete wavelength range from 0 nm to 6000 nm, so we need observations of the reflected spectra at these wavelengths outside the Cassini wavelengths. These observations not only help fill the observational gaps in wavelength but also help validate the Cassini ISS and VIMS observations. The observations of the reflected spectra, which come from the Cassini ISS and VIMS observations and the other observations, are defined as the spectral observations. The albedo spectra in the wavelength range 150-190 nm come from the Cassini Ultraviolet Imaging Spectrograph (UVIS) observations (Esposito et al., 2004; Ajello et al., 2008). The Faint Object Spectrograph (FOS) of the Hubble Space Telescope (HST) and the European Southern Observatory (ESO) also provide albedo spectra of Titan (Karkoschka, 1994, 1998; McGrath et al., 1998).

For the phase function of Titan's albedo, the Imaging Photopolarimeter (IPP) on the spacecraft Pioneer 11 conducted the first observations (Tomasko and Smith, 1982). The coverage of phase angle is better for the Cassini ISS/VIMS observations than for Pioneer 11 observations, but the latter can help validate the Cassini observations. Table S1 in the Supporting Information summarizes the data sets for the SSI, the phase integral, and the spectral observations. These data sets are discussed in detail in following sections.

S3. Solar Spectral Irradiance Data

The Solar Spectral Irradiance (SSI) provides a base for computing Titan's albedo and hence the reflected/absorbed solar power at each wavelength. The SSI from 0 to 6000 nm contributes to ~ 99.7% of the total solar power, so we construct the SSI in the wavelength range 0-6000 nm. The SEE, SORCE, and ASTM are three data sets used for the solar spectral irradiance (SSI). They are the Solar EUV Experiment (SEE) (http://lasp.colorado.edu/lisird/data/timed_see_ssi_l3a/), the

Solar Radiation and Climate Experiment (SORCE) (http://lasp.colorado.edu/lisird/data/sorce_ssi_l3/), and the American Society for Testing and Materials (ASTM) (https://www.nrel.gov/grid/solar-resource/spectra-am1.5.html), respectively. We do not find trustable data sets for the SSI in the wavelength range 4000-6000 nm, so we compute it by assuming the blackbody spectra for the Sun with a temperature 5778 K.

It should be mentioned that the longest wavelength of VIMS is 5131 nm, so our analyses of Titan's albedo is mainly in the wavelength range 0-5131 nm, which contains more than 99.5% of the total solar power. The total solar power varies ~ 0.1% on the time scale of decades (Willson and Mordvinov, 2003; Lean and Rind, 2009) (also see Fig. S1), but the SSI at some wavelengths can vary with much larger magnitudes. Therefore, it is better to resolve the temporal variations of the SSI. We construct the SSI in the wavelength range 0-6000 nm for the Cassini epoch (2004-2017) from different data sets (see Table S1) listed in Fig. S1. Figure S1 shows both the SSI (panel A) and the total solar power at Earth (i.e., solar constant) (panel B) by integrating the SSI over wavelength.

Based on the constructed SSI at Earth (Fig. S1), we can compute the SSI at Titan (panel A of Fig. S2) with the distance between the Sun and Titan (panel B of Fig. S2). The distance between the Sun and Titan during the period of 2004-2017 (panel B) comes from the NASA/JPL solar system dynamics – the Horizons Web-interface (https://ssd.jpl.nasa.gov/horizons.cgi). In addition, the total solar power at Titan (i.e., solar flux), which is computed by integrating the SSI (panel A) over wavelength, is shown in panel C. The SSI at Titan is used for the computation of Titan's albedo.

S4. Supplementary Observations and Data

As shown in Table S1, there are observations different from the Cassini ISS and VIMS observations (i.e., Supplementary Observations), which can help to validate the Cassini ISS and VIMS measurements and fill the observational gaps in wavelengths. There are many observations of Titan's albedo spectra in different wavelengths and times. Here, we select the best available observations. The first observations come from the ESO (Karkoschka, 1994, 1998), one of the best observations of Titan's albedo spectra cover the wavelengths from ~ 305 nm to 1050 nm with a very high spectral resolution (~ 0.4 nm). Two data sets from the ESO are used: one is the albedo spectra at a phase angle 2.7° in 1993 and the other is the albedo spectra at a phase 5.7° in 1995. The two spectra are shown in Fig. S3.

The shortest effective wavelength of the ESO observations is about 305 nm, so we also searched for albedo spectra with wavelengths less than 305 nm. Two data sets are used: one comes from the Cassini UVIS (Esposito et al., 2004) and the other comes from HST/FOS (McGrath et al., 1998). Based on the observations from the Cassini UVIS and the HST/FOS, the studies by Ajello et al. (2008) and McGrath et al. (1998) provide the albedo spectra in the wavelength ranges of 150-190 nm and 190-305 nm, respectively. We are unable to locate good data sets for the albedo spectra in the wavelength range 0-150 nm, so we assume that the albedo spectra in this wavelength range are the same as that at 150 nm.

There are very limited observations for the phase function of Titan's albedo mainly because the Earth-based observations cover a very narrow range of phase angle. To the best of our knowledge, the only good measurements of the phase function of Titan's albedo aside from Cassini were conducted by the IPP on Pioneer 11 (Tomasko and Smith, 1982). Compared to the Cassini observations, the coverage of phase angle by the Pioneer 11 observations are quite limited, but they are the best observations for the phase function of Titan's albedo before the Cassini epoch.

The IPP on the spacecraft Pioneer 11 conducted measurements of Titan’s albedo in two wavelengths (452 nm (blue) and 648 (red)) with phase angles varying from 21.9° to 95.9°. The Pioneer 11/IPP measurements, which have been described in a previous study (Tomasko and Smith, 1982), are shown in Fig. S5.

S5. Cassini ISS/VIMS Data and Data Processing

The Cassini spacecraft conducted on-orbit observations of the Saturn system from October 2004 to September 2017. During this period, there are many observations of Titan with multiple flybys. In this study, we mainly analyze the observations of Titan’s reflected solar irradiance from two Cassini instruments: ISS and VIMS. The observations recorded by the Cassini ISS and VIMS have many improvements than the previous observations, which have been discussed in our previous studies (Li et al., 2010, 2011, 2018; Creecy et al., 2019). Therefore, our analyses of Titan’s Bond albedo, which are based on the Cassini observations, represent the best existing measurements of Titan’s Bond albedo. The measurements of Titan’s Bond albedo are combined with our previous measurements of Titan’s emitted power (Creecy et al., 2019) with the observations from the Cassini Composite Infrared Spectrometer (CIRS) (Flasar et al., 2004) to provide the first precise measurements of Titan’s global radiant energy budget. More importantly, the long-term Cassini observations from 2004 to 2017 make it possible to investigate the temporal variations of Titan’s radiant energy budget and examine the possible energy imbalance for the first time.

Here, we briefly introduce the two Cassini instruments (i.e., ISS and VIMS), which are used to measure Titan’s Bond albedo for the Cassini epoch. As the imaging system of the Cassini spacecraft, the ISS is a Charged-Coupled Device with two cameras (one is the narrow-angle camera and the other is the wide-angle camera) (Porco et al., 2004). The characteristics of the ISS instrument and the related data processing (e.g., calibrating and navigating) are described in previous studies (Porco et al., 2004; Li et al., 2018). The ISS has multiple filters (i.e., wavelengths) ranging from the ultraviolet to the near infrared. Here we mainly use the 12 filters with a wavelength range from 264 nm to 939 nm, which were summarized in our previous study of Jupiter’s radiant energy budget and internal heat (Li et al., 2018), to compute the full-disk albedo of Titan. The basic characteristics of 12 filters (three ultraviolet filters “UV1”, “UV2”, and “UV3”; three methane-absorption filters “MT1”, “MT2”, and “MT3”; the three continuum filters “CB1”, “CB2”, and “CB3”; and the three color filters “BL1”, “GRN”, and “RED”) are introduced in the ISS introductory paper (Porco et al., 2004) and summarized in our previous study of Jupiter (Li et al., 2018).

To compute Titan’s full-disk albedo, we searched for the global images of Titan from the complete ISS data set (https://pds-imaging.jpl.nasa.gov/volumes/iss.html). We selected the ISS global images with spatial resolutions from ~ 6 km/pixel to ~ 200 km/pixel, which resolve Titan well, to conduct the measurements. The corresponding phase angles vary from ~ 0° to ~167°, which are the best among all available observations. There are observational gaps in phase angle even with the Cassini ISS observations, so the least-squares method is used to fill the observational gaps in phase angle (see section “Filling Observational Gaps in Phase Angle”).

After collecting the raw ISS global images, we calibrated the recorded digital number of brightness to radiance using the latest version of the Cassini ISS CALibration software (https://pds-imaging.jpl.nasa.gov/data/cassini/cassini_orbiter/coiss_0011_v4.3/), which was developed by the ISS team (West et al., 2010; Knowles et al., 2020). An example of such calibration is presented in Fig. S6. The radiance at each pixel of the global images is multiplied by the area of the pixel, and summed over all pixels in Titan's disk with an effective radius (see section "Effective Radii of Titan's Atmosphere") to get the observed full-disk reflected solar irradiance. At the same time, the reference SSI (Fig S2) is multiplied by the total area of Titan's disk with the effective radius to get the reference full-disk solar irradiance. Then the ratio between the observed full-disk solar irradiance and the reference full-disk solar irradiance is taken as the full-disk albedo (i.e., I/F).

The Cassini ISS observations have the best coverage of phase angle, but they focus on limited wavelengths only. On the other hand, the Cassini VIMS instrument is a spectral camera that takes images in 352 wavelengths between ~350 nm and ~5130 nm with varying spectral resolutions from ~ 4 nm to ~ 25 nm (Brown et al., 2004). The VIMS observations can help extend the spectral coverage of the ISS observations. The raw global VIMS images, which are available on the PDS system (https://pds-imaging.jpl.nasa.gov/volumes/vims.html), are well calibrated by the VIMS Operations Team (Brown et al., 2004; McCord et al., 2004; Filacchione et al., 2007; Buratti et al., 2010; Pitman et al., 2010).

For the wavelengths covered by the Cassini ISS observations (~ 264-939 nm), the reflected solar irradiance is dominant over the emitted thermal radiance in the recorded radiance, so the emitted thermal radiance from Titan can be neglected in the ISS recorded radiance. When the wavelength increases, the emitted thermal radiance becomes stronger, even though it is still much smaller than the reflected solar irradiance (even at the longest VIMS wavelength 5131 nm). However, it is more accurate to consider the emitted thermal radiance when computing Titan's albedo in the relatively long infrared wavelengths covered by the VIMS observations. Based on the incident solar angle, we divide each VIMS global image into the day-side and night-side parts (see examples in Fig. S7). The radiance recorded by the night-side part is mainly from the thermal emission, and the radiance recorded by the day-side part includes both the reflected solar irradiance and the thermal emission. In order to precisely measure the reflected solar irradiance and hence full-disk albedo, we subtract the night-side thermal emission from the day-side radiance to get the reflected solar irradiance.

The spatial resolutions are generally much lower for the VIMS images than for the ISS images. Here, we select the VIMS global images with spatial resolutions better than 210 km/pixel. The coverage of phase angle is also much more sparse for the VIMS observations than for the ISS observations. We searched the complete data set of the VIMS observations and found high-quality global observations at ~11 phase angles only (see section "Filling Observational Gaps in Phase Angle" and Fig. S23). The selected VIMS observations are used to address the phase functions of Titan's albedo in the wavelength range 350-5131 nm. But these VIMS observations are distributed in different years of the Cassini era, so they cannot resolve temporal variations of the phase function of Titan's albedo. The temporal variations of the phase function observed at the ISS wavelengths were extrapolated to these VIMS wavelengths outside of the ISS wavelengths (936-5131 nm) (see section "Filling Observational Gaps in Wavelength and Time").

The Cassini spacecraft has one more instrument observing the reflected solar irradiance of Titan - the UVIS (39). The UVIS was used to observe Titan at the wavelengths (56 - 190 nm), which are shorter than the wavelengths covered by the ISS and VIMS. The UVIS team has already generated Titan's full-disk geometric albedo in the wavelength range 150-190 nm (Ajello et al., 2008), which is used in this study (see Fig. S4 in the Supplementary Information 4). There are some difficulties in retrieving Titan's albedo in the wavelength range 56-150 nm with the UVIS observations (Ajello et al., 2008). In addition, the SSI in the wavelength range 56-150 nm occupies only ~ 0.006% of the total solar irradiance. So the UVIS-retrieved albedo in the wavelength range 56-150 nm are not analyzed in this study. Instead, we simply assume that Titan's albedo in the wavelength range 0-150 nm is the same as that at 150 nm (see section “Filling Observational Gaps in Wavelength and Time”).

S6. Effective Radii of Titan’s Atmosphere

Titan’s thick atmosphere extends to a few hundred kilometers, which is not negligible compared to its solid body radius ~ 2575 km (Zebker et al., 2009). Therefore, Titan’s optical radius in which the solar irradiance is effectively absorbed and reflected (i.e., effective radius) is generally larger than its solid radius. In this section, we discuss the effective radius, which varies with wavelength. We follow the method from a previous study (Smith, 1980), in which the edge of the optical disk corresponds to the maximal radiance contrast. We therefore compute the gradient of the calibrated radiance around the boundary of Titan’s optical disk and search for the maximal and minimal radiance gradients. The pixel positions with the maximal and minimal radiance gradients are used to locate the left and right edges of the optical disk, respectively.

We first test this idea with Cassini observations of Enceladus. For Enceladus, its effective radius should be equal to its solid surface because this moon does not have a visible atmosphere. We first select two lines around the boundaries of the optical disk (i.e., two horizontal solid lines in panel A of Fig. S8), which are along the equator of Enceladus. The calibrated radiances for the pixels in the two lines are plotted in panel B of Fig. S8. The gradients of the radiance along the two solid lines are presented in panel C. Then we can determine the pixel location of the maximal gradient of the line around the left boundary (i.e., the location of the left edge of the optical disk) and the pixel location of the minimal gradient of the line around the right boundary (i.e., the location of the left edge of the optical disk). The left and right edges are shown by the two vertical dashed lines respectively in panel A of Fig. S8. The distance between the two edges (i.e., the product of the pixel number between the two edges and the spatial resolution) is used to determine the diameter of the optical disk, and half of the diameter is the effective radius.

For the estimate of the error bar in determining the effective radius by the radiant gradient, we simply assume there is one-pixel uncertainty in such a method. So we can use the size corresponding to one pixel (i.e., spatial resolution) to estimate the error bar of the effective radius. Based on the analysis shown in Fig. S8, we have the effective radius of Enceladus is 253.8±2.6 km, which is consistent with the solid radius of Eaceladus 252.1±0.2 km (Thomas, 2010). This test validates the method of the maximal/minimal radiance gradient works for determining the effective radius of moons.

After the validation, we apply the method to the global images recorded by the ISS 12 filters. We try the global ISS images at both low and high phase angles. The inter-comparison of the comparisons between the low and high phase angles can be used to double check the results. Examples of determining the effective radius are demonstrated with ISS images recorded by the red filter. The analyses of the observations at the low and high phase angles are shown in Fig. S9 and Fig. S10, respectively. The analyses based on the observations at a (Fig. S9) generate an effective radius 2849.0±10.8 km, which is basically consistent with the effective radius 2857.9±12.4 km from the analyses from the observations at a high phase angle (Fig. S10).

We also test the temporal variations of the effective radius. Among the global images recorded by the ISS 12 filters, the largest number of images were recorded by the CB3 filter. Therefore we searched for the highest-quality global images of Titan recorded by the CB3 filter in different years to examine the temporal variations of its effective radius. Panels A, B, and C in Fig. S11 show the global images recorded by the CB3 filter in 2004, 2009, and 2016, respectively. The effective radii in the three years are displayed in panel D of Fig. S11. We can see the effective radius at the CB3 wavelength is basically constant with time.

Titan's effective radii at the wavelengths covered by the ISS 12 filters are shown in Fig. S12. Panel A shows that the differences of effective radius between the low and high phase angles are smaller than the error bars, which suggests that the results based on the low and high phase angles are consistent. The analyses at both low and high phase angles show that the effective radius decreases with wavelength except for small oscillations at some wavelengths. The effective radii averaged over the analyses at the low and high phase angles are shown in panel B of Fig. S12.

We also validate the effective radii measured from the Cassini/ISS observations with some previous studies. Based on the Pioneer observations, Smith (1980) measured Titan's effective radii at the blue (440 nm) and red (640 nm) wavelengths. There are also some theoretical investigations of Titan's effective radii (55-57). With a model study, Toon et al. (1992) suggested a formula to estimate the effective radii at visible wavelengths. In panel A of Fig. S13, we compare the Cassini results with the two previous studies. First, the Cassini ISS results are basically consistent with the Pioneer IPP results (i.e., the differences between them are smaller than the error bars of measurements). The trend of decreasing effective radius with wavelength, which is shown by the ISS observations, is also consistent with the results from the model study (Toon et al., 1992). In panel B of Fig. S13, we further compute the ratio of the difference between the ISS results and the previous results over the ISS results. We find that the ratio is smaller than 3%, which also suggests that the Cassini ISS results are approximately consistent with the previous results.

The Cassini ISS multi-filter observations cover limited wavelengths only, so we have to use the VIMS observations to determine Titan's effective radii in more wavelengths. Generally, the spatial resolution in the radial direction is much better for the VIMS solar-occultation observations (Maltagliati et al., 2015; Cours et al., 2020) than for the VIMS direct observations of Titan at low and high phase angles. The glow of Titan's atmosphere in some wavelengths (e.g., 3200-3500 nm) can reach ~ 700 km in the VIMS images of Titan (Baines et al., 2005), which makes the method of determining the effective radius by the radiance gradient based on the VIMS images of Titan at low and high phase angles does not work. Therefore, the VIMS solar-occultation observations are used to determine the effective radii in the longer wavelengths.

The solar-occultation observations were performed by the infrared part of the VIMS instrument (~ 884-5000 nm) only, so there are no data acquired in the visible wavelengths during the solar-occultation observations. The solar-occultation can help us determine the cross section of Titan's atmospheric extinction (Maltogliati et al., 2015; Cours et al., 2020), and the cross section is used to determine the effective radius. Four solar-occultation observations are used in our measurements of the effective radii in the infrared wavelengths, and we average the four measurements to get the effective radii in the VIMS infrared wavelengths (see Fig. S14). In the radial direction, the spatial resolutions change from 7 km to 15 km for the four solar-occultation observations (Maltagliati et al., 2015). Such spatial resolutions are comparable to the standard deviation of the four measurements of effective radius (~ 5-20 km). We combine the spatial resolution of observations and the standard deviation of measurements to represent the uncertainties of the VIMS measurements of effective radii. It should be mentioned that the standard deviation of the VIMS measurements of Titan's effective radius is probably related to the spatio-temporal variations of Titan's atmospheric processes (e.g., haze) (West et al., 2018, Seignovert et al., 2021). The uncertainties of the VIMS measurements of Titan's effective radius, which includes the possible spatio-temporal variations, are accounted in the analysis of Titan's Bond albedo and hence the absorbed solar energy. Figure S15 further compares the effective radii between the ISS and VIMS measurements. The differences between the ISS and VIMS measurements are smaller than the error bars of the VIMS measurements, which suggests that they are basically consistent.

S7. Validation of Cassini ISS and VIMS Results

After determining Titan's effective radii by the ISS and VIMS observations (Figs S12 and S14), we can calculate Titan's full-disk albedo by integrating the calibrated radiance over the disks with the effective radii in these wavelengths covered by the ISS and VIMS (see section "Cassini ISS/VIMS Data and Data Processing"). To validate the full-disk albedo computed from the ISS and VIMS observations, we first made an inter-comparison between the ISS and VIMS results. Then we compared the ISS and VIMS results with other studies.

Figure S16 shows the comparison of Titan's full-disk albedo between the ISS and VIMS observations. Only 10 ISS filters are displayed in this figure because the wavelengths of the UV1 and UV2 filters are outside of the VIMS wavelength range. The VIMS observations dispersed in different years of the Cassini epoch, and it is difficult to find a simultaneous ISS observation for each VIMS observation. Titan's full albedo, based on all available ISS and VIMS observations during the Cassini epoch, is displayed in Fig. S16. Both the ISS and VIMS observations show that Titan's albedo decreases from phase angle 0° to ~ 100-140° then increases from phase angle ~ 100-140° to ~ 160°. The increase of albedo at the high phase angles is due to the efficient forward scattering of sunlight by Titan's thick atmosphere (Garcia Munoz et al., 2017). Figure S16 demonstrates that the ISS and VIMS measurements of Titan's full-disk albedo are consistent.

The spacecraft Pioneer 11 conducted observations of Titan's full-disk at the blue (440 nm) and red wavelengths with phase angle varying from 21.9° to 95.9°. The range of phase angle from the Pioneer 11 observations are less than that of the Cassini ISS observations (0-167°), but the Pioneer 11 observations are the best in coverage of phase angle before the Cassini epoch. Here, we compare the Pioneer 11 observations at blue and red wavelengths[46] with the Cassini ISS and VIMS observations at the corresponding wavelengths (Fig. S17). The Cassini blue (459 nm) and red (648 nm) filters have slightly different wavelengths from the blue and red wavelengths of the Pioneer 11. Figure S17 shows that the differences between the Cassini and Pioneer measurements are smaller than the uncertainties in the Pioneer measurements, which suggests that the Cassini measurements are consistent with the Pioneer measurements.

The Pioneer observations have the best coverage of phase angle among the observations before the Cassini epoch, but the Pioneer observations are limited to two wavelengths (blue and red). The Earth-based ESO provide high-spectral-resolution (~ 0.4 nm) measurements of Titan's full-disk albedo in a relatively wide wavelength range (305-1050 nm) (Karkoschka, 1994, 1998). The geometry of Earth-Sun-Titan makes the phase angles of the Earth-based observations vary in a very narrow range. For the measurements conducted in 1993 and 1995 (Karkoschka, 1994, 1998), the phase angles are 2.7° and 5.7°, respectively. Here we use the ESO observations in 1995 (Karkoschka, 1998) because the observational time is closer to the Cassini epoch. The ISS UV1 filter (~ 264 nm) has the wavelength shorter than the low limit the ESO wavelength range (~305 nm). To validate the ISS UV1 measurements, the observations recorded by the FOS on the HST, which cover the wavelength 264 nm, are used. As shown in Fig. S18, the comparisons between the Cassini ISS measurements and the other measurements suggest that they are basically consistent.

The Cassini ISS observations cover limited wavelengths, but the Cassini VIMS observations have much better coverage of wavelength. So we also compare the spectral lines between the VIMS observations and the ESO observations. The VIMS observations do not have high-quality global images at phase angle less than 11.7°. Here, we compare the ESO observations with the VIMS observations at a phase angle 11.7°, which is the closest to the phase angle 5.7° for the ESO observations in 1995. Figure S19 shows the two spectra, which suggests that the ESO spectra and the VIMS spectra have the same spectral structures. However, there are significant differences between the two spectra, which can be explained by the different phase angles between them (5.7° for the ESO spectra and 11.7° for the VIMS spectra). In addition, the spectral resolution is much worse in the VIMS observations (~ 4-25 nm) than in the ESO observations (~ 0.4 nm). Therefore, the VIMS observations cannot resolve some fine spectral structures, which are revealed by the ESO high-spectral-resolution observations.

S8. Filling Observational Gaps in Phase Angle

In this study, we want to examine the temporal variations of Titan's Bond albedo and hence the reflected/absorbed solar power during the Cassini epoch. Such examinations are further combined with our previous measurements of the temporal variations of Titan's emitted power (Creecy et al., 2019) to determine the temporal variations of Titan's radiant energy budget. We first organize the ISS observations by time. In addition, the computation of Bond albedo requires the observations at different phase angles (Li et al., 2018). Therefore, the computed full-disk albedo is organized over time and phase angle. Figure S20 displays the organized full-disk albedo from the ISS observations in the two-dimensional domain of time and phase angle.

Figure S20 suggests that there are observational gaps in phase angle and such observational gaps vary from year to year. We use the least-squares fitting (Bevington and Robinson, 2003) to fill the observational gaps in phase angle. In our study of Jupiter's Bond albedo, we tried different functions (Li et al., 2018) to fit the phase function of Jupiter's full-disk albedo and we concluded that the polynomial functions of phase angle work well for fitting the phase function. Here, we try different polynomial functions to fit Titan's data, and we find a six-order polynomial function $P(\phi) = c_1\phi^6 + c_2\phi^5 + c_3\phi^4 + c_4\phi^3 + c_5\phi^2 + c_6\phi + c_7$ (where ϕ is phase angle and the parameters c_1, c_2, c_3, … c_7 are fitting coefficients to match the observations with least-squares method) has the smallest fitting residual. An example of such fitting is shown in Fig. S21. For comparison, a physically-based function (i.e., the double Henyey-Greenstein (H-G) function) is also included in Fig. S21. The double H-G function (Henyey & Greenstein 1941; Hapke, 2002) is defined as $P(A_{HG}, g_1, g_2, f, \phi) = A_{HG} \cdot (f P_{HG}(g_1, \phi) + (1 - f) P_{HG}(g_2, \phi))$, where A_{HG} is the coefficient to match the amplitude of the observed phase function. The term $P_{HG}(g, \phi)$ represents both forward (with a factor g_1 and $g_1 \in [0,1]$) and backward (with a factor g_2 and $g_2 \in [-1,0]$) scattering lobes, respectively. The factor f ($f \in [0,1]$) stands for the fraction of the forward versus backward scattering. The term $P_{HG}(g, \phi)$ (g can be g_1 or g_2 and ϕ is phase angle) has a form as $P_{HG}(g, \phi) = (1 - g^2)/(1 + g^2 + 2g \cdot \cos\phi)^{3/2}$. Figure S21 shows the polynomial-function fitting is better than the double H-G fitting. In addition, the double H-G fitting is smaller than the polynomial-function fitting at the highest phase angles (165-180°). Therefore, our following estimate of the fitting uncertainty at the highest phase angles by assuming the uncertainty can reach the fitted values of the polynomial-function fitting (see B.2 in section S11. Analyses of the uncertainties in determining Titan's radiant energy budget) is good enough. Note that Titan's albedo is larger at very high phase angles (i.e., > 170°) than at 0° phase angle, which is caused by Titan's thick atmosphere and efficient forward scattering of sunlight (Garcia Munoz et al., 2017).

Then the six-order polynomial functions from the least-squares technique are used to fit the phase functions and fill the observational gaps in phase angle for the ISS-derived albedo in the 12 filters during the Cassini epoch. Note that the direct fitting does not work for the data in some years with very poor coverage of phase angle. For these years, we increase the coverage of phase angle by linear interpolation/extrapolation in time from the neighboring years before doing the fitting. The fitting results for the ISS-derived albedo during the Cassini epoch are presented in Fig. S22.

The fitting residuals, which are the differences between the fitted results (Fig. S22) and the data (Fig. S20), are used to evaluate how well the fitting preforms. The ratios between the fitting residuals and the raw data are shown in Fig. S23. Most of the ratios are less than 5% and a few ratios are larger than 5% but smaller than 10%. Generally, the six-order polynomial functions work well in fitting the ISS full-disk albedo and hence filling the observational gaps in phase angle.

There are relatively few high-quality global images from the VIMS observations, so we only find 10 VIMS observations with the phase angle varying from 11.7° to 159.1°. The 10 observations disperse in different years of the Cassini epoch, so the VIMS observations themselves cannot resolve the temporal variations of the phase function of Titan's full-disk albedo. The temporal variations retrieved from the ISS observations are extrapolated to the VIMS wavelength range to address the temporal variations of the phase functions of Titan's Bond albedo in that range (see section "Filling Observational Gaps in Wavelength and Time").

The available VIMS high-quality spectra are displayed in Fig. S24. The 10 VIMS observations do not cover the complete range of phase angle, so we have to fill the observational gaps in phase angle. We first try the six-order polynomial function for the VIMS data. The comparison of fitting in the overlap wavelengths between the ISS and VIMS suggests that the six-order polynomial function works well for the range of phase angle for the VIMS observations (11.7°-159.1°), but it does not work well for fitting the VIMS data in the ranges of low and high phase angles (< 11.7° and > 159.1°) because the VIMS observations are lacking in these ranges. The ISS observations have better coverage than that of the VIMS observations, especially in the range of the low and high phase angles. So we first use the ISS observations in low and high phase angles to fill the VIMS observational gaps. Then we use the six-order polynomial function to fit the data, and such a fitting works well for filling the VIMS observations gaps.

The wavelength range of the VIMS observations is larger than the wavelength range of the ISS observations. For the VIMS wavelengths covered by the ISS 12 filters, we follow the method discussed above to do the fitting and then fill the observational gaps. For the VIMS wavelengths not covered by the ISS filters, we interpolate/extrapolate the ISS observations from the ISS wavelengths to the VIMS wavelengths to fill the VIMS observational gaps at the low and high phase angle first. Then we apply the six-order polynomial function to fit the VIMS data and then fill the observational gaps. After filling the VIMS observational gaps in phase angle, we have the full-disk albedo in the two-dimensional domain of wavelength and phase angle for the VIMS wavelength range (350-5131 nm), which is shown in Fig. S25.

Figure S26 displays the ratio between the fitting residual (i.e., fitting results – observational results) and the observational results for these phase angles where the VIMS observations exist. Most of the fittings have ratios less than 10%, but there are fittings with residual ratios larger than 10% or even 20%. We further examine these fittings with the large residual ratios. We find that the residual ratios generally get bigger with longer wavelengths (especially in these wavelengths longer than 2000 nm). The observational data (i.e., full-disk albedo) are extremely small when wavelengths longer than 2000 nm, so even the small fitting residuals can make the residual ratios pretty large.

These fittings with large residual ratios are mainly in the wavelengths longer than 2000 nm. In these longer wavelengths, solar spectral irradiance contributes a very small fraction (< 6%) to the total solar power. So the uncertainties in these wavelengths do not significantly affect our measurements of Titan's Bond albedo and hence the reflected/absorbed solar power. However, the uncertainty related to such fitting residuals is considered in our analyses of the measurement uncertainties (see section "Analyses of the Measurement Uncertainties").

S9. Filling Observational Gaps in Wavelength and Time

The Cassini observations of Titan's full-disk albedo have observational gaps in not only phase angle but also wavelength. After filling the observational gaps in phase angle, which is discussed in the previous section, we work on the observational gaps in wavelength. Both the ISS and VIMS data have observational gaps in wavelength. The ISS 12 filters record Titan's albedo in separated and limited wavelengths from ultraviolet (~ 264 nm) to near infrared (~ 939 nm) and the VIMS observations do not cover the wavelengths shorter than 350 nm. In order to compute Titan's full-disk albedo, we need measurements of Titan's albedo in the wavelength range of 0-5131 nm. The SSI in this wavelength range contributes to more than 99.5% of the total solar power.

We first fill the observational gaps in wavelength for the Cassini ISS observations. The ground-based observations (see Fig. S3) and the Cassini VIMS observations both suggest that the magnitude of Titan's albedo spectra change with phase angle but the spectral structure and shape basically stay constant. It means that the phase functions are correlated among different wavelengths. With the least-squares fitting, we have derived Titan's full-disk albedo over the whole range of phase angle for these wavelengths covered by the Cassini ISS 12 filters (see Fig. S22). Please note that the ISS UV1/2 observations do not cover all years during the Cassini epoch (see Fig. S20), and we use interpolation and extrapolation to fill the observations gaps in time for the UV1/2 results. Then, we use the complete phase functions (i.e., distribution over phase angles 0-180°) at the Cassini ISS 12 wavelengths to derive the phase functions at all wavelengths from 264 nm (i.e., the shortest wavelength of the ISS observations) to 939 nm (i.e., the longest wavelength of the ISS observations) by referring to the spectral shape at the phase angle 5.7° which is from the high-spectral-resolution measurements (see Fig. S3). Figure S27 displays examples of the ISS-derived albedo in the two-dimensional domain of wavelength and phase angle for these years during the Cassini epoch.

To validate the ISS-derived albedo in the two-dimensional domain of wavelength and phase angle, we compare the derived results between the ISS and VIMS observations. We first average the ISS-derived two-dimensional albedo over the Cassini epoch. Then we compare the time-mean ISS-derived albedo with the VIMS-derived albedo in the overlap wavelengths (350-939 nm). Figure S28 shows that the results are basically consistent between ISS (panel A) and VIMS (panel B) results. Figure S29 further provides the differences and differences ratio between the ISS-derived and the VIMS-derived results. Panel A shows that large differences are mainly concentrated in the low and high phase angles. However, the difference ratios suggest that the values are less than 15% even for these large differences in the low and high phase angles.

To address the temporal variations of Titan's Bond albedo and hence the reflected/absorbed solar power during the Cassini epoch, we require the time series of Titan's full-disk albedo in the two-dimensional domain of wavelength and phase angle with the complete coverage of phase angle (0-180°) and wavelength (0-5131 nm). The above ISS-derived albedos (Fig. S27) with the complete coverage of phase angle are used for the wavelength range 264-939 nm. It should be mentioned that we get Titan's albedo in the two-dimensional domain from both the ISS observations (Fig. S27) and the VIMS observations (Fig. S25) for the overlap wavelengths (i.e., 350-939 nm) between the ISS and VIMS observations. In this study, we use the ISS-derived results for the overlap wavelengths (i.e., 350-939 nm) because: (1) the ISS observations resolved the temporal variations of the phase functions for Titan's full-disk albedos; (2) the coverage of phase angle is much better for the ISS observations than for the VIMS observations so that the fitted phase functions are more precise for the ISS observations than for the VIMS observations; and (3) the spectra from the Earth-based observations[42], which are used to derive the ISS albedo (Fig. S27), have a very high spectra resolution ~ 0.4 nm. Such a spectral resolution is much better than the spectral resolution of the VIMS observations (~ 4-24 nm), so that some fine spectral structures can be better resolved.

The low and high limits of the wavelengths for the ISS observations are 264 nm (UV1) and 939 nm (CB3), respectively. For the temporal variations of Titan's full-disk albedo in the wavelengths shorter than 264 nm (i.e., 0-264 nm), we refer to the ISS measurements at the UV1 filter (264 nm). We first interpolate and extrapolate the UV1 phase functions in 2009 and 2015 (Fig. S22) to the whole Cassini epoch (2004-2017). We then extrapolate the available geometric albedo spectra from the Cassini UVIS (150-190 nm) and the HST/FOS (190-305 nm) (Fig. S4) to the wavelength range 0-150 nm to get the geometric albedo spectra in the wavelength range of 0-264 nm. Finally, the extrapolated phase function in each wavelength of the wavelength range 0-264 nm is combined with the available albedo at the same wavelength to derive Titan's albedo over the complete range of phase angle. For each year of the Cassini epoch, we build the albedo in the two-dimensional domain of wavelength and phase angle for the wavelength range 0-264 nm.

For the temporal variations of Titan's albedo at wavelengths longer than 939 nm (i.e., 939-5131 nm), we combine the ISS and VIMS observations together. The basic idea is that we extrapolate the temporal variations at 939 nm, which are based on the ISS CB3 observations, to the wavelength range 939-5131 nm. The albedos in the wavelength range 939-5131 nm (Fig. S25), which are derived from the VIMS observations, are assumed to be the time-mean albedo. During the process of extrapolating the temporal variations of the ISS observations to the VIMS wavelengths 939-5131 nm, the time-mean two-dimensional albedos (Fig. S25) are used as a reference.

After addressing the temporal variations of Titan's albedo in the wavelengths outside of the ISS coverage (i.e., 0-264 nm and 939-5131 nm), we have the two-dimensional albedo in the complete coverage of phase angle (0-180°) and wavelength (0-5131 nm) for each year during the Cassini epoch (2004-2017). Some examples of such two-dimensional albedo are shown in Fig. S30.

S10. Computing Titan's Bond Albedo and the Related Qualities

Based on Titan's full-disk albedo in the complete domain of wavelength and phase angle for each year of the Cassini epoch (Fig. S30), we can compute Titan's monochromatic Bond albedo and the related qualities at each wavelength for each year of the Cassini epoch. The monochromatic geometric albedo, which is defined as the albedo at phase angle 0°, is automatically found from Fig. S30. The phase integral, which is the integral of phase function of Titan's albedo, can be computed from the distribution of Titan's albedo with phase angle at each wavelength. Finally, we can derive the monochromatic Bond albedo from the product of the monochromatic geometric albedo and monochromatic phase integral (see section "Method of Computing the Bond Albedo").

Figure S31 displays the monochromic geometric albedo, phase integral, and Bond albedo in the two-dimensional domain of time (2004-05 – 2017) and wavelength (0 – 5131 nm). For the distribution with wavelength, the geometric albedo has roughly the same spectral structures as those shown in the Earth-based observations (Fig. S3) and the VIMS observations (Fig. S24) at high phase angles. The phase integral largely increases with wavelength. In the visible part (300-800 nm), the phase integral has the smallest values ~1.6-2.3. In some infrared parts (e.g., 3900-4500 nm), the phase integral can reach the largest values ~5-5.5. In the direction of wavelength, Panel E shows that the Bond albedo has similar distributions as those of the geometric albedo. The Bond albedo reaches maxima (~ 0.4-0.5) around the visible wavelengths between 600 nm and 800 nm, and it becomes very small (< 0.2) at wavelengths longer than 2200 nm. The large Bond albedo between 600 nm and 800 nm is mainly due to the large geometric albedo in the same wavelengths. The small monochromatic Bond albedo at wavelengths longer than 2200 nm is because the small geometric albedo is dominant over the large phase integral at these wavelengths. The anomalies (i.e., difference from time-mean) suggest that the temporal variations of the geometrical albedo (panel B of Fig. S31) and Bond albedo (panel F of Fig. S31) are mainly concentrated in the wavelength range 400-1000 nm. The anomaly of the phase integral (panel D of Fig. S31) displays the temporal variations basically in all wavelengths.

Based on the distribution of the monochromatic Bond albedo (Panel E of Fig. S31), we can compute the wavelength-average Bond albedo (i.e. Titan's Bond albedo) by weighting the monochromatic Bond albedo with the SSI (Fig. S2), as we did in our study of measuring Jupiter's Bond albedo (Li et al., 2018). Titan's Bond albedo during the Cassini epoch is displayed in Fig. 1 in the main text.

The product between the SSI at Titan (panel A of Fig. S2) and the monochromatic Bond albedo (panel E of Fig. S31) generates the reflected SSI. Subtracting the reflected SSI from the SSI at Titan, we have the absorbed SSI at Titan. Multiplying the SSI, the reflected SSI, and the absorbed SSI by the effective radius at each wavelength, we have the total SSI, the total reflected SSI, and the total absorbed SSI over Titan's optical disk at each wavelength. Integrating the total SSI, the total reflected SSI, and the total absorbed SSI at each wavelength over the complete wavelength range 0-5131 nm, we have the total solar power, the total reflected solar power, and the total absorbed solar power at Titan. Their temporal variations during the Cassini epoch are presented in Fig. 2 in the main text.

S11. Analyses of the uncertainties in determining Titan's radiant energy budget

In this section, we discuss the uncertainties in computing Titan's radiant energy budget. Titan's radiant energy budget is determined by the emitted thermal energy and the absorbed solar energy of Titan. Therefore, we mainly discuss the uncertainties in the measurements of Titan's emitted power and absorbed power. In addition, other possible energy sources (e.g., emission from Saturn and Titan's internal heat), which possibly affect the radiant energy budget, are also discussed.

A. Uncertainties in the measurements of Titan's emitted thermal power

We first discuss the uncertainties in computing Titan's emitted power with the Cassini/CIRS observations. Such uncertainties were briefly discussed in our previous studies of Titan's emitted power (Li et al., 2011; Creecy et al., 2019), which are based on the methodology we developed in our investigation of Saturn's emitted power (Li et al., 2010). Here, we provide more discussions on the uncertainty in computing Titan's emitted power. There are two dominant uncertainty sources in computing Titan's emitted power with the Cassini/CIRS observations: (1) the uncertainty related to the CIRS data calibration; and (2) the uncertainty related to filling the observational gaps of the CIRS data.

A.1. Uncertainty in the CIRS data calibration

The basic approach for calibrating the CIRS measurements to radiance of targets (e.g., Titan) was introduced in the introductory CIRS paper (Flasar et al., 2004) and discussed in our previous study of Saturn's emitted power (Li et al., 2010). The main process of the CIRS calibration is to remove the radiance of the background (i.e., the instrument itself) from the radiance of targets. To estimate the background radiance, the CIRS routinely viewed deep space (i.e., zero radiance from target) and recorded the spectra of the deep space. Generally, the spectra of deep space are much smaller than the spectra of targets. Figure S32 displays the comparison between the spectra of Titan and the typical spectra of deep space, which were recorded by the three focal planes (FP1, FP3, and FP4) of the CIRS. Figure S32 suggests that calibration uncertainty mainly comes from the FP1, which is dominant among the three focal planes. So we focus on the FP1 data in the following discussion.

The absolute radiometric calibration of the FP1 was operated at 170 K instrument temperature. The radiance from deep space is the main error source for the CIRS calibration. Figure S33 shows the temporal variations of the FP1 spectra of deep space, which suggests a good stability. The uncertainty related to the background noise in the FP1 spectra is estimated as follows: we randomly choose ~ 100,000 spectra of deep space for each year of 2004–2017. These spectra are first integrated in wavenumber because Titan's spectra are integrated when calculating the emitted power. The mean value and standard deviation of the 100,000 wavenumber-integrated spectra are used as an estimator for the uncertainty due to the background radiance in each year. The mean values and the standard deviations of some years were presented in one of our previous studies (Li et al., 2010). We add the absolute mean value to the standard deviation to estimate the absolute calibration uncertainty of Titan's emitted power for each Earth year.

It should be mentioned that the thermal control of the CIRS instrument possibly affects the data calibration. The entire FP1 interferometer and detector were operated at the 170 K instrument temperature. The sensors were calibrated before flight and didn't show any evidence of drift during the Cassini observational period. The temperature control was about 0.1 K, so an absolute accuracy of 0.2 K overall is a good estimate for the upper limit. Panel A of Fig. 34 shows the blackbody spectra of the CIRS instrument at 170 K. In contrast, we also plot the blackbody spectra at 170.2 K by adding the temperature control (0.2 K) to the designed temperature of the CIRS instrument (170 K). Panel B shows the difference between the two spectra shown in panel A, which is used to estimate the spectral noise related to the temperature control of the CIRS instrument. Panel C is the comparison between the spectral noise and typical spectra of deep space, which suggests that the spectral noise related to the temperature control is much smaller than the spectra of deep space. Therefore, we only consider the spectra of deep space for the CIRS data calibration.

A.2. Uncertainty related to filling CIRS observational gaps

The other uncertainty of computing Titan's emitted power is related to filling observational gaps of the CIRS data in emission angle. Based on the uncertainty analysis in our study of Saturn's emitted power (Li, et al., 2010), we have the sum of unknown radiance in the observational gaps along a single latitude ($P_{emit}(N)$) as

$$P_{emit}(N) = 2\pi \sum_{k=1}^{N} I(\theta_k)\cos\theta_k \sin\theta_k \Delta\theta = \sum_{k=1}^{N} c_k I_k \qquad (1)$$

where N the number of the radiance at the unknown emission angles and $I(\delta_k)$ is the radiance at the unknown emission angles (δ_k). In the above equation, we also simplify the equation with a coefficient c_k, which is represented by $c_k = 2\pi \cos\delta_k \sin\delta_k \Delta\alpha$. Then the total difference between the fitted radiance and the real radiance for all observational gaps along the latitude ($P_{emit}(N)'$) can be expressed as

$$P_{emit}(N)' = \sum_{k=1}^{N} c_k I_k' \qquad (2)$$

where I_k' is the radiance difference between the fitted value and the real value at unknown emission angles.

The variance of $P_{emit}(N)'$ is used to estimate the uncertainty of emitted power related to filling the observational gaps. The variance of the sum of multiple variables can be determined by the following equation (23)

$$\sigma^2\left(P_{emit}(N)'\right) = \sum_{k=1}^{N} c_k^2 \sigma_k^2 + 2\sum_{i=2}^{N}\sum_{j=1}^{i-1} c_i c_j \sigma_{ij}^2 \qquad (3)$$

where σ_k^2 is the variance of the radiance difference I_k' and σ_{ij}^2 is the covariance of the radiance difference at two different unknown emission angles with the two corresponding coefficients c_i and c_j. Our previous analyses (19, 20) show that least-squares fitting does a good job in fitting the recorded radiance. Figure S35 shows an example of the fitting and the fitting residual. The fitting residual is used to estimate the variance of the radiance difference δ_k^2 at the observational gaps. The covariance δ_{ij}^2 will disappear if we assume that the radiances at different unknown points are independent from each other. Then Eq. (3) can be used to compute the uncertainty related to filling the observational gaps.

A.3. Total uncertainty of emitted power

With the analysis in the above section, we have the uncertainty related to filling the observational gaps at each latitude. In addition, we assume that the calibration uncertainty is constant with latitude. As an example, the meridional distribution of calibration uncertainty and filling uncertainty in 2009 are shown in Fig. S36. It suggests that the fitting uncertainty is larger than the calibration uncertainty by roughly one order of magnitude.

We combine the two uncertainties as the total uncertainty of emitted power by $\sigma_{all} = \sqrt{\sigma_{calibration}^2 + \sigma_{fitting}^2}$. Now, we discuss the uncertainty of the global-average emitted power. The global-average emitted power can be written as (Li et al., 2010)

$$\bar{P} = \frac{1}{2(1-2\varepsilon/3)}\sum_{i=1}^{N}\left(1-2\varepsilon\sin^2\varphi_i\right)P(\varphi_i)\cos\varphi_i\Delta\varphi = \sum_{i=1}^{N} c_i P(\varphi_i) \qquad (4)$$

where ε is the oblateness of Titan (~(2574.91-2574.34)/2574.91 ~ 0.00022), φ is latitude, and $P(\varphi_i)$ is the emitted power at the latitude φ_i. The index N is the number of latitude bands from pole to pole. The coefficient c_i is represented by $c_i = \left[\left(1-2\varepsilon\sin^2\varphi_i\right)\cos\varphi_i\Delta\varphi\right] \big/ \left[2\left(1-2\varepsilon/3\right)\right]$. With the coefficient, the global-average emitted power is the sum of multiple variables. Again, we can use the analysis of the variance of the sum of multiple variables (Bevington and Robinson, 2003) to estimate the uncertainty of the global-average emitted power.

Using the uncertainty of emitted power at each latitude ($\sigma^2(P_i)$) (Fig. S36) and assuming the emitted power is independent at different latitudes, we have the uncertainty of the global-average emitted power as

$$\sigma^2(\bar{P}) = \sum_{i=1}^{N} c_i^2 \sigma^2(P_i) \tag{5}$$

Based on eq. (5), we can compute the uncertainty of global-average emitted power in each Earth year during the Cassini time period of 2004–2017. Figure S37 shows the time series of different uncertainties for Titan's emitted power. Panel B of Fig. S37 suggests that the ratios between the total uncertain and Titan's emitted power are about 0.3 percent for the Cassini/CIRS measurements. Such ratios are much smaller than the ratios in the meridional direction (Fig. S36), because averaging uncertainties over all latitudes smoothens the uncertainties into a much smaller value, as Eq. (5) suggests.

The effective radius is different between Titan's emitted thermal emission and absorbed solar irradiance, so we integrate the uncertainty over the effective radius of Titan's thermal emission (i.e., 2575+500 km) (Li et al., 2011) to get the uncertainty of Titan's sphere-integrated emitted power (Fig. S38). Such uncertainty is used in the comparison between the sphere-integrated emitted thermal power and the disk-integrated absorbed solar power (Fig. 3 in the main text), which helps to determine if Titan's global radiant energy budget is balanced.

B. Uncertainties in the measurements of Titan's absorbed solar power

The absorbed solar power is determined by Titan's Bond albedo with known solar flux at Titan (Fig. S2). Therefore, the uncertainties in the absorbed solar energy mainly come from the uncertainties in computing Titan's Bond albedo with the Cassini observations. At each wavelength, the monochromatic Bond albedo (A_λ) can be expressed as below (Li et al., 2018)

$$A_\lambda = \frac{2}{S/D^2} \sum_{\phi_i=0}^{\phi_i=180^o} I_\lambda(\phi_i) \sin\phi_i \Delta\phi \tag{6}$$

where λ is wavelength, πS is the solar constant at Earth, D is the distance of the planet from the Sun in astronomical units (1 AU = 149.6×10^9 m), and $I_\lambda(\phi_i)$ is the reflected solar irradiance at phase angle ϕ_i.

We organize the uncertainty sources in the measurements of monochromatic Bond albedo in three categories: (1) the uncertainty in calibrating the Cassini ISS and VIMS images; (2) the uncertainty related to filling observational gaps with the least-squares fitting; and (3) other uncertainties.

B.1. Uncertainty in the ISS and VIMS data calibration

We first discuss the uncertainty in the calibration of the ISS and VIMS data. For the ISS images, we use the latest version of the Cassini ISS CALibration software (Knowles et al., 2020), to calibrate the data. The calibrated ISS images are generated with a unit of radiance, as shown in Fig. S39. In Fig. S39, the domain outside Titan's disk corresponds to deep space. It should be mentioned the calibrated radiance in the domain of deep space, which is used to estimate the absolute calibration of the CIRS spectra, cannot be used to estimate the absolute calibration uncertainty of the ISS images. In the ISS images, the domain of deep space contains light from

Titan's disk spreading out by the point spread function, plus stray light from scattering of Titan light off the structures in the telescope (West et al., 2010; Knowles et al., 2020).

In the ISS calibration papers (West et al., 2010; Knowles et al., 2020) and the Cassini calibration manual (https://pds-rings.seti.org/viewmaster/volumes/COISS_0xxx/COISS_0011/), the calibration uncertainties, which include many error sources (e.g., uneven bit-weighting, 2-Hz noise, dark current in the ISS cameras, bright/dark pixel pair artifacts from anti-blooming mode, flat-field artifacts), are discussed in detail. Most of the calibration uncertainty sources vary with filter, viewing geometry, and observing object. But the combined effect of these uncertainty sources typically results to ~ a few percent of the calibrated radiance (2-6%) (Knowles et al., 2020). Here, we assume that the total calibration uncertainty is 5% for the absolute calibrated radiance of Titan's images. It should be emphasized that the 5% calibration uncertainty is not systematic and it is a random error (Knowles et al., 2020). In other words, it overestimates the real radiance at some wavelengths & phase angles but underestimates the radiance at other wavelengths and phase angles (Knowles et al., 2020). When we integrate the recorded radiance over wavelength and phase angle for computing the Bond albedo, the calibration uncertainties at different wavelengths and phase angles cancel each other so that its effect on the Bond albedo becomes very small (<1%). It should be mentioned that there is a systematic uncertainty related to the ISS instrumental effect. For the ISS images in which Titan occupies almost all of the image frames, some of Titan's reflected flux can be outside of the ISS image frames. This effect systematically underestimates the real radiance. Fortunately, such images are relatively few (< 10% of the total global images used in our analysis). The tests by the ISS calibration team suggest that such a systematic bias is ~ 0.5% of the total scattered flux from Titan, which is accounted in our computation of Titan's Bond albedo.

For Cassini VIMS observations, the calibration has already been discussed in a few previous studies (15, 50-53). Work described by McCord et al. (2004) and Filacchione et al. (2007) conducted the basic calibration processes (e.g., correcting flat-field artifacts, subtracting the noise from the radiation of Cassini's power generators, and removing cosmic rays). The calibration of the VIMS data of satellites of Saturn (Pitman et al., 2010) suggests that the calibration uncertainty is on the order of 5% of the calibrated radiance. Based on these previous analyses, the calibration uncertainty for the VIMS data is 5%. Such an estimate is the same as that of the ISS data even though the two instruments did independent calibrations. As discussed with respect to the ISS calibration uncertainty, the VIMS 5% calibration uncertainty is not systematic either. The random calibration errors at different wavelengths and phase angles cancel each other when integrating over wavelength and phase angle for Titan's Bond albedo.

The comparison of full-disk albedo between the ISS and VIMS (Fig. S16 in section "Validation of Cassini ISS and VIMS results"), which are based on the calibrated data from the two instruments, also suggests that the calibrations from the two instruments are consistent. Finally, the validation of the Cassini ISS/VIMS data by the other observations (Fig. S17-19 in section "Validation of Cassini ISS and VIMS results") also suggests that the Cassini ISS/VIMS data are calibrated well.

B.2. Uncertainty related to filling ISS/VIMS observational gaps

From the equation of monochromic Bond albedo (Eq. (6)), we know that the Bond albedo is determined by the reflected solar irradiance at phase angles varying from 0° to 180°. But there are observational gaps in phase angle for the Cassini ISS/VIMS observations (see Figs. S20 and S24). In the equation of monochromic Bond albedo, the part for the observational gaps can be expressed as

$$A'_\lambda = \frac{2}{S/D^2}\sum_{i=1}^{N} I_\lambda\left(\phi_i\right)\sin\phi_i\Delta\phi = \sum_{i=1}^{N} c_i I_\lambda\left(\phi_i\right) \tag{8}$$

where N is the number of unobserved points in phase angle and the coefficient c_i is expressed as $c_i = 2D^2\sin\phi_i\Delta\phi/S$. Then the Bond albedo for the observational gaps can be represented as the sum of multiple variables. Likewise, we use the variance of the sum of multiple variables (Bevington and Robinson, 2003) to estimate the uncertainty of the Bond albedo from filling the observational gaps as below

$$\sigma^2\left(A'_\lambda\right) = \sum_{i=1}^{N} c_i^2\sigma\left(I_\lambda\left(\phi_i\right)\right) \tag{9}$$

Now we discuss how to estimate the variance of the reflected radiance at the unobserved phase angles. The observational gaps in phase angle are filled by least-squares fitting for the Cassini ISS/VIMS observations of Titan's reflected solar irradiance. Figure S40 shows a fitting example for the full-disk albedo recorded by the ISS observations, which suggests that the least-squares fitting does a good job in fitting the Cassini observations. Panel C of Fig. S39 further suggests that most of the residual ratios are less than 3%. The fitting residual is used in the estimate of the uncertainty in the CIRS measurements of Titan's emitted power by least-squares fitting. Such a method works for the fitting for the ISS/VIMS observational gaps at the relatively s, but it does not work for the ISS/VIMS observational gaps at very high phase angles.

The smallest phase angles of the ISS observations change from ~ 0.5° to ~ 4.4° for most filters except for the filters UV1, UV2, and CB1 (see Fig. S20). The smallest phase angles for the ISS images recorded by UV1, UV2, and CB3 are between ~ 8.4° and ~ 9.8°. The smallest phase angle for the high-quality VIMS observations is ~ 9.8° (see Fig. S24). The Cassini ISS/VIMS observations at the s are consistent with other observations at s including 0° phase angle, which were recorded by the HST and ESO (see Fig. S18). So we think least-squares fitting works well for extrapolating the ISS/VIMS observations at the s including 0° phase angle. Therefore, we use the fitting residuals to estimate the variances of the ISS/VIMS observational gaps at the relatively s.

The estimate of the variances of the ISS/VIMS observational gaps at very high phase angles is a different story. In our discussion of the uncertainty in the measurements of Titan's emitted power with the Cassini CIRS observations, the fitting residuals are used to estimate the variance for these observational gaps at both low and high emission angles. But there is one difference between the CIRS observational gaps in emission angle and the ISS/VIMS observational gaps in phase angle. For the CIRS observations, we have the data around the lowest and highest emission angles (0° and 90° respectively) for most latitudes (see Fig. S35), so we know the basic distribution of emitted radiance along emission angle. But for the ISS/VIMS observations, we have the observations around the lowest phase angle (0°) but not around the highest phase angle (180°), as shown in Fig. S20. There are no high-quality ISS/VIMS observations at the phase angles larger than ~165° because the solar irradiance comes into the instrument and could damage the Cassini detectors if the phase angle is even higher. In addition, the ground-based telescopes and Earth-orbiting observatories can conduct observations of Titan with s only (< 6.5°) due to the orbit geometry of Earth and Titan. The largest phase angle of the Pioneer 11 observations is ~ 96°.

In summary, there are no high-quality observations of Titan at phase angles larger than ~165°. Lacking observations makes it difficult to estimate the uncertainty in filling the observational gap at the phase angles larger than 165°. Using the fitting residuals at the lower phase angle probably underestimates the uncertainties at high phase angles larger than 165°. In this study, we use the fitting residuals at these available points (Fig. S40) to estimate the variance of the observational gaps with phase angles smaller than 165°. For the observational gaps with phase angles larger than 165°, we set larger uncertainty and assume that the uncertainty can reach the fitted values.

B.3. Other uncertainties in the measurements of Titan's Bond albedo

In addition to the uncertainties from the Cassini data calibration and filling the observational gaps in phase angle, there are other uncertainty sources. The first one is the high-altitude detached haze. Some haze features have altitudes higher than 500 km, which are beyond the effective radii of Titan's reflected solar irradiance. Figure S41 shows that the detached high-altitude haze shows in the ISS images at some filters but not in other filters. Even for the ISS images including strong-reflection haze (e.g., panel A of Fig. S41), our calculation suggests that the reflected solar irradiance from the detached haze is ~ 0.2% of the total reflected solar irradiance from the full disk of Titan. Therefore, the high-altitude haze does not significantly contribute to the uncertainty of the Bond albedo compared to the calibration and filling uncertainties. However, we include it in the uncertainty analysis.

The errors in estimating the effective radii of Titan's reflected solar irradiance also introduce uncertainty in computing Titan's Bond albedo. Based on the average effective radius (~ 2884.9 km) retrieved from the ISS observations and the corresponding average error (~ 9.7 km), we simply estimate the uncertainty as $((2884.9+9.7)^2–2884.9^2)/ 2884.9^2$ ~ 0.7%.

Titan has a thick atmosphere, which is not uniform in latitude and longitude. In addition, atmospheric processes (e.g., clouds) vary with time. Finally, the solar irradiance can be reflected from Titan's surface at some wavelengths (e.g., the ISS CB3 filter). The optical characteristics of Titan's surface vary spatially. The heterogeneous nature of the atmosphere and surface and their possible temporal variations can introduce more uncertainty in measuring the full-disk albedo of Titan. Figure S42 shows full-disk images of Titan recorded by the ISS CB3 filter at different times but with the same phase angle (~ 14°). The CB3 images record both the atmosphere and surface of Titan, so the CB3 images at different times can be used to address the heterogeneous property of Titan's atmosphere and surface and their temporal variations. The first two global images are separated by ~ 3 days, which are shorter than the orbital period of Titan around Saturn (~ 16 Earth days). The two images cover different longitudes (panel A mainly covers longitudes ~ 200-360° and 0-20° and panel B mainly covers longitudes ~150-330°). So the comparison between panels A and B can help us to address not only the heterogeneous property but also the diurnal variation of Titan's atmosphere and surface. However, we find that the full-disk albedo only changes ~ 0.4% from 0.1911 in the first image to 0.1903 in the second image in Fig. S42.

We average the observations in each year of the Cassini period (2004-2017) to get yearly albedo of Titan. So the temporal variations with time scales longer than one Titan day (~ 16 Earth days) but shorter than one Earth year are not resolved. Panel C of Fig. S42 shows an image of Titan recorded ~ 2 Earth months after the second image (panel B). But the two images have the roughly same latitude/longitudinal coverage. Therefore, the comparison between panel B and panel C can help us examine the temporal variations of Titan's full-disk albedo at the time scales longer than one Titan day but shorter than one Earth year. Titan's full-disk albedo changes ~ 0.7% from 0.1903 in panel B to 0.1890 in panel C. Therefore, Titan's heterogeneous property and temporal variations at the time scales shorter than one Earth year is probably smaller than 1% and we assume 1% for this uncertainty.

The cloud bands also develop on Titan sometimes. An example of such cloud bands is shown in Fig. S43. Cloud bands are generally composed by very bright clouds aligned in the longitudinal direction. Our estimates shows that the cloud bands shown in Fig. S43 increase the original albedo by ~ 20%. The ratio between the area of the cloud bands and the full-disk area is ~ 2%, so the cloud bands increase the full-disk albedo by 0.4%. It is hard to examine the whole lifetime (i.e., from birth to death) of the cloud bands. But it is probable that the cloud bands have lifetimes less than one half of an Earth year. So the cloud bands shown in Fig. S43 increase the annual-mean albedo with an upper limit 0.4% × 1/2 = 0.2%.

Combining the uncertainties from the high-altitude haze, the error in determining Titan's effective radius, the spatio-temporal variability of Titan's atmosphere and surface, and the effects of cloud bands, we have the combined uncertainty as $\sqrt{0.002^2+0.007^2+0.01^2+0.002^2}$ =0.012 = 1.3%.

B.4. Total uncertainty of Bond albedo

We combine the calibration, fitting, and other uncertainties into the total uncertainty of Titan's monochromic Bond albedo ($\delta(A_\lambda)$). The total uncertainty can expressed as

$$\delta(A_\lambda)=\sqrt{\delta_{cal}^2(\lambda)+\delta_{fit}^2(\lambda)+\delta_{other}^2(\lambda)} \tag{10}$$

where $\delta_{cal}(\lambda)$, $\delta_{fit}(\lambda)$, and $\delta_{other}(\lambda)$ are uncertainties related to data calibration, fitting, and other error sources, respectively. Titan's Bond albedo is computed by weighting the monochromic Bond albedos over the whole wavelength range (0-6000 nm) by the solar spectral irradiance. But the Cassini ISS/VIMS observations do not cover the whole wavelength range, and there are observational gaps in wavelength. First, we interpolate/extrapolate the uncertainty in these wavelengths recorded by the Cassini ISS/VIMS to other wavelengths in the wavelength range of 0-6000 nm. Figure S43 shows the spectral distribution of the uncertainties in the measurements of monochromic Bond albedo during the Cassini epoch.

Figure S44 suggests that the uncertainty related to filling the observational gaps in phase angle is dominant in the total uncertainty. This figure also shows that the temporal variations of the uncertainties are not very strong. That is because the ISS and VIMS data calibrations and the observational gaps do not vary significantly with time. Figure S45 further shows the ratio between the total uncertainty and the corresponding monochromic Bond albedo. First, we can see that the spectral distribution of the total uncertainty is basically the same as that of the measured Bond albedo, which means that the uncertainties of the large Bond albedo are also large. Second, the ratio can reach 35% in some wavelengths (panel C of Fig. S45). These large ratios appear in the wavelengths longer than 1000 nm. The relatively small monochromic Bond albedos at these wavelengths are the main reason why there are large ratios. It should be mentioned that the large ratios in these wavelengths do not significantly contribute to Titan's Bond albedo and the corresponding uncertainty because the SSI in the wavelengths longer than 1000 nm are relatively small compared to the SSI in the short wavelengths.

Based on the spectral distribution of the uncertainties in the monochromatic Bond albedo (Fig. S44), we can estimate the uncertainties of Titan's Bond albedo. The Bond albedo (A) is computed by weighting the monochromic Bond albedos with the SSI as below (Li et al., 2018)

$$A=\frac{1}{SSI_{sum}}\sum_{\lambda=0}^{\lambda=5131nm} SSI_\lambda A_\lambda=\sum_{\lambda=0}^{\lambda=5131nm} c_\lambda A_\lambda \tag{11}$$

where SSI_λ and SSI_λ are the SSI at different wavelengths and the sum of SSI over wavelength, respectively. The coefficient c_λ is defined as $c_\lambda = SSI_\lambda / SSI_{sum}$. Eq. (11) suggests that the process of computing Bond albedo is like the sum of the monochromatic Bond albedos at different wavelengths with weighting factors. Therefore, the uncertainty of Titan's Bond albedo can be estimated from the uncertainties of the monochromatic Bond albedo by applying the rule of error propagation of addition (Bevington and Robinson, 2003) as below

$$\sigma^2(A) = \sum_\lambda c_\lambda^2 \sigma^2(A_\lambda) \tag{12}$$

where $\delta^2(A)$ and $\delta^2(A_\lambda)$ are variances of Titan's Bond albedo and monochromatic Bond albedo, respectively. Combining the spectral distribution of the monochromatic Bond albedo (Fig. S44) and Eq. (12), we have uncertainty of Titan's Bond albedo shown in Fig. S46. Compared with the uncertainties in the monochromic Bond albedo (Fig. S44), the uncertainties in Titan's Bond albedo (Fig. S46) are much smaller because the uncertainties of monochromic Bond albedo can cancel each other when they are averaged over wavelength.

When investigating Titan's radiant energy budget, we need to determine the emitted thermal power and the absorbed solar power. Considering that the effective radius is different between Titan's emitted thermal emission (Creecy et al., 2019) and absorbed solar irradiance (this study), we need to compute the sphere-integrated emitted power and absorbed power. The uncertainties in the sphere-integrated emitted thermal power are discussed in previous section. Here, we discuss the uncertainty of disk-integrated absorbed solar power, which are related to the uncertainties of disk-integrated solar flux and reflected solar power.

Titan's disk-integrated solar flux is computed by production of the SSI at Titan (Fig. S2) and Titan's disk areas based on the effective radii (Figs. S8-S15). The solar flux at Titan is based on the measured solar constant at Earth (Fig. S1), which have negligible uncertainties. So the uncertainty in the disk-integrated solar flux is mainly determined by the uncertainty in the measurements of effective radii. Because the uncertainty in the measurements of effective radius is very small and such small uncertainty becomes even smaller when averaging over wavelength (see Eq. (12)). Then the uncertainty in the disk-integrated solar flux can be used to compute the uncertainty in the disk-integrated reflected solar power. The disk-integrated reflected solar power can be computed by $P_{reflect} = P_{solar} \times A$ (where P_{solar} and $P_{reflect}$ are disk-integrated solar flux and the reflected solar power respectively). Based on the error propagation, we have the uncertainties of disk-integrated reflected solar power as

$$\frac{\delta^2(P_{reflect})}{P_{reflect}^2} = \frac{\delta^2(P_{solar})}{P_{solar}^2} + \frac{\delta^2(A)}{A^2} \tag{13}$$

where $\delta^2(P_{reflect})$ and $\delta^2(P_{solar})$ are variances of the disk-integrated solar flux and reflected solar power, respectively. The disk-integrated absorbed solar power (P_{absorb}) can be computed by $P_{absorb} = P_{solar} - P_{reflect}$. Then the uncertainty in the disk-integrated absorbed solar power ($\delta(P_{absorb})$) can expressed as

$$\delta^2(P_{absorb}) = \delta^2(P_{solar}) + \delta^2(P_{reflect}) \tag{14}$$

where $\delta^2(P_{absorb})$ is the variance of the disk-integrated absorbed solar power. The uncertainties of the disk-integrated solar flux, reflected solar power, and absorbed solar power are shown in Fig. S47, which are furthered used in Figs. 2 and 3 in the main text.

C. Other uncertainties affecting the radiant energy budget of Titan

When investigating the global radiant energy budget of Titan, we take the atmosphere and surface as a system. For such a system, there are other energy sources, which should be considered. The first one is the emitted thermal radiance from Saturn. Saturn's emitted power is ~ 4.95 Wm^{-2} in the Cassini epoch (Li et al., 2010). Such a power drops to ~ 0.012 Wm^{-2} at the distance of Titan. During the Cassini epoch, Titan's average solar constant (Fig. S2) and Bond albedo (Fig. 1 in the main text) are ~ 15.04 Wm^{-2} and ~ 0.26, respectively. So the absorbed solar power is ~ 15.04×(1-0.26) = 11.13 Wm^{-2}. Assuming that the albedo for the Saturn's thermal radiance is the same as Titan's Bond albedo (~ 0.26), we have the absorbed power from Saturn's thermal emission is ~ 0.012×(1-0.26) = 0.009 Wm^{-2}, which is about 0.1% of the absorbed solar power (0.009/11.13 ~ 0.1%).

There are two other energy sources: (1) internal energy released from the surface (Sohl et al., 1995; Tobie et al., 2006); (2) tidal heat (Tobie et al., 2006). Both have values of order 10^{-3} Wm^{-2}, which is comparable to the thermal radiant power from Saturn's emission. The two powers are also comparable to the uncertainty in the measurements of Titan's emitted thermal power (~ 0.006 Wm^{-2}) (see Fig. S37) but are much smaller than the uncertainty in the measurements of Titan's absorbed solar power. The measurements of Titan's Bond albedo and hence the absorbed solar power have large uncertainty because there are no observations of reflected solar irradiance at the highest phase angles. Based on the uncertainty of Titan's Bond albedo (~ 0.0026, see Fig. S45) and the solar constant at Titan (~ 15.04 Wm^{-2}, see Fig. S2), we have the uncertainty in the measurements of Titan's absorbed solar power as 15.04×0.0026 = 0.039 Wm^{-2}. Such an uncertainty is much larger the uncertainties from internal energy and tidal heat. Therefore, the powers from Saturn's thermal emission, internal energy, and tidal heat are not considered in our discussion of the global radiant energy budget of Titan.

In summary, the uncertainty related to filling observational gaps is dominant in the measurements of Titan's emitted power (see Figs. S36 and S37). For the uncertainty of the measurements of Titan's Bond albedo and hence absorbed solar power, the large observational gaps at the highest phase angles (~ 165-180°) significantly contribute to the uncertainty (see Fig. S44). The large observational gaps in measuring Titan's Bond albedo also make the uncertainty is much larger in the measurements of Titan's absorbed solar power (~ 0.039 Wm^{-2}) than in the measurements of Titan's emitted thermal power (~ 0.006 Wm^{-2}), as we discussed above. Considering that the emitted power goes off from the whole sphere and the absorbed solar power acts on the cross section of Titan, we have that uncertainties of the total power are not that different between the disk-integrated absorbed power (~ 10×10^{11} W, see Fig. S47) and the sphere-integrated emitted power (~ 7×10^{11} W, see Fig. S38).

Extending the Cassini analysis to a complete Titan's year

The Cassini epoch (2004-2017) occupies slightly less than one half of Titan's orbital period around the Sun (i.e., a Titan year ~ 29.4 years). In order to examine Titan's radiant energy budget during a complete Titan year, we investigate the possible seasonal cycles of the absorbed solar power and the emitted power. The temporal variations of the absorbed solar power follow the seasonal cycle of the solar irradiance (Fig. 2). Earth's global emitted power (Jacobowitz et al., 1979; Yang et al., 1999) clearly displays a seasonal cycle, so we assume that Titan's emitted power also has a seasonal cycle (Creecy et al., 2019). We use a sine function with a period of 29.4 years to fit the observed absorbed power and emitted power (Fig. 3) and estimate their seasonal cycles, which are displayed in Fig. S48. The uncertainty of fitting is estimated by the fitting residuals and extrapolating the fitting residuals from the Cassini epoch to a complete Titan year.

Integrating the fitted functions over a complete Titan year (Fig. 3), we find that the total absorbed solar energy, $(2.676\pm0.005)\times10^{23}$ J, and the total emitted thermal energy, $(2.549\pm0.053)\times10^{23}$ J, have an even bigger energy imbalance of $(0.127\pm0.053)\times10^{23}$ J for the complete Titan year. Such an energy imbalance is 5.0±2.1% of the total emitted energy for a complete Titan year. The extrapolated energy imbalance over a complete Titan year is larger than the energy imbalance during the Cassini epoch because the relatively large energy imbalance mainly happened in the time period before the Cassini epoch (see Fig. S48).

References

Ajello J. M. et al. (2008). Titan airglow spectra from the Cassini Ultraviolet Imaging Spectrograph: FUV disk analysis. *Geophysical research letters* 35, L06102.

Baines K. H. et al. (2005). The atmospheres of Saturn and Titan in the near-infrared: First results of Cassini/VIMS. *Earth, Moon, and Planets* 96, 119-147.

Bevington, P. R. & Robinson, D. K. (2003). Data Reduction and Error Analysis for the Physical Sciences, 3rd ed. (McGraw-Hill).

Brown, R. H. et al. (2004). The Cassini visual and infrared mapping spectrometer (VIMS) investigation, *Space Sci. Rev.* 115, 111-168.

Buratti B. J. et al. (2010). Cassini spectra and photometry 0.25–5.1 μm of the small inner moons of Saturn. *Icarus* 206, 524-536.

Conrath, B. J., Hanel, R. A. & Samuelson, R. E. (1989). Thermal Structure and Heat Balance of the Outer Planets. In *Origin and Evolution of Planetary and Satellite Atmospheres* (eds. Atreya, S. K., Pollack, J. B., & Matthews, M. S.) (The University of Arizona Press).

Cours, T., Cordier, D., Seignovert, B., Maltagliati, L., Biennier, L. (2020). The 3.4 μm absorption in Titan’s stratosphere: Contribution of ethane, propane, butane and complex hydrogenated organics. *Icarus* 339, 113571.

Creecy, E. C., Li, L., Jiang, X., Nixon, C. A., West, R. A. & Kenyon, M. E. (2019). Seasonal Variations of Titan's Brightness. *Geophysical Research Letters* 46, 13649-13657.

Esposito, L. W. et al. (2004). The Cassini ultraviolet imaging spectrograph investigation. *Space science reviews* 115, 299-361.

Filacchione, G. et al. (2007). Saturn's icy satellites investigated by Cassini-VIMS: I. Full-disk properties: 350–5100 nm reflectance spectra and phase curves. *Icarus* 186, 259-290.

Flasar, F. M. et al. (2004). Exploring the Saturn system in the thermal infrared: The Composite Infrared Spectrometer. *Space Sci. Rev.* 115, 169–297.

Garcia Muñoz, A. G., Lavvas, P. & West, R. A. (2017). Titan brighter at twilight than in daylight. *Nature Astronomy* 1, 1-7.

Hapke, B. (2002). Bidirectional reflectance spectroscopy: 5. The coherent backscatter opposition effect and anisotropic scattering. *Icarus* 157, 523-534.

Henyey, L.G. & Greenstein, J. L. (1941). Diffuse radiation in the galaxy. *The Astrophysical Journal* 93, 70-83.

Jacobowitz, H., Smith, W. L., Howell, H. B., Nagle, F. W., Hickey, J. R. (1979). The first 18 months of planetary radiation budget measurements from the Nimbus 6 ERB experiment. *Journal of the Atmospheric Sciences* 36, 501-507.

Karkoschka, E. (1994) Spectrophotometry of the jovian planets and Titan at 300-to 1000-nm wavelength: The methane spectrum. *Icarus* 111, 174-192.

Karkoschka, E. (1998). Methane, Ammonia, and Temperature Measurements of the Jovian Planets and Titan from CCD–Spectrophotometry. *Icarus* 133, 134-146.

Knowles, B. et al. (2020). End-mission calibration of the Cassini Imaging Science Subsystem. *Planetary and Space Science* 185.

Lean, J. L., Rind, D. H. (2009). How will Earth's surface temperature change in future decades? *Geophysical Research Letters* 36.

Li, L., Conrath, B. J., Gierasch, P. J., Achterberg, R. K., Nixon, C. A., Simon-Miller, A. A., Flasar, F. M., Banfield, D., Baines, K. H., West, R. A., Ingersoll, A. P., Vasavada, A. R., Del Genio, A. D., Porco, C. C., Mamoutkine, A. A., Segura, M. E., Bjoraker, G. L., Orton, G. S., Fletcher, L. N., Irwin, P. G. J. & Read, P. L. (2010). Emitted power of Saturn. *Journal of Geophysical Research - Planet* 115, art. No. E11002.

Li, L. et al. (2011). The Global Energy Balance of Titan. *Geophys. Res. Lett*. 38, L23201.

Li, L. et al. (2018). Less absorbed solar energy and more internal heat for Jupiter. *Nature communications* 9, 3709.

Maltagliati, L. et al. (2015). Titan's atmosphere as observed by Cassini/VIMS solar occultations: CH4, CO and evidence for C2H6 absorption. *Icarus* 248, 1-24.

McCord, T. B. et al. (2004). Cassini VIMS observations of the Galilean satellites including the VIMS calibration procedure. *Icarus* 172, 104-126.

McGrath M. A. et al. (1998). The ultraviolet albedo of Titan. *Icarus* 131, 382-392.

McKay, C. P., Pollack, J. B., Courtin, R. (1989). The thermal structure of Titan's atmosphere. *Icarus* 80, 23–53.

Pitman, K. M., Buratti, B. J., Mosher, J. A. (2010). Disk-integrated bolometric Bond albedos and rotational light curves of saturnian satellites from Cassini Visual and Infrared Mapping Spectrometer. *Icarus* 206, 537-560.

Porco, C. C. et al. (2004). Cassini Imaging Science: Instrument characteristics and anticipated scientific investigations at Saturn, *Space Sci. Rev.* 115, 363-497.

Seignovert, B., Rannou, P., West, R. A., Vinatier, S. (2021). Haze seasonal variations of Titan's upper atmosphere during the Cassini Mission. *The Astrophysical Journal* 907, 36.

Smith, P. H. (1980). The radius of Titan from Pioneer Saturn data, *J. Geophys. Res.* 85, 5943–5947.

Sohl, F., Sears, W. D., Lorenz, R. D. (1995). Tidal dissipation on Titan. *Icarus* 115, 278-294.

Thomas, P. C. (2010). Sizes, shapes, and derived properties of the saturnian moons after the Cassini nominal mission. *Icarus* 208, 395-401.

Tobie, G., Lunine, J. I., Sotin, C. (2006). Episodic outgassing as the origin of atmospheric methane on Titan. *Nature* 440, 61-64.

Tomasko, M. G., Smith, P. H. (1982). Photometry and polarimetry of Titan: Pioneer 11 observations and their implications for aerosol proper- ties. *Icarus* 51, 65–95.

Tomasko, M. G., Bezard, B., Doose, L., Engel, S., Karkoschka, E., Vinatier, S. (2008). Heat balance in Titan's atmosphere, *Planet. Space Sci.* 56, 648–659.

Toon, O. B., McKay, C. P., Griffith, C. A., Turco, R. P. (1992). A physical model of Titan's aerosols. *Icarus* 95, 24-53.

West, R. et al. (2010). In-flight calibration of the Cassini imaging science sub-system cameras. Planetary and Space Science 58, 1475-1488.

West, R.A., Seignovert, B., Rannou, P., Dumont, P., Turtle, E. P., Perry, J., Roy, M. and Ovanessian, A. (2018). The seasonal cycle of Titan's detached haze. *Nature Astronomy* 2, 495-500.

Willson, R. C., Mordvinov, A. V. (2003). Secular total solar irradiance trend during solar cycles 21–23. *Geophysical Research Letters* 30.

Yang, S. K., Hou, Y. T., Miller, A. J., Campana, K. A. (1999). Evaluation of the earth radiation budget in NCEP–NCAR reanalysis with ERBE. *Journal of climate* 12, 477-493.

Zebker, H. A., Stiles, B., Hansley, S., Lorenz, R., Kirk, R. L. & Lunine, J. (2009). Size and shape of Saturn’s moon Titan. *Science* 324, 921–923.

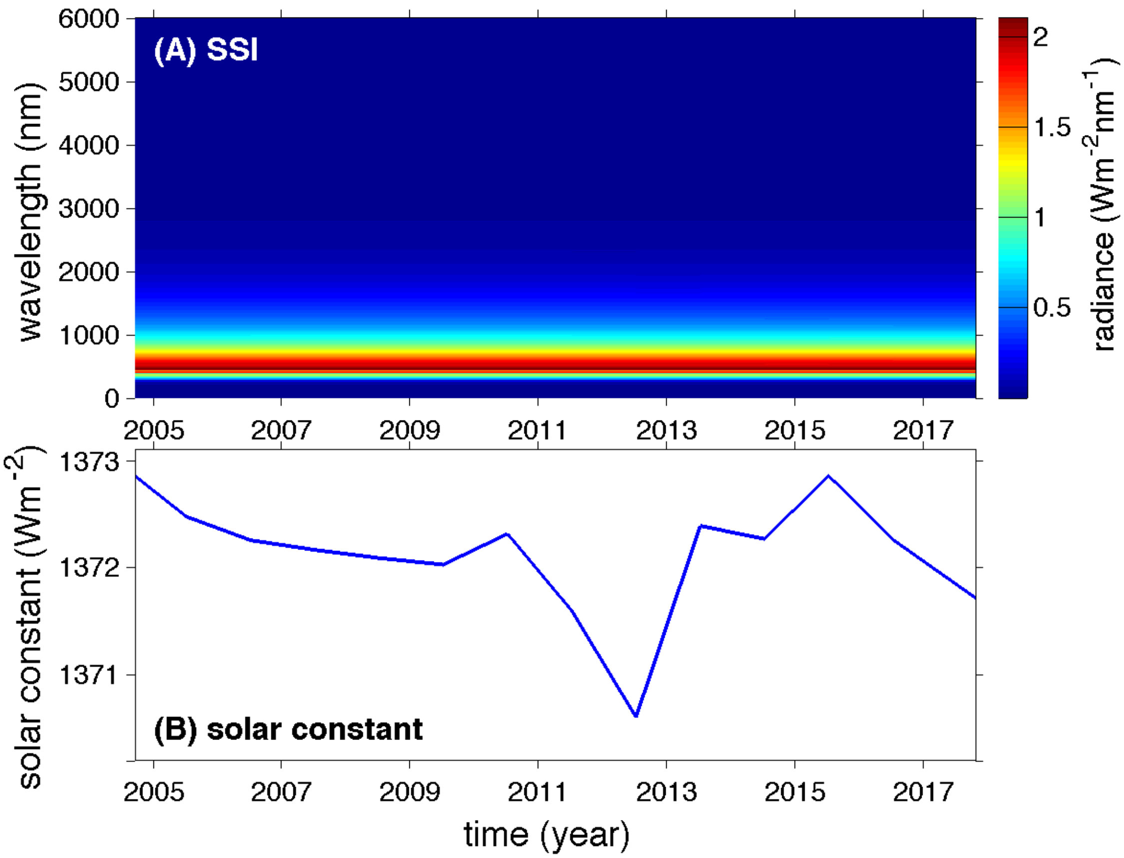

Figure S1. The Solar Spectral Irradiance (SSI) at Earth from 2004 to 2017. (A) Earth's SSI. (B) Earth's solar power (i.e., solar constant). The solar power is computed by integrating the SSI over wavelength. The time-varying SSI from 2004 to 2017 in the wavelength range 0-200 nm and 200-2400 nm comes from the Solar EUV Experiment (SEE) and the Solar Radiation and Climate Experiment (SORCE), respectively. The climatological SSI in the wavelength range 2400-4000 nm comes from American Society for Testing and Materials (ASTM). The SSI in the range 4000-6000 nm is computed by assuming the blackbody spectra with a temperature 5778 K (which matches best the observed SSI over the wavelength range 0-4000 nm), in which the temporal variations of SSI are not considered (see Table S1 for more details).

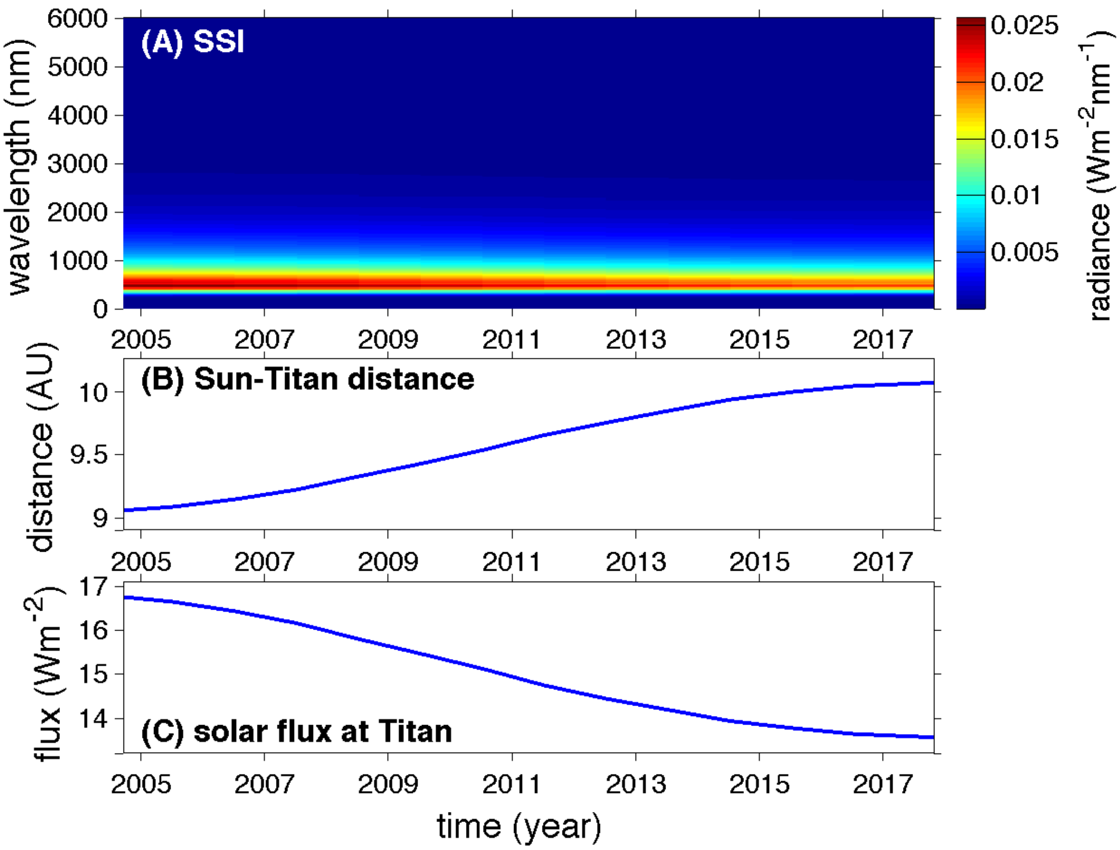

Figure S2. The SSI, Sun-Titan distance, and solar flux at Titan from 2004 to 2017. (A) The SSI at the distance of Titan. (B) The distance between the Sun and Titan. (C) The solar flux at the distance of Titan. The SSI at the distance of Titan (panel A) is computed by dividing the SSI at Earth (panel A of Fig. S1) by the square of the distance between the Sun and Titan (panel B). The solar flux at Titan is computed by integrating the SSI (panel A) over wavelength.

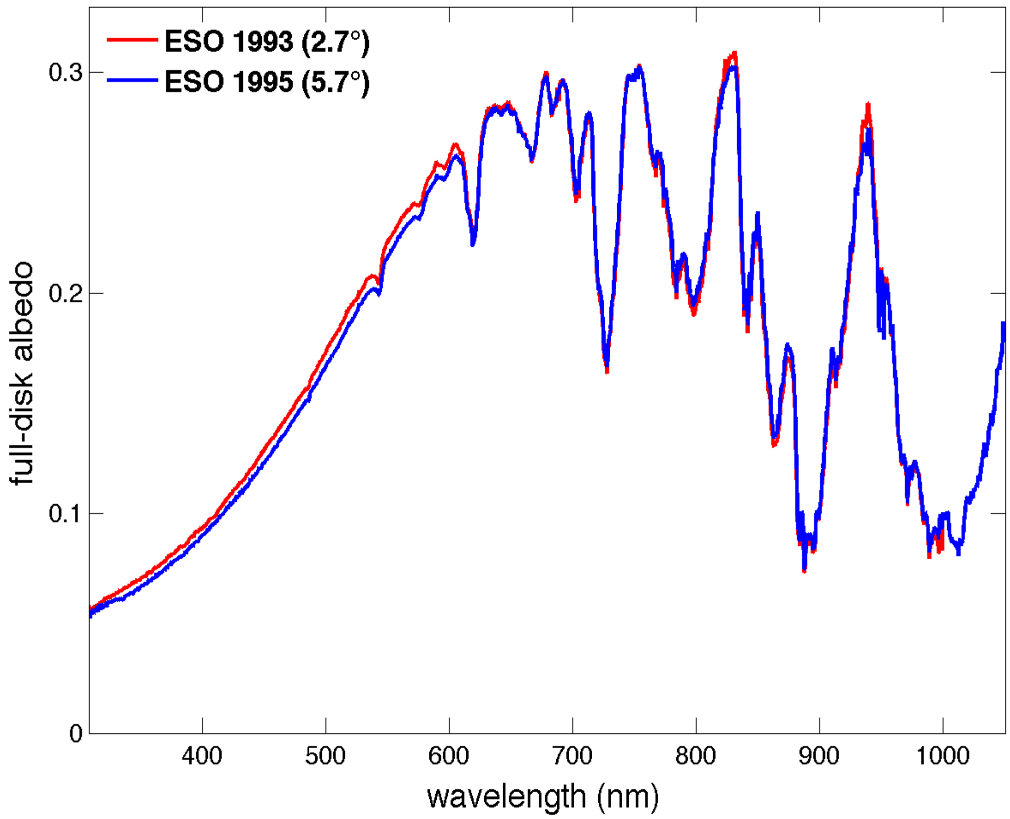

Figure S3. Titan's albedo spectra (305-1050 nm) recorded by the European Southern Observatory (ESO). The two spectra were recorded in 1993 and 1995 with phase angles 2.7° and 5.7° respectively. Note that the spectra generated by Karkoschka were derived with the solid radius of Titan ~ 2575 km (see section "Supplementary Observations and Data" in Materials and Methods). Titan's wavelength-dependent effective radii (see section "Effective Radii of Titan's Atmosphere") are considered in the spectra.

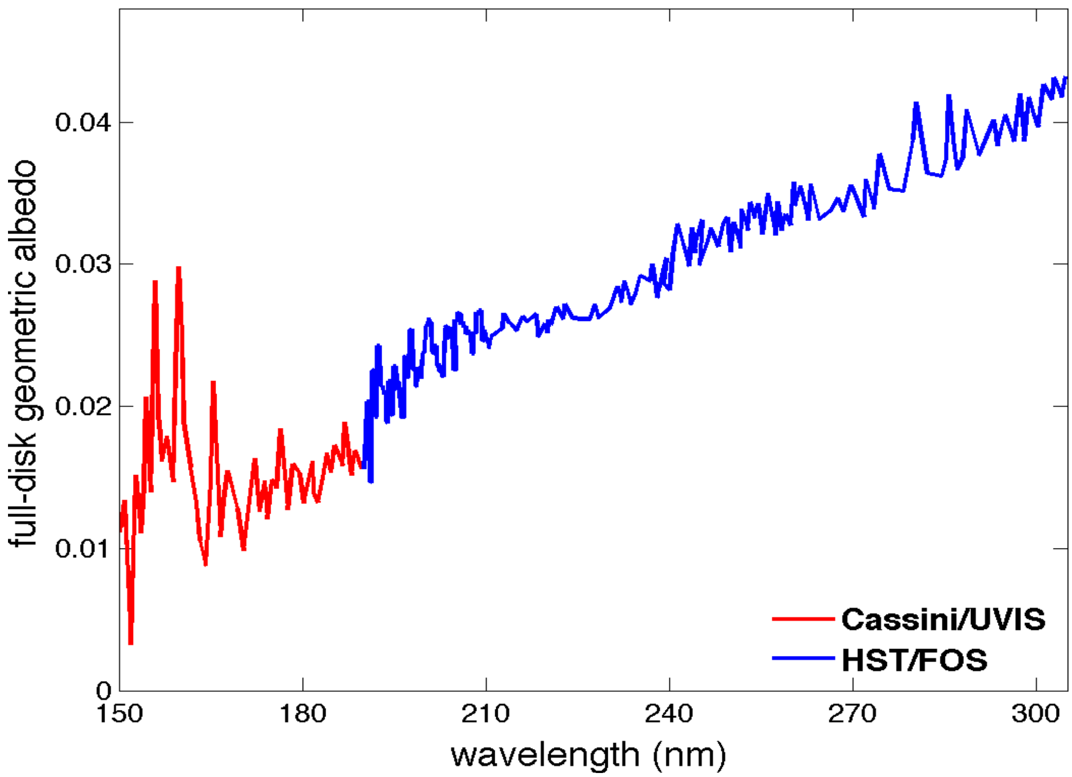

Figure S4. Titan's albedo spectra (150-305 nm) from the Cassini UVIS and the HST/FOS. The geometric-albedo spectra in the wavelength range 150-190 nm come from the Cassini UVIS and the geometric-albedo spectra in the wavelength range 190-305 nm come from the Faint Object Spectrograph (FOS) of the Hubble Space Telescope (HST) (also see Supplementary Information Table S1). Note that Titan's wavelength-dependent effective radii (see section "Effective Radii of Titan's Atmosphere") are considered in the spectra.

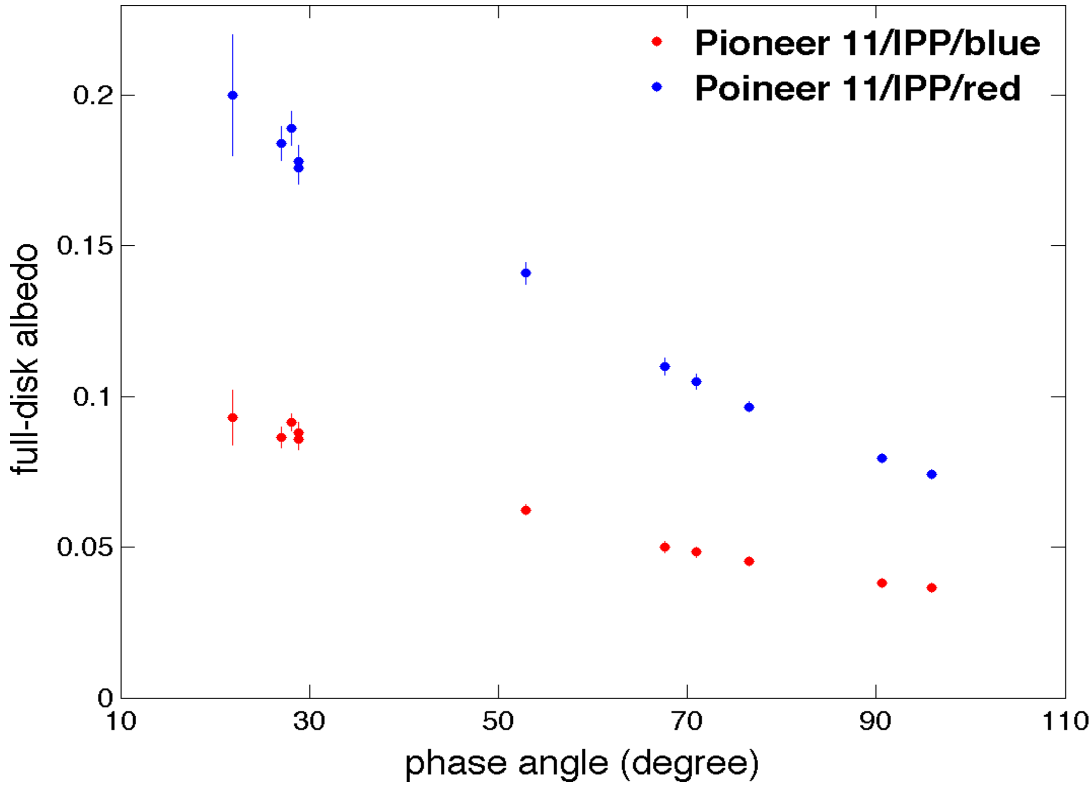

Figure S5. Phase function of Titan's albedo from Pioneer 11 observations. The variations of Titan's albedo as a function of phase angle at blue (452 nm) and red (648 nm) wavelengths come from a previous study based on the observations recorded by the Imaging Photopolarimeter (IPP) on the Pioneer 11 spacecraft. Note that Titan's wavelength-dependent effective radii (see section "Effective Radii of Titan's Atmosphere") are considered. Vertical lines represent error-bars of measurements.

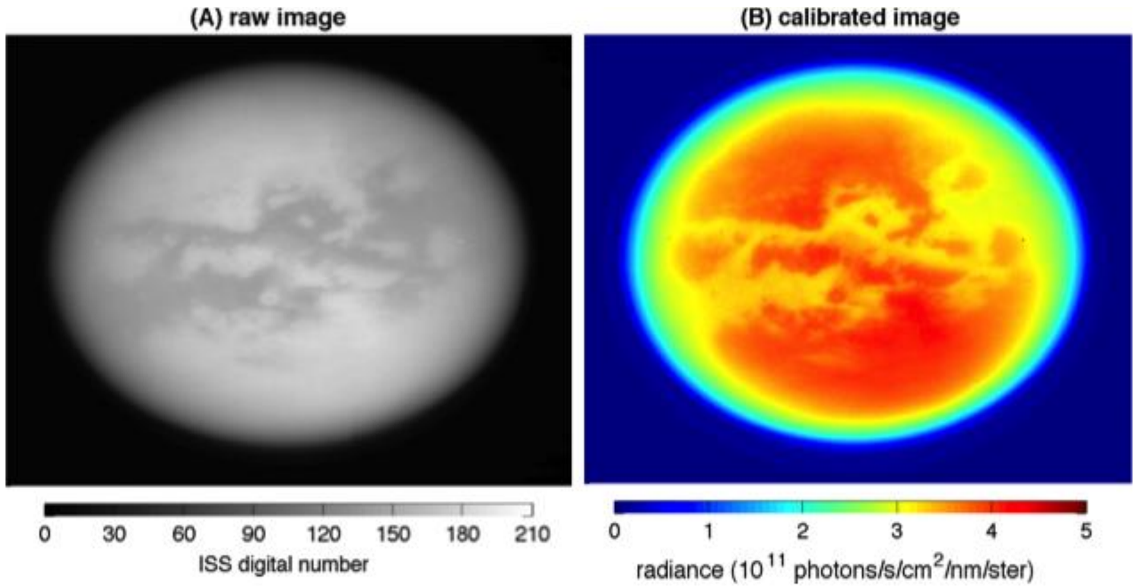

Figure S6. An example of the ISS raw and calibrated images. (A) The ISS raw image. (B) The calibrated image with a unit of radiance. The raw image was taken by the ISS CB3 filter on August 27, 2009 with a phase angle ~ 0.75° and a spatial resolution ~ 8.6 km/pixel. The ISS raw images are calibrated by the Cassini ISS CALibration (CISSCAL) software (see section "Cassini ISS/VIMS Data and Data Processing").

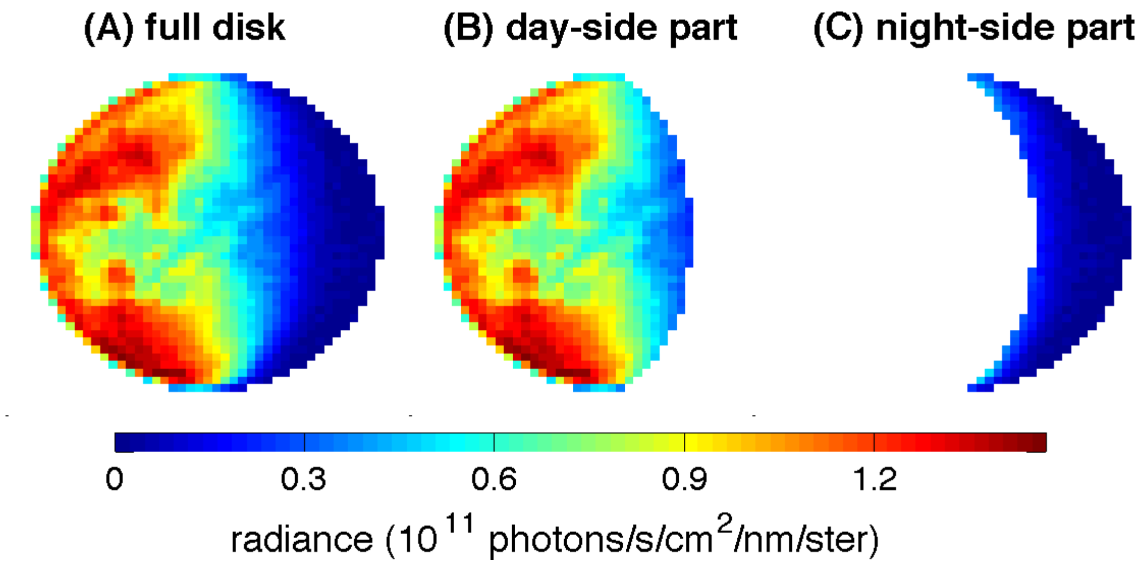

Figure S7. Examples of the VIMS calibrated images. (A) Full-disk image. (B) Day-side image. (C) Night-side image. The corresponding VIMS raw image was taken by the VIMS on July 1, 2006 with a phase angle ~ 60.7° and a spatial resolution ~ 135.5 km/pixel. The VIMS took images from ~ 350 nm to ~ 5131 nm. The example shown here has a wavelength ~ 2000 nm.

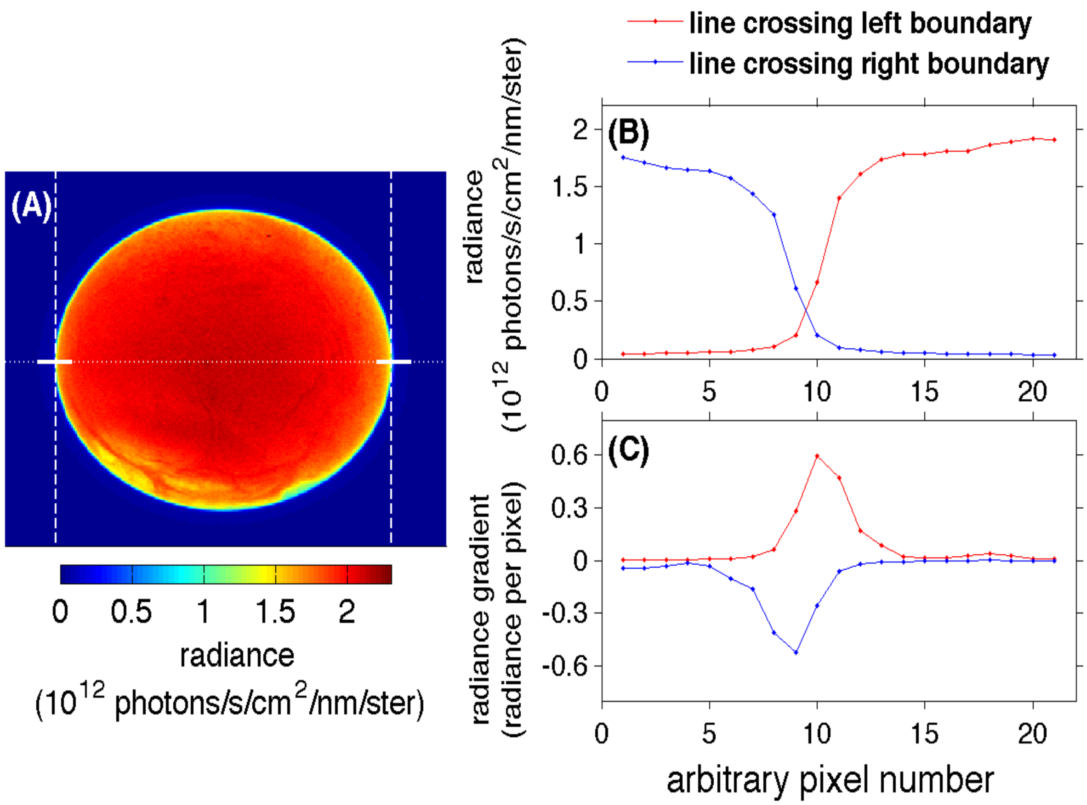

Figure S8. Test of the effective radius of Enceladus. (A) A calibrated image of Enceladus. The corresponding raw image in panel A was taken by the Cassini ISS at RED filter with a phase angle of ~1.36° and a spatial resolution ~ 2.58 km/pixel. The two horizontal solid white lines in panel A, which are located in the left and right boundaries of Enceladus respectively, are used to conduct the analyses in panels B and C. The two vertical dashed white lines in panel A show the locations of the two boundaries with Enceladus' optical disk, which are determined by the analyses in panels B and C. (B) The calibrated radiance along the two horizontal solid white lines shown in panel A. (C) The gradient of radiance along the horizontal direction for the two boundary lines shown in panel B. The locations of the vertical dashed white lines in panel A, which suggest the left and right boundaries of Enceladus's optical disk, are determined by the pixel locations with the maximal gradient of the line crossing the left boundary and the minimal gradient of the line crossing the right boundary, respectively. The product between the pixel number between the two vertical dashed lines and the spatial resolution is used to estimate the effective diameter, and half of the effective diameter is the effective radius (also see section "Effective Radii of Titan's Atmosphere").

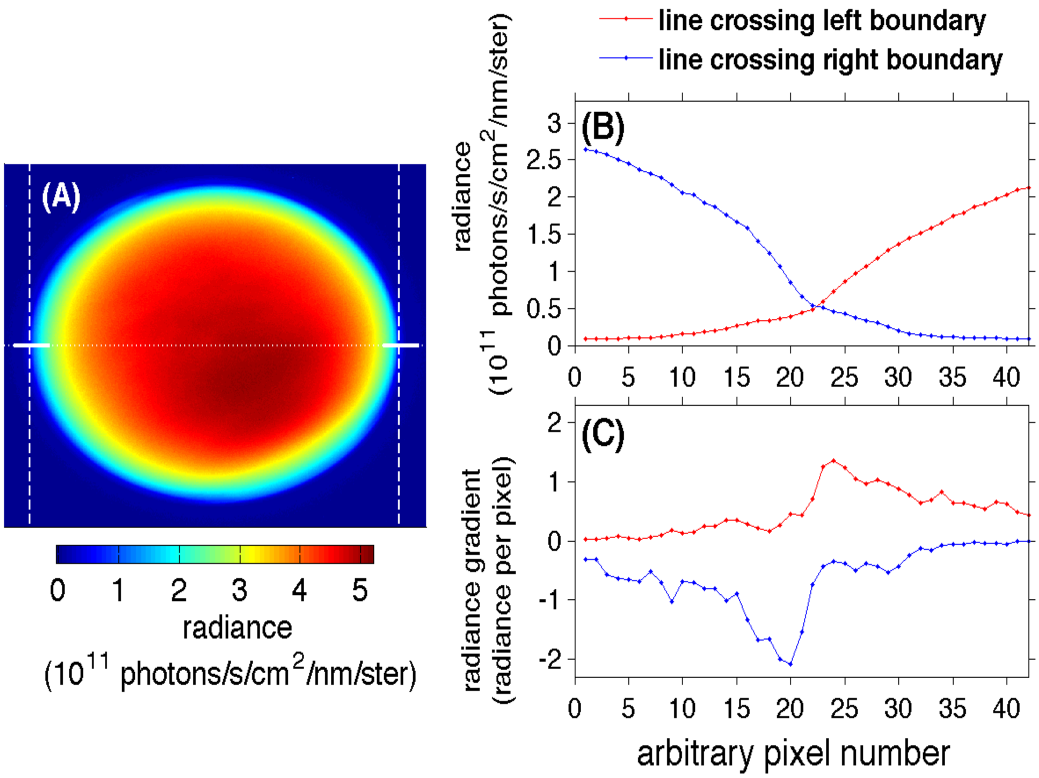

Figure S9. Titan's effective radius at the RED wavelength with a high phase angle. This figure is the same as Fig. S8 except for the image of Titan. The raw image corresponding to the calibrated image in panel A was taken by the RED filter of the Cassini ISS on April 13, 2013 with a phase angle ~4.26° and a spatial resolution ~ 10.8 km/pixel.

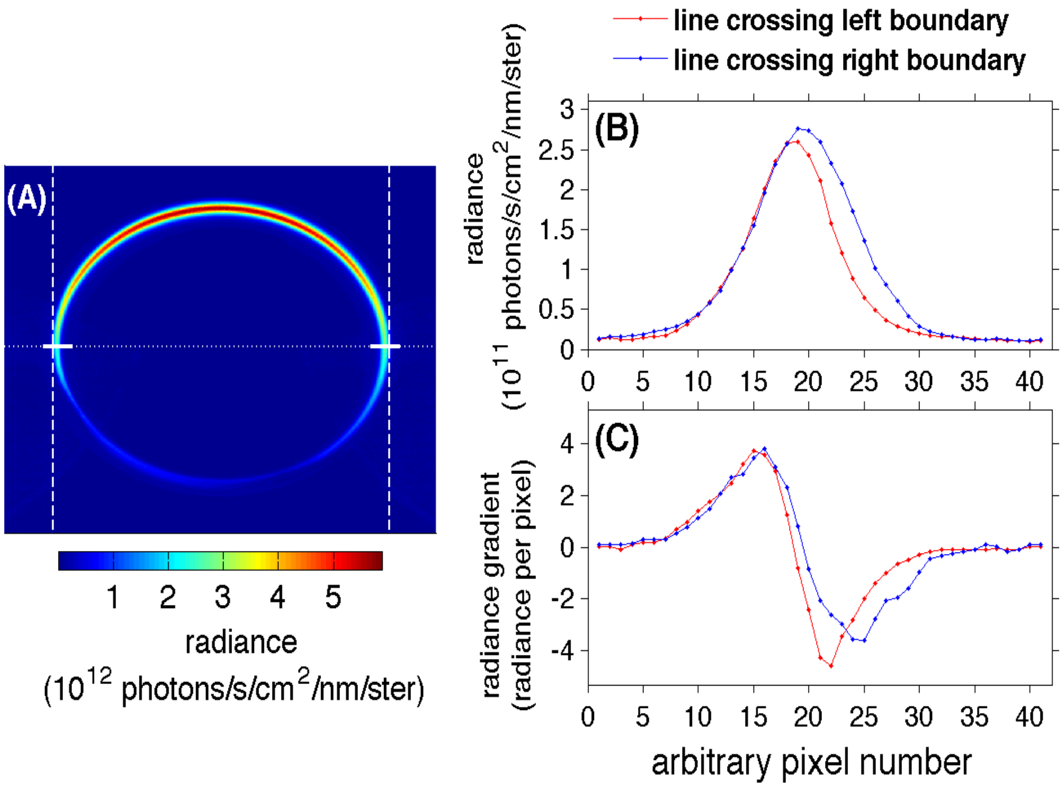

Figure S10. Titan's effective radius at the RED wavelength with a high phase angle. This figure is the same as Fig. S9 except that the image was taken at a high phase angle. The raw image corresponding to the calibrated image in panel A was taken by the RED filter of the Cassini ISS on June 29, 2007 with a phase angle ~166.56° and a spatial resolution ~ 12.4 km/pixel.

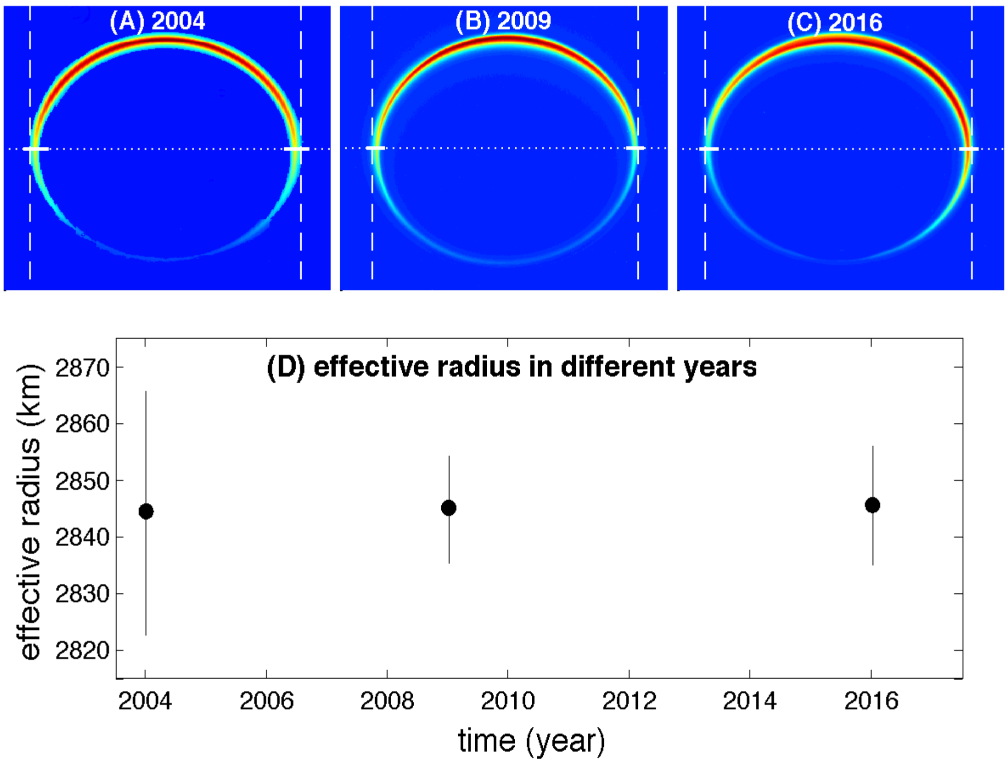

Figure S11. Temporal variations of Titan's effective radius at the CB3 wavelength. Panels A-C are the ISS calibrated images recorded by the CB3 filter in three different years. (A) A calibrated image in 2004. The corresponding raw image was taken by the CB3 filter of the Cassini ISS on December 13, 2004 with a phase angle ~ 161.21° and a spatial resolution ~ 21.8 km/pixel. (B) A calibrated image in 2009. The corresponding raw image was taken by the CB3 filter on July 22, 2009 with a phase angle ~ 161.30° and a spatial resolution ~ 9.7 km/pixel. (C) A calibrated image in 2016. The corresponding raw image was taken by the CB3 filter on November 10, 2016 with a phase angle ~ 164.06° and a spatial resolution ~ 10.6 km/pixel. (D) Titan's effective radius at the CB3 wavelength in different years. Please see the caption of Fig. S8 for explanations of the solid and dashed white lines in panels A-C. Vertical lines in panel D represent error-bars of measurements.

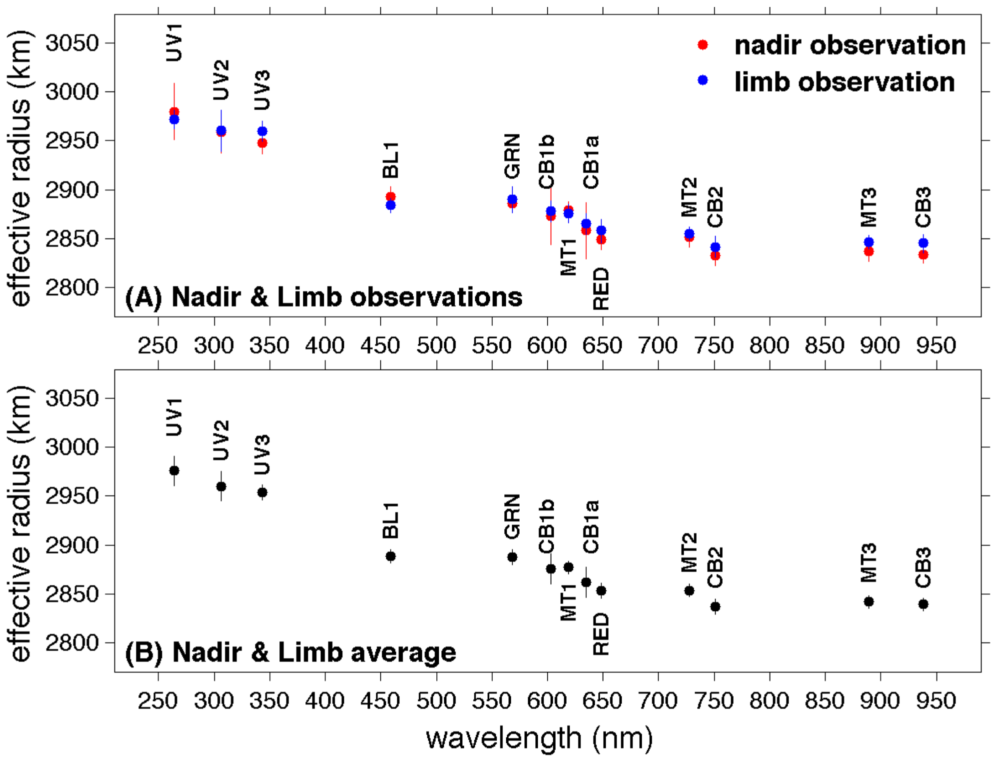

Figure S12. Titan's effective radii measured by the Cassini ISS 12 filters. (A) Effective radii at the wavelengths of the ISS 12 filters with low and high phase angles. Note: the CB1 is composed by two sub-filters (CB1a and CB1b). It is hard to differentiate the CB1 observations between CB1a and CB1b. We use the CB1 observations to get the effective radii first. Then we use the slope of effective radii at the neighboring filters (GRN and RED) to interpolate the CB1 results to the wavelengths of CB1a and CB1b. (B) Averaged effective radii at the wavelengths of the ISS 12 filters. We average over the analyses at the low and high phase angles shown in panel A to get the average radii. Vertical lines in the two panels represent the error-bars of the measurements (see section "Effective Radii of Titan's Atmosphere").

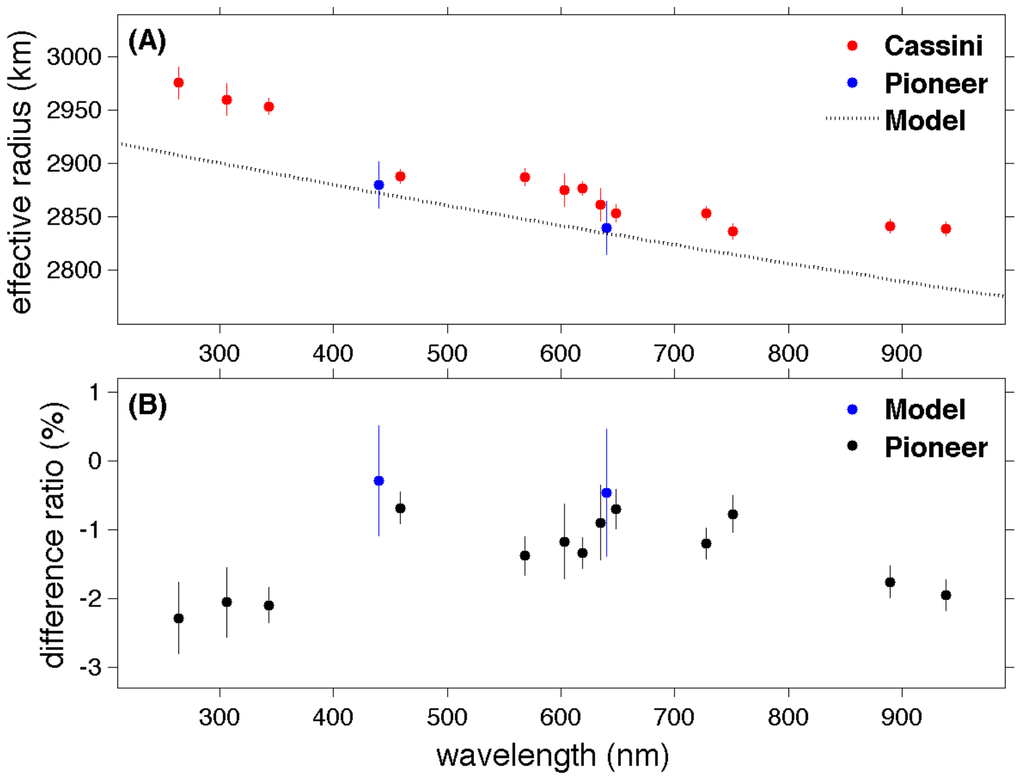

Figure S13. Comparison of Titan's effective radii between the Cassini ISS measurements and other studies. (A) Comparison among the Cassini results, the Pioneer results, and the results from a model study. (B) The ratio of the difference between the Cassini results and other results over the Cassini results. Please note the wavelengths of the red (640 nm) and blue (440 nm) filters from the Pioneer observations are slightly different from the wavelengths of the RED and BL1 filters from the Cassini observations. We linearly interpolate the Cassini results to the Pioneer red and blue wavelengths and then compute the difference between the Cassini results and the Pioneer results (please see section "Effective Radii of Titan's Atmosphere" for more details and references).

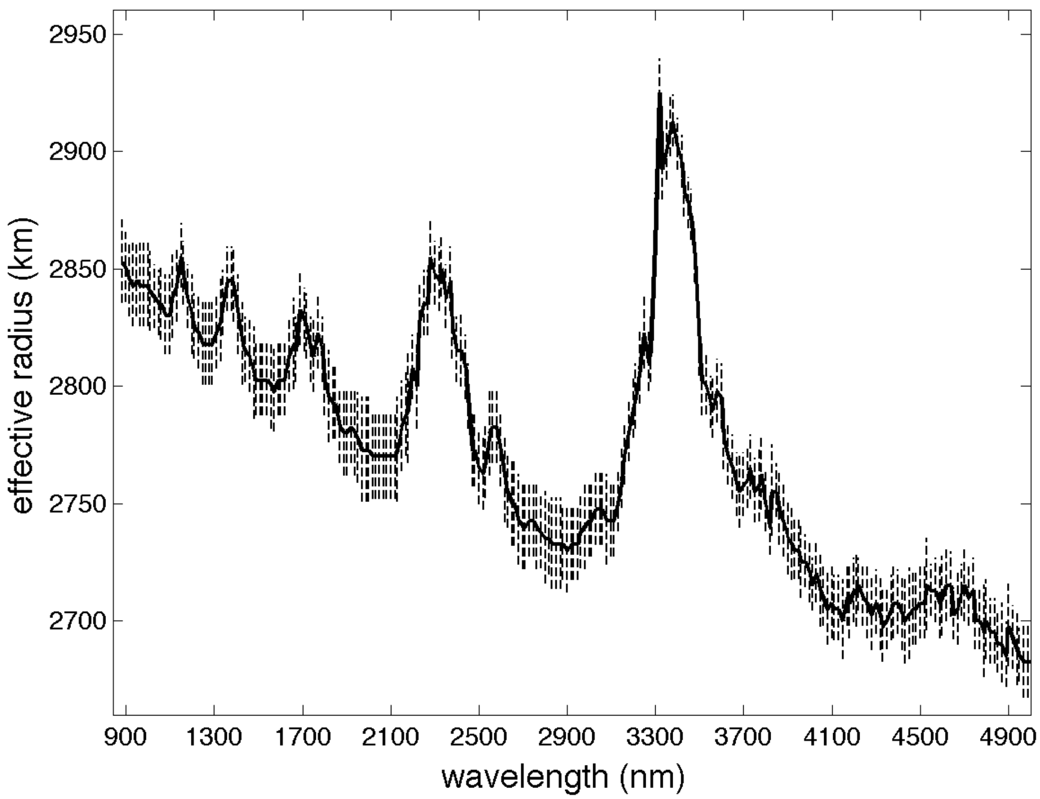

Figure S14. Titan's effective radii measured by the Cassini VIMS observations. The measurements are based on four solar-occultation observations. The four measurements are averaged to get the mean effective radii in the infrared wavelengths of the VIMS instrument (thick black line). The vertical dashed lines represent the uncertainties of the effective radii (see section "Effective Radii of Titan's Atmosphere").

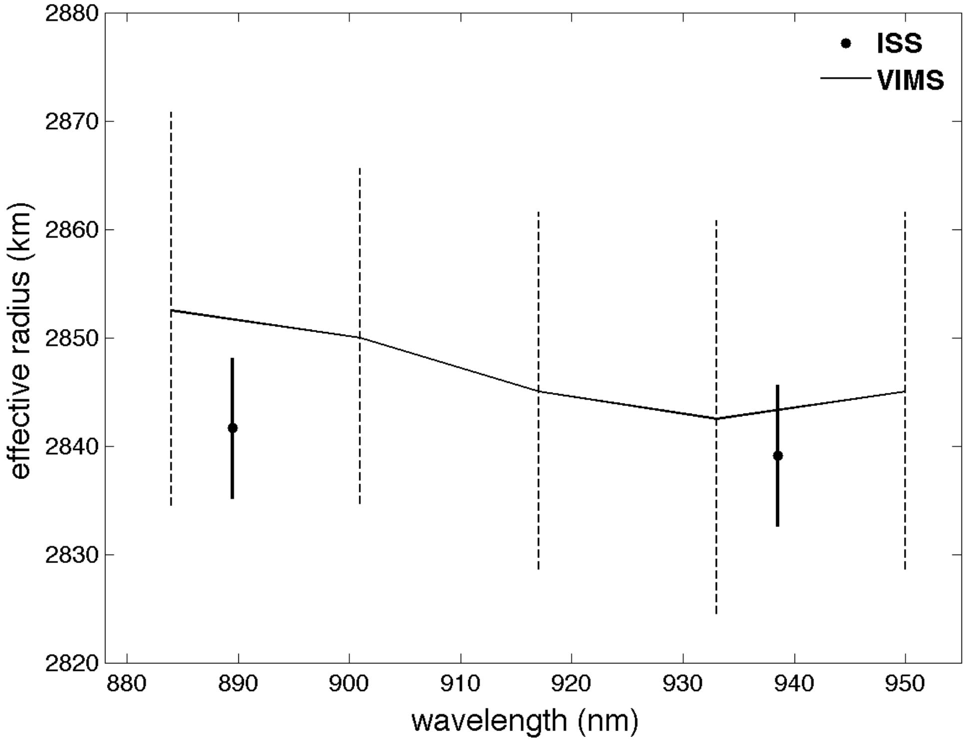

Figure S15. Comparison of effective radii between the Cassini ISS and VIMS measurements. The vertical solid and dashed lines are for error-bars of the measurements of ISS and VIMS, respectively. As we discussed in text, the solar-occultation observations were conducted in the infrared part of the VIMS instrument (840-5000 nm). The VIMS infrared wavelengths are overlapped with two ISS filters/wavelengths only (i.e., MT3-889 nm and CB3-938 nm).

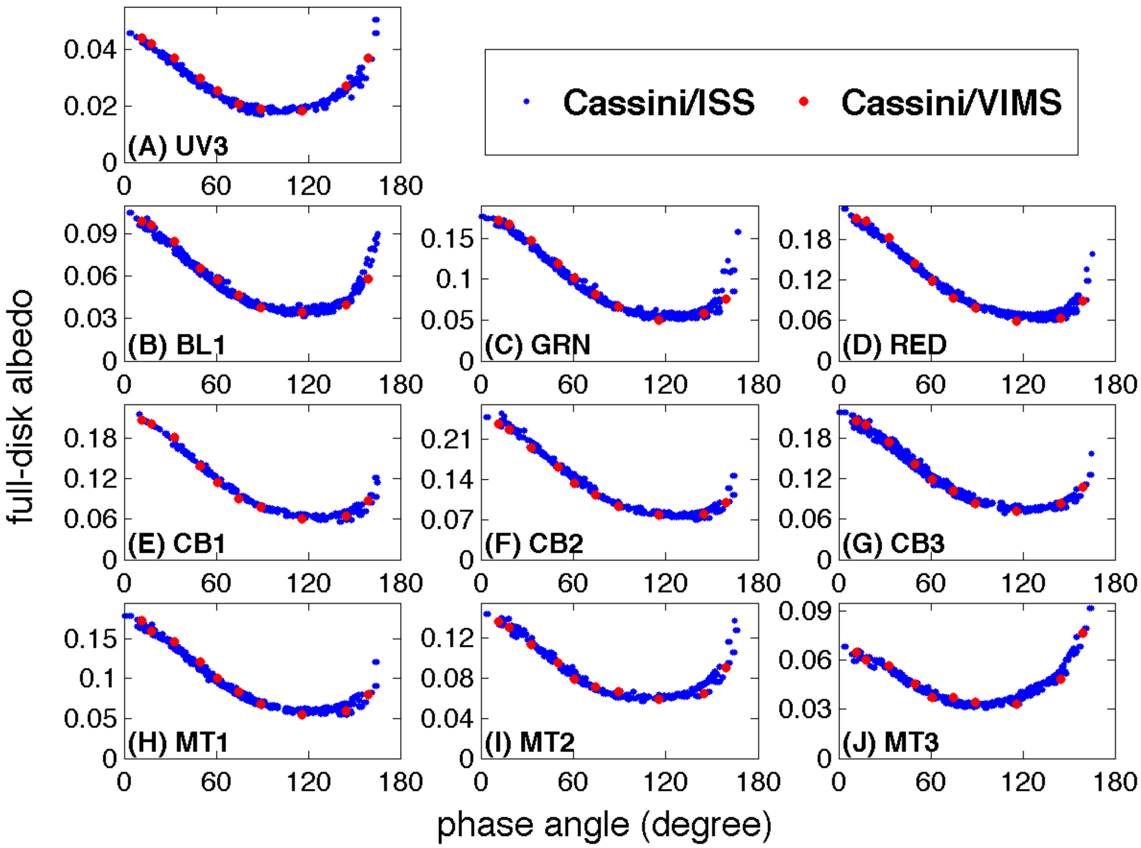

Figure S16. Comparison of Titan's full-disk albedo between the Cassini ISS and VIMS observations. Among the ISS 12 filters, the three violet filters (UV1 ~ 264 nm, UV2 ~306 nm, and UV3 ~ 343 nm) are out of the wavelength range of the VIMS (350-5131 nm). The wavelength of the UV3 filter (343 nm) is close to the low limit of the VIMS wavelength (350 nm), so we keep the ISS UV3 results and compare them with the VIMS measurements at 350 nm (panel A).

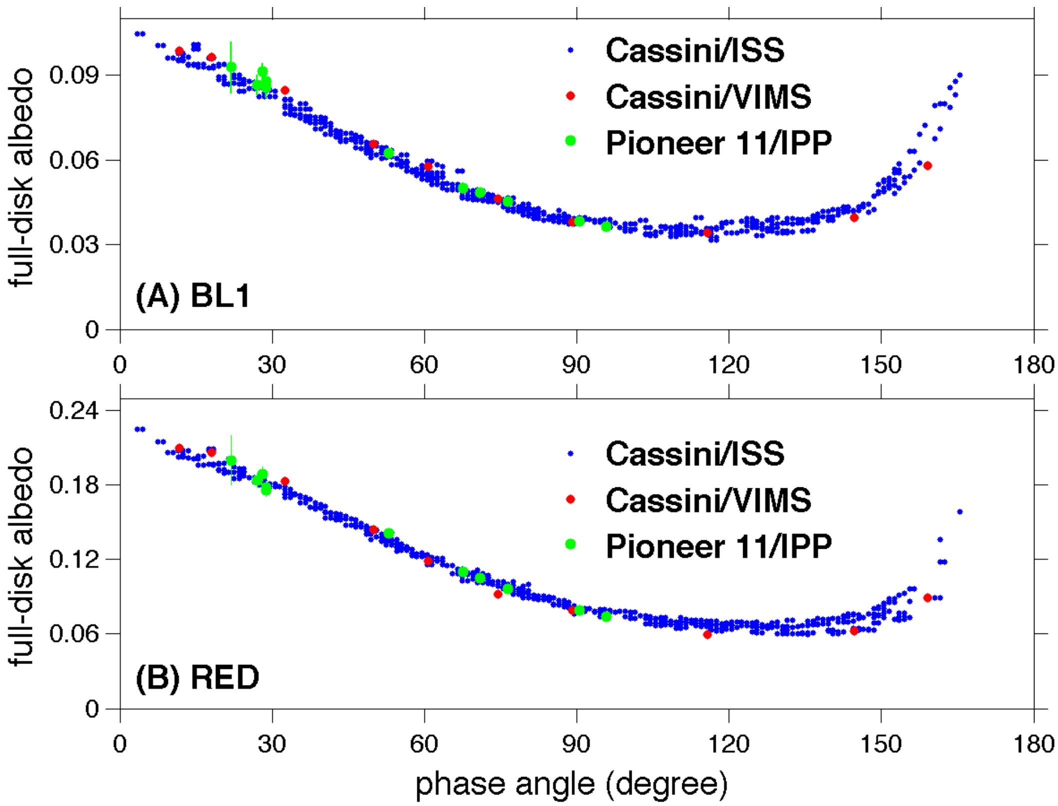

Figure S17. Comparison of Titan's full-disk albedo between the Cassini measurements (ISS and VIMS) and the Pioneer measurements. The Pioneer measurements at the blue (440 nm) and red (640 nm) wavelengths were conducted by the IPP on Pioneer 11 (please see Fig. S5 for more details). The VIMS measurements at 440 nm and 640 nm are plotted for comparison. The measurements based on the ISS BL1 (459 nm) and RED (649 nm) filters, which are close to the Pioneer blue and red wavelengths, are also plotted for comparison (see section "Validation of Cassini ISS and VIMS Results").

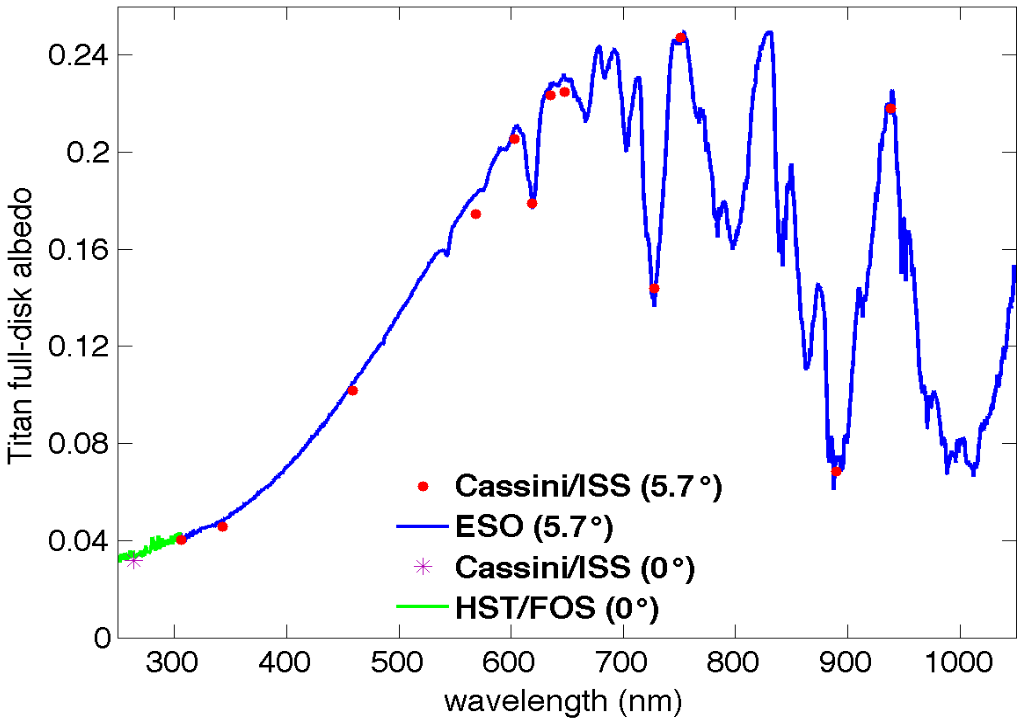

Figure S18. Comparison of Titan's full-disk albedo between the Cassini ISS observations and Earth-based observations. The ground-based ESO measurements in 1995 are used (see Fig. S3). Please note that the ESO measurements are based on the observations over Titan's disk with a solid radius (Fig. S3). We scale the results by the ratio between the ISS measurements with the solid radius and the ISS measurements with the effective radii. The ESO observations were conducted in the effective wavelength range 305-1050 nm with a phase angle ~ 5.7°, so we use the ISS observations with a phase angle 5.7° for comparison. The ISS UV1 (264 nm) filter is outside of the ESO wavelength range (305-1050 nm). So we use the observations from the HST/FOS (also see Fig. S4). The full-disk albedo from the HST was corrected to zero phase angle, so we use the ISS UV1 measurements at zero phase angle too.

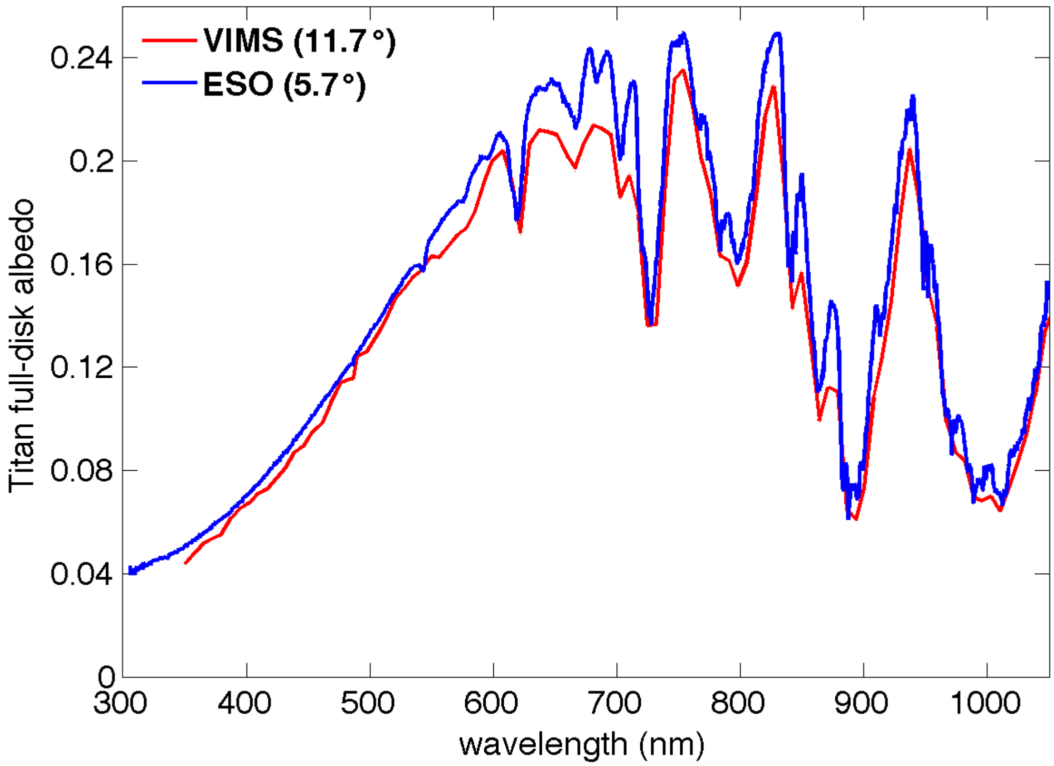

Figure S19. Comparison of Titan's full-disk albedo between the Cassini VIMS observations and Earth-based observations. Same as Fig. S18 except for the Cassini VIMS observations are compared with the Earth-based ESO observations in 1995 (40). Note the VIMS observations and the ESO observations have different phase angles (11.7° for VIMS and 5.7° for ESO) and spectral resolutions (~ 4-25 nm for VIMS and ~ 0.4 nm for ESO) (see section "Validation of Cassini ISS and VIMS Results" for more details).

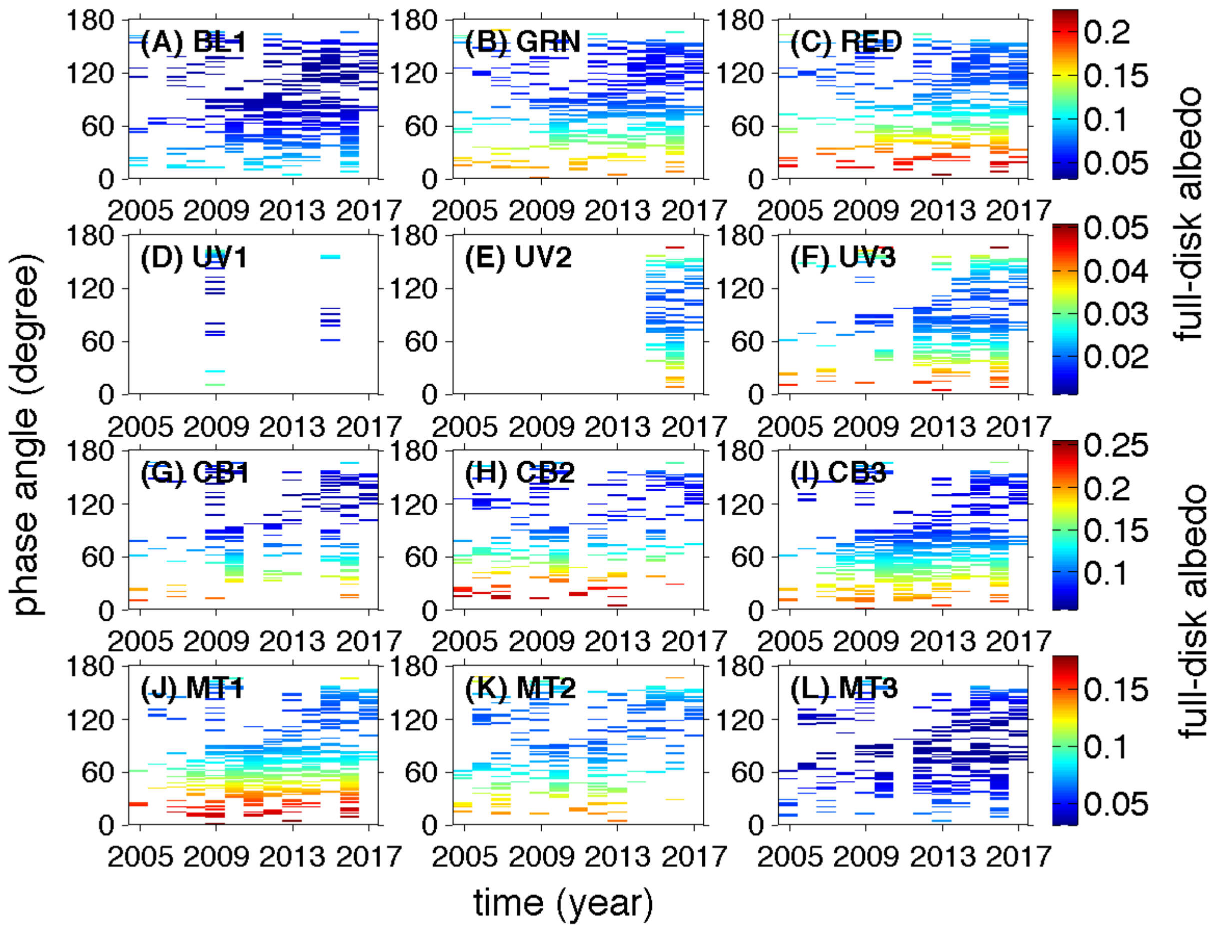

Figure S20. Titan's full-disk albedo from the observations recorded by the Cassini ISS 12 filters during the Cassini period of 2004-2017. (A) BL1 filter (459 nm); (B) GRN filter (569 nm); (C) RED filter (648 nm); (D) UV1 filter (264 nm); (E) UV2 filter (306 nm); (F) UV3 filter (343 nm); (G) CB1 fitler (CB1a ~ 635 nm and CB1b ~ 603 nm); (H) CB2 filter (751 nm); (I) CB3 fitler (939 nm); (J) MT1 fitler (619 nm); (K) MT2 filter (728 nm); (L) MT3 fitler (890 nm). The full-disk albedo functioning as phase angle is displayed in each year from 2004-05 to 2017. There are only three-month (October-December) high-quality observations in 2004, so the 2004 observations are combined with the 2005 observations. The blank areas are observational gaps.

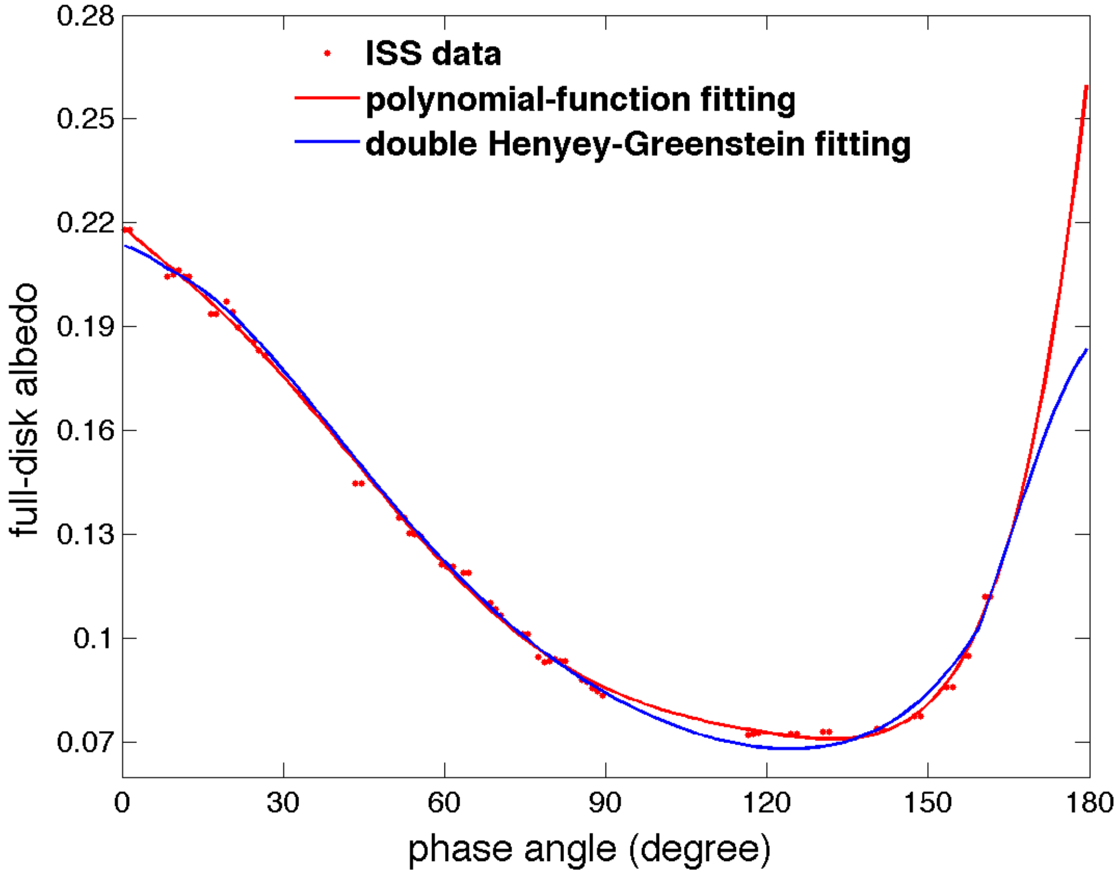

Figure S21. An example of fitting the phase function of Titan's full-disk albedo recorded by the Cassini ISS observations. The raw ISS data were recorded by the CB3 filter of the Cassini/ISS in 2009. A six-order polynomial function (red line) and the double H-G function (blue line) are used for fitting the ISS data (see section "Filling Observational Gaps in Phase Angle" for more details).

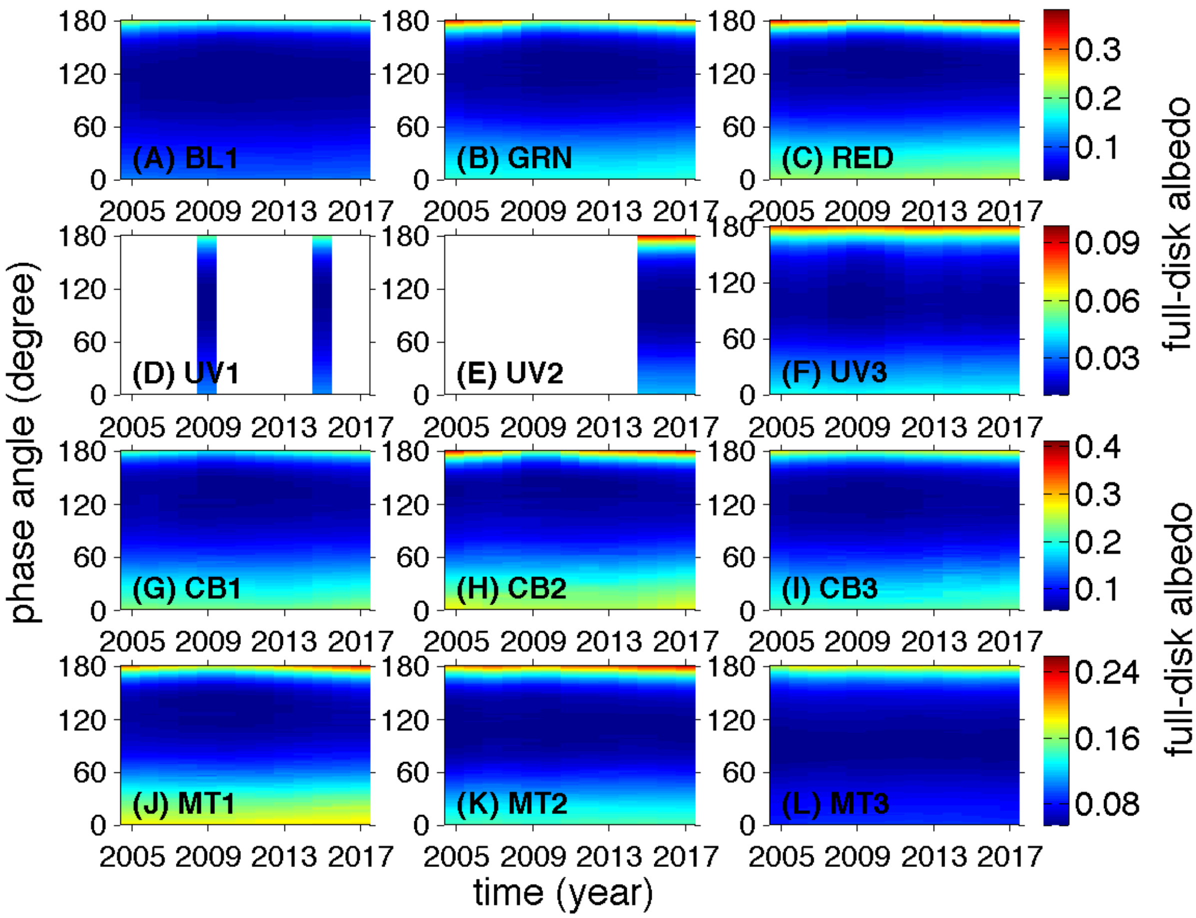

Figure S22. Fitting the phase functions of Titan's full-disk albedo recorded by the Cassini ISS 12 filters. (A) BL1 filter (459 nm); (B) GRN filter (569 nm); (C) RED filter (648 nm); (D) UV1 filter (264 nm); (E) UV2 filter (306 nm); (F) UV3 filter (343 nm); (G) CB1 fitler (CB1a ~ 635 nm and CB1b ~ 603 nm); (H) CB2 filter (751 nm); (I) CB3 fitler (939 nm); (J) MT1 fitler (619 nm); (K) MT2 filter (728 nm); (L) MT3 fitler (890 nm).

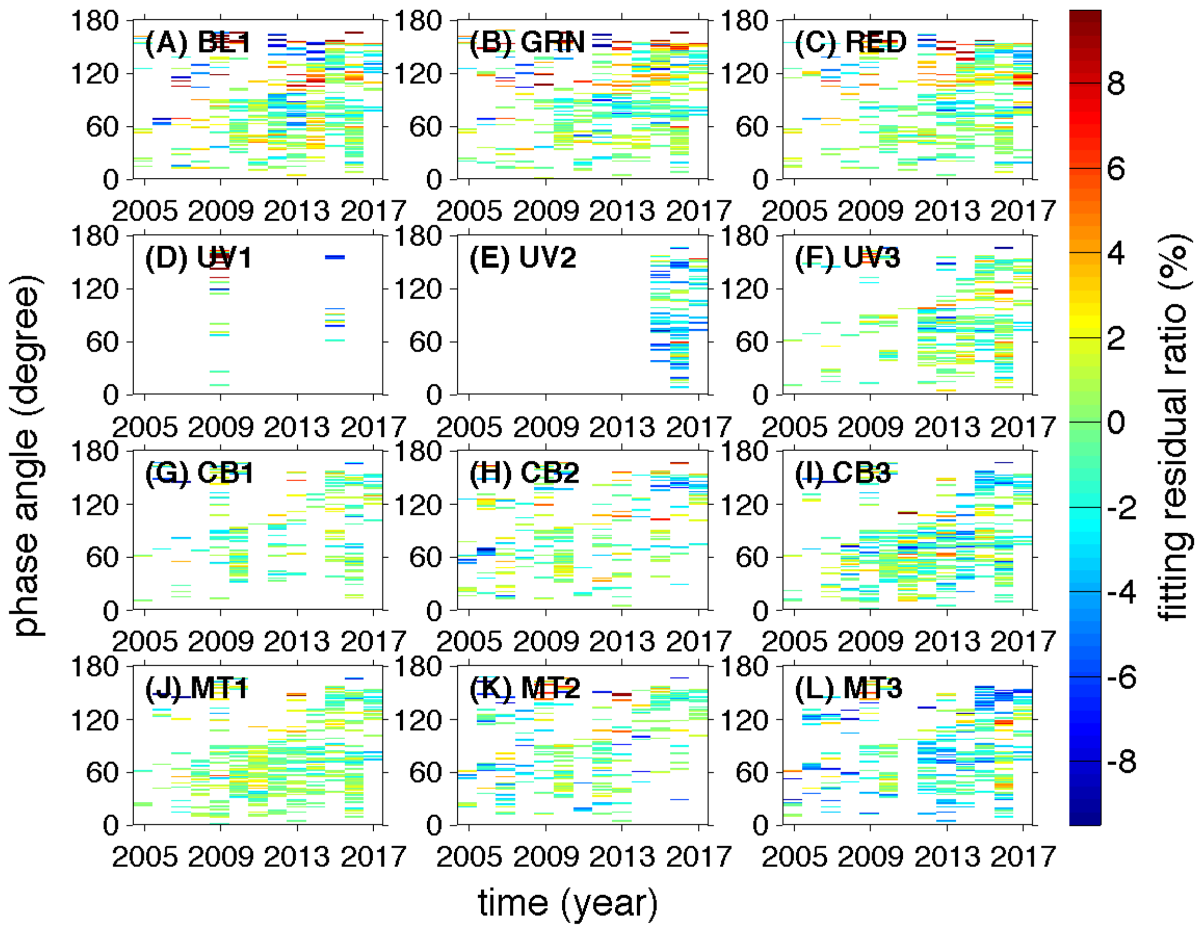

Figure S23. Ratios between fitting residuals and observed albedos for the ISS 12 filters. The fitting residual is defined as the difference between fitted albedo (Fig. S22) and the observed albedo (Fig. S20). (A) BL1 filter (459 nm); (B) GRN filter (569 nm); (C) RED filter (648 nm); (D) UV1 filter (264 nm); (E) UV2 filter (306 nm); (F) UV3 filter (343 nm); (G) CB1 fitler (CB1a ~ 635 nm and CB1b ~ 603 nm); (H) CB2 filter (751 nm); (I) CB3 fitler (939 nm); (J) MT1 fitler (619 nm); (K) MT2 filter (728 nm); (L) MT3 fitler (890 nm).

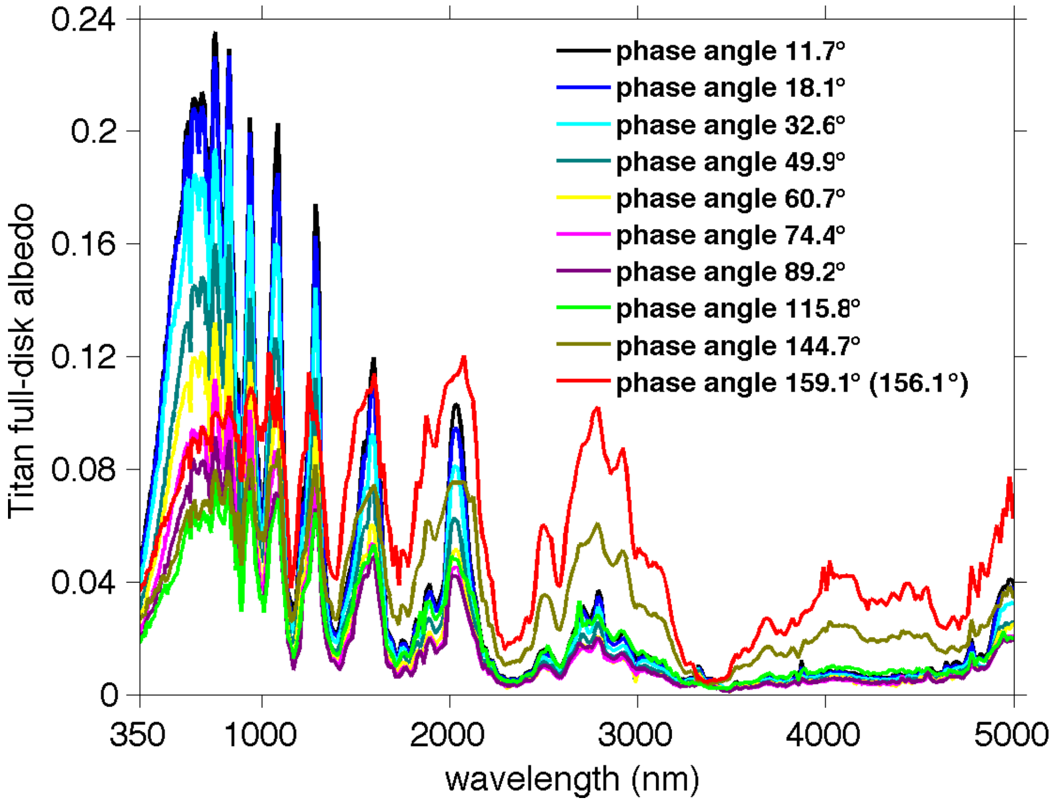

Figure S24. Titan's full-disk albedo observed by the Cassini VIMS. The times (spatial resolutions) for the VIMS observations with phase angles 11.7°, 18.1°, 32.6°, 49.9°, 60.7°, 74.4°, 89.2°, 115.8°, and 144.7° are 2007 (206 km/pixel), 2006 (191 km/pixel), 2007 (147 km/pixel), 2007 (178 km/pixel), 2006 (139 km/pixel), 2008 (147 km/pixel), 2008 (161 km/pixel), 2006 (206 km/pixel), and 2007 (129 km/pixel), respectively. The largest phase angles of the high-quality VIMS observations are 159.1° and 156.1° for the visible part (~350-1046 nm) and the infrared part (~1046-5131 nm), respectively. The observations with the phase angle 159.1° (visible part) were recorded in 2007 with a spatial resolution ~ 151 km/pixel. The observations with the phase angle 156.1° (infrared part) were recorded in 2012 with a spatial resolution ~ 126 km/pixel. We combine the visible spectra at 159.1° and the infrared spectra at 156.1° together (red line).

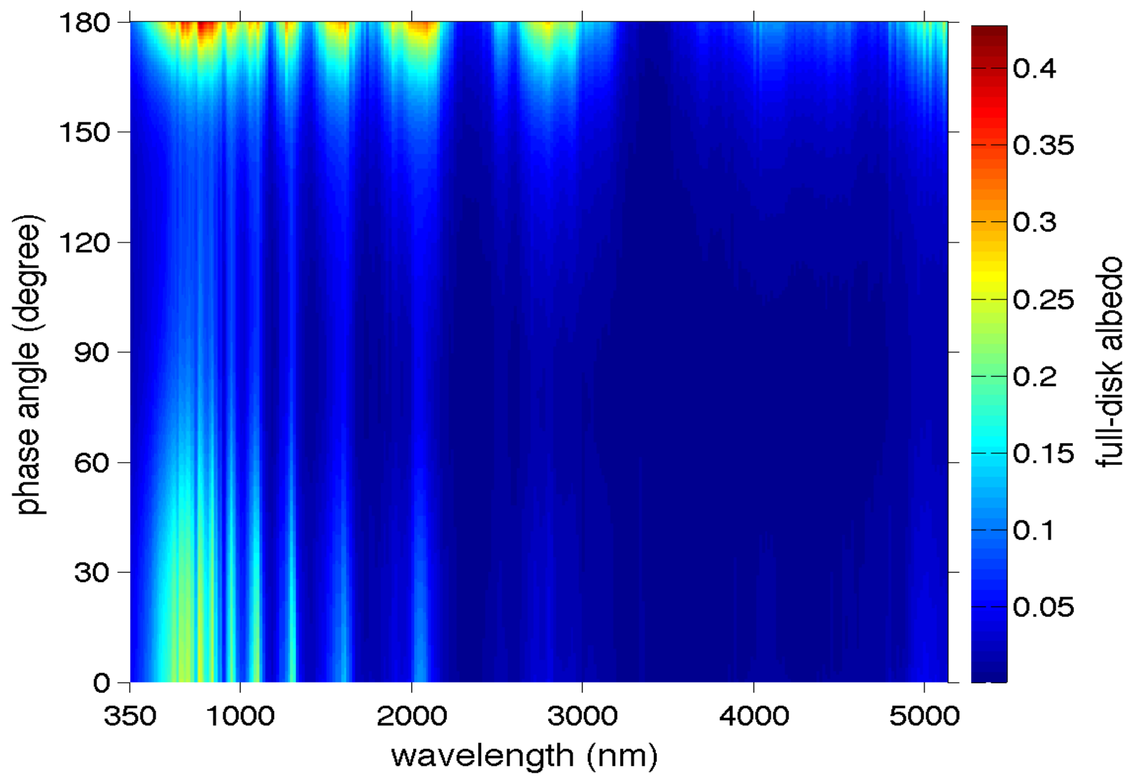

Figure S25. Fitting the phase function of Titan's full-disk albedo by the VIMS observations (350-5131 nm). The VIMS observational gaps with phase angles smaller than 11.7° and larger than 159.1° are filled by the ISS data before the least-squares fitting (see section "Filling Observational Gaps in Phase Angle").

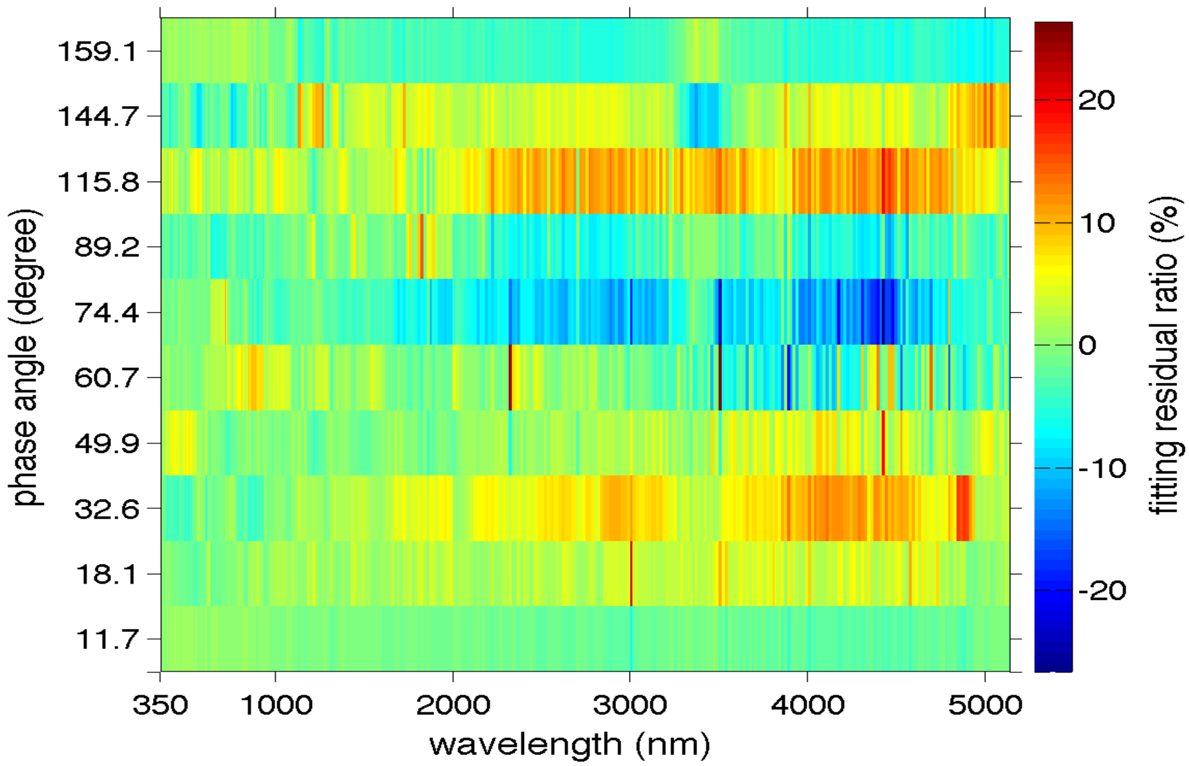

Figure S26. Ratio between fitting residual and observed albedo for the VIMS observations. The fitting residual is defined as the difference between fitted albedo (Fig. S25) and the observed albedo (Fig. S24). Please note that the phase angle 159.1° in y axis is for the VIMS visible part (350-1046 nm) only. The VIMS infrared part (1046-5131 nm) has a phase angle 156.1° (see Fig. S24).

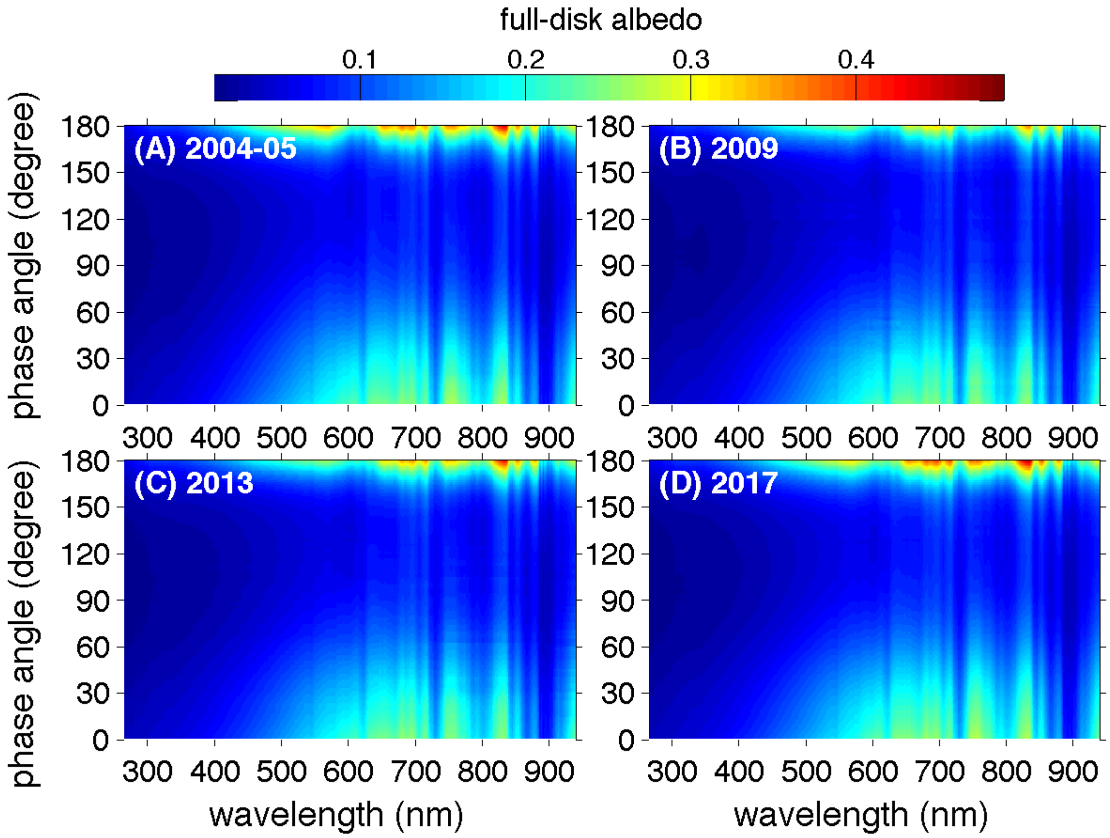

Figure S27. ISS-derived albedo in the two-dimensional domain of phase angle (0-180°) and wavelength (264-939 nm) during the Cassini epoch. The derived albedo is based on the ISS fitted phase functions in Fig. S22 and reference albedo spectra with a high spectral resolution shown in Fig. S3 (40) (see section "Filling Observational Gaps in Wavelength and Time"). Titan's two-dimensional albedo in each year of the Cassini period of 2004-2017 is derived. Here, only four years (2004-05, 2009, 2013, and 2017) are shown as examples.

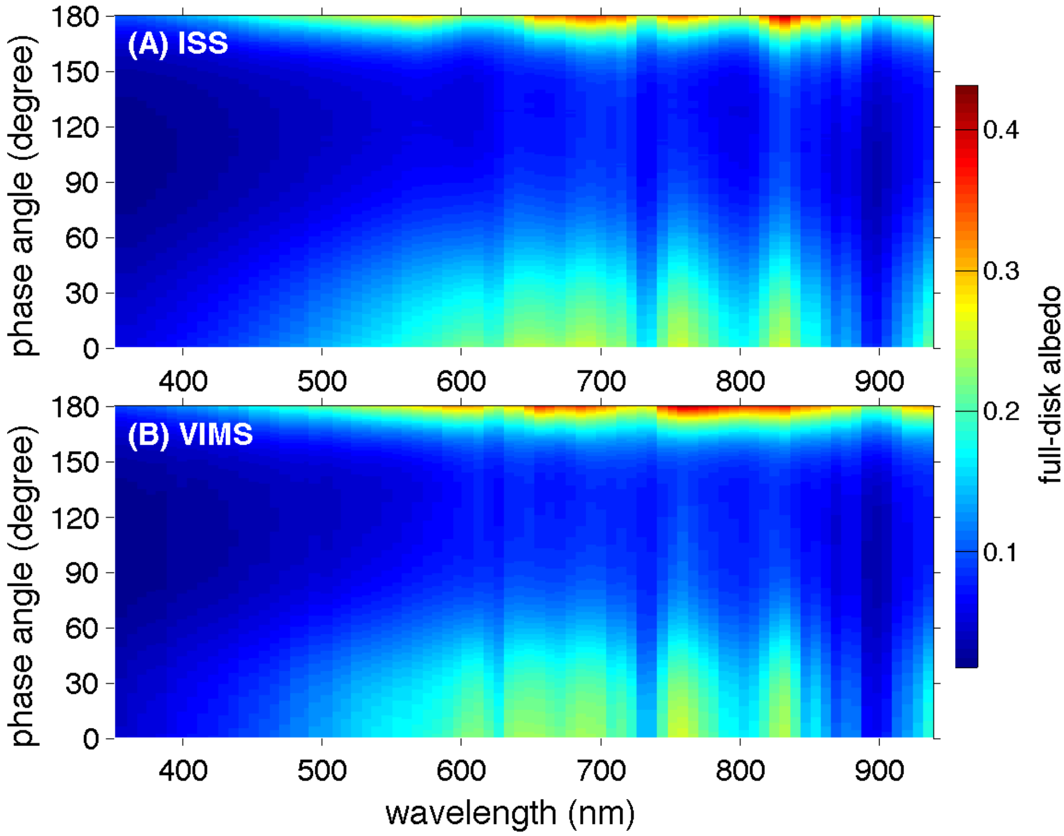

Figure S28. Comparison of Titan's albedo between the ISS derived results and the VIMS fitted results for the overlap wavelengths (~ 350-939 nm). (A) The ISS derived albedo. Panel A shows the time-mean albedo, which is averaged over the Cassini epoch (2004-2017) (see Fig. S27). (B) The VIMS fitted albedo. The VIMS results come from Fig. S25.

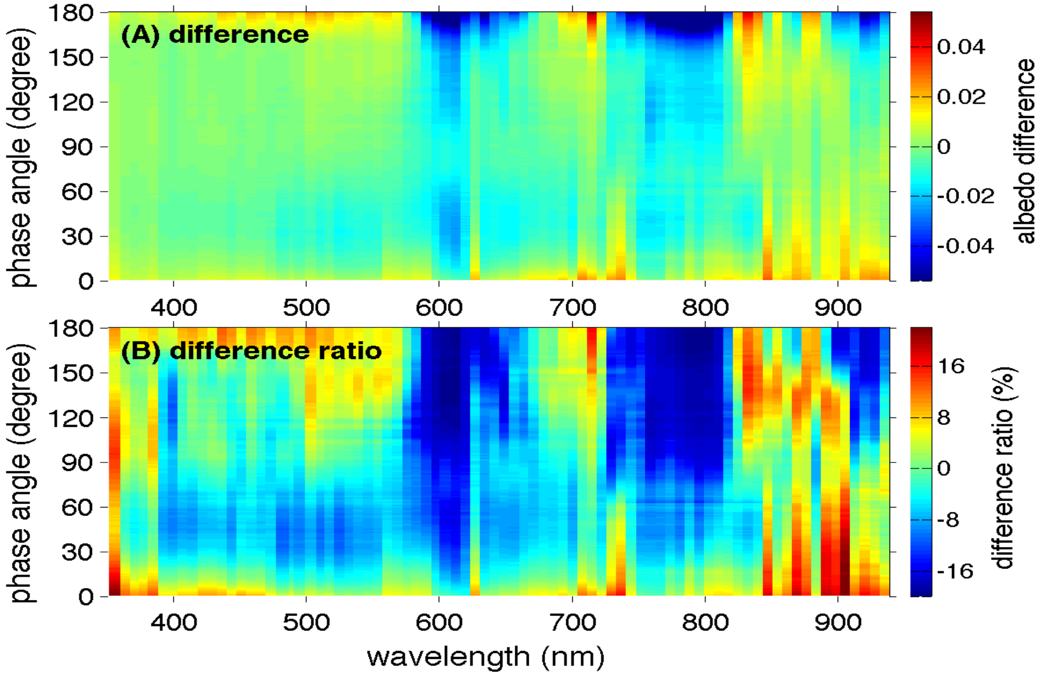

Figure S29. Difference of Titan's albedo between the ISS derived results and the VIMS fitted results. (A) Difference of Titan's albedo between the ISS results (panel A of Fig. S28) and the VIMS results (panel B of Fig. S28). (B) Difference ratio. The difference ratio is defined as the ratio between the difference (panel A) and the mean value.

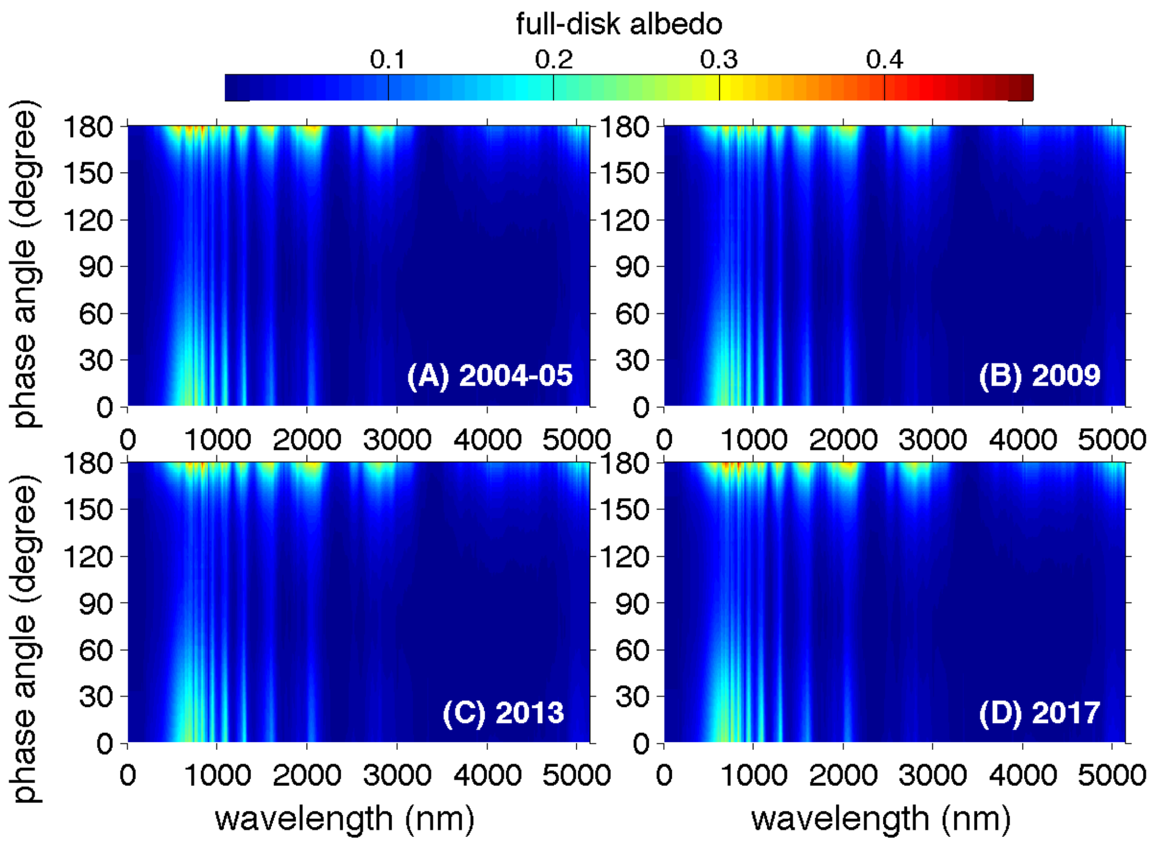

Figure S30. Titan's albedo in the complete wavelength range 0-5131 nm during the Cassini epoch. The time-varying albedo in the wavelength range 264-939 nm comes from Fig. S27. The time-varying albedo in the wavelength range 939-5131 nm (outside of the ISS wavelength range but in the VIMS wavelength range) is based on the VIMS fitted results (Fig. S25) and assume the VIMS results have the same temporal variations of those of the ISS CB3 results at 939 nm. The time-varying albedo in the wavelength range 0-264 nm (uncovered by the Cassini ISS & VIMS observations) is based on the albedo spectra from Cassini/UVIS (150-190 nm) the HST/FOS (190-264 nm) and assume that the albedo spectra in the wavelength range 0-150 nm has the same albedo as that at 150 nm. In addition, the phase functions and the corresponding temporal variations from the ISS UV1 (264 nm) observations are used to approximate the phase functions and their temporal variations in the wavelength range 0-264 nm (see section "Filling Observational Gaps in Wavelength and Time").

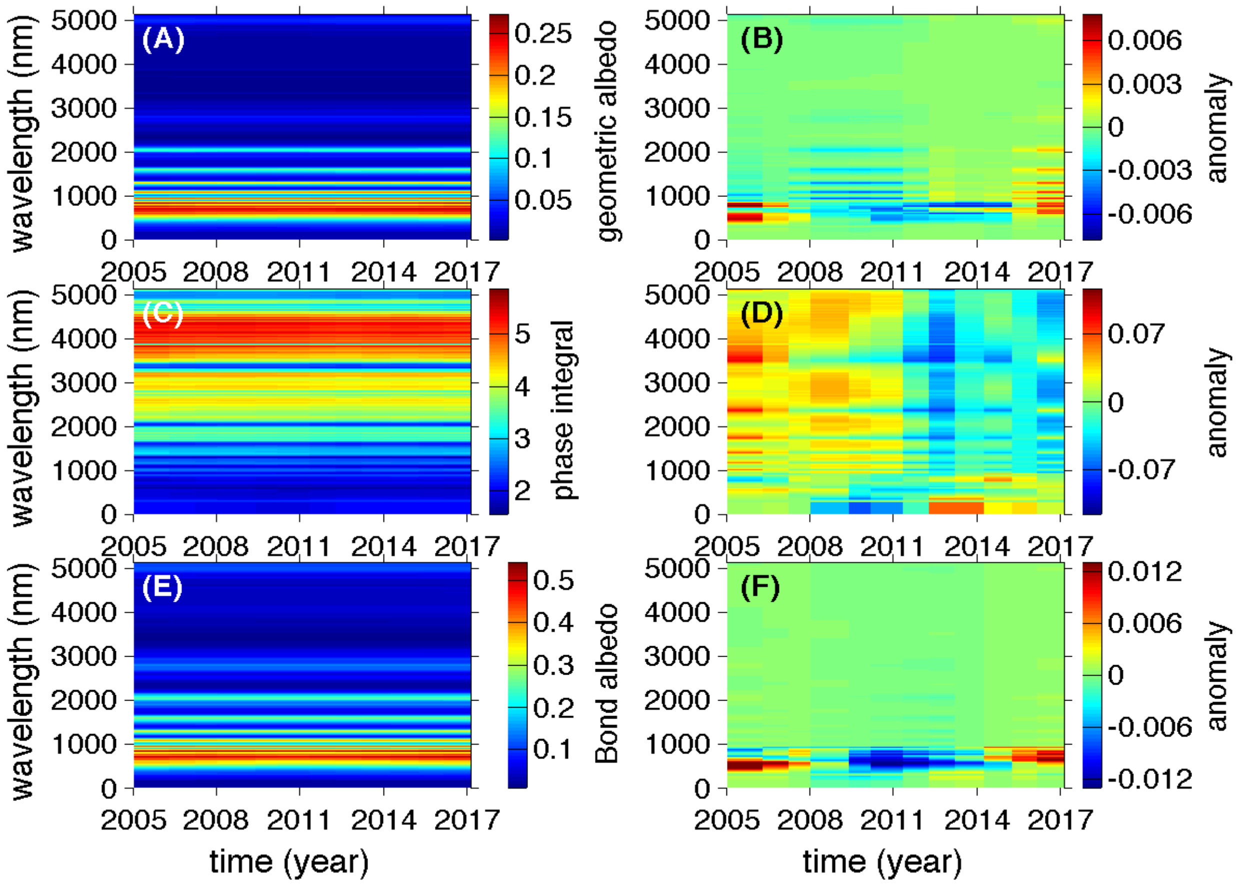

Figure S31. Titan's monochromatic geometric albedo, phase integral, and Bond albedo in the wavelength range 0-5131 nm during the Cassini epoch. Panels (A) and (B) are monochromatic geometric albedo and anomaly (i.e., difference from time-mean), respectively. Panels (C) and (D) are monochromatic phase integral and anomaly, respectively. Panels (E) and (F) are monochromatic Bond albedo and anomaly, respectively.

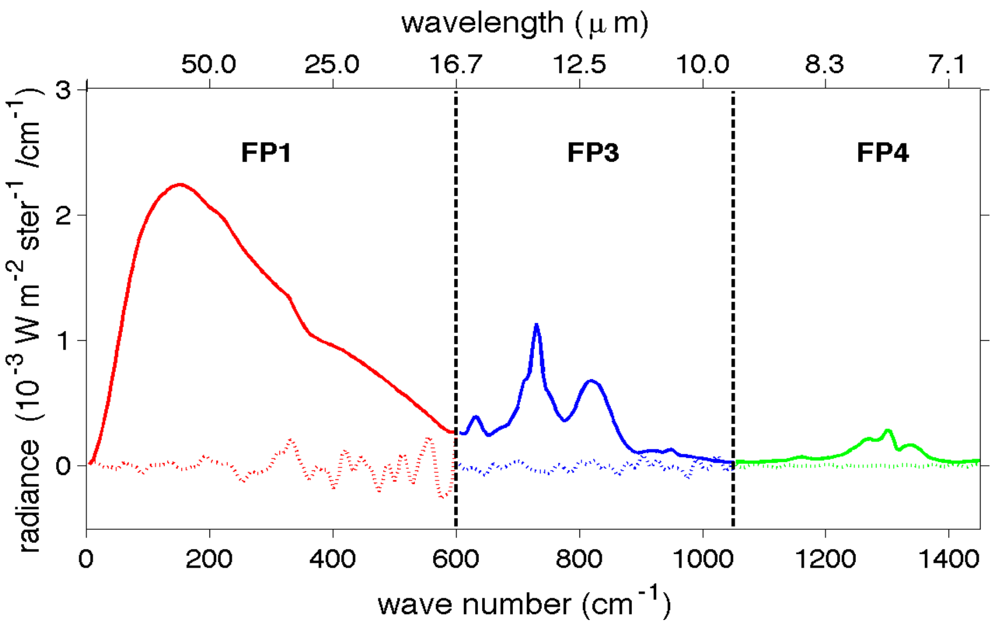

Figure S32. Comparison between typical spectra of Titan (solid line) and typical spectra of deep space (dashed line). Both spectra of Titan and deep space were recorded by the three focal planes of the Cassini/CIRS in 2011 with a spectral resolution 5 cm^{-1}.

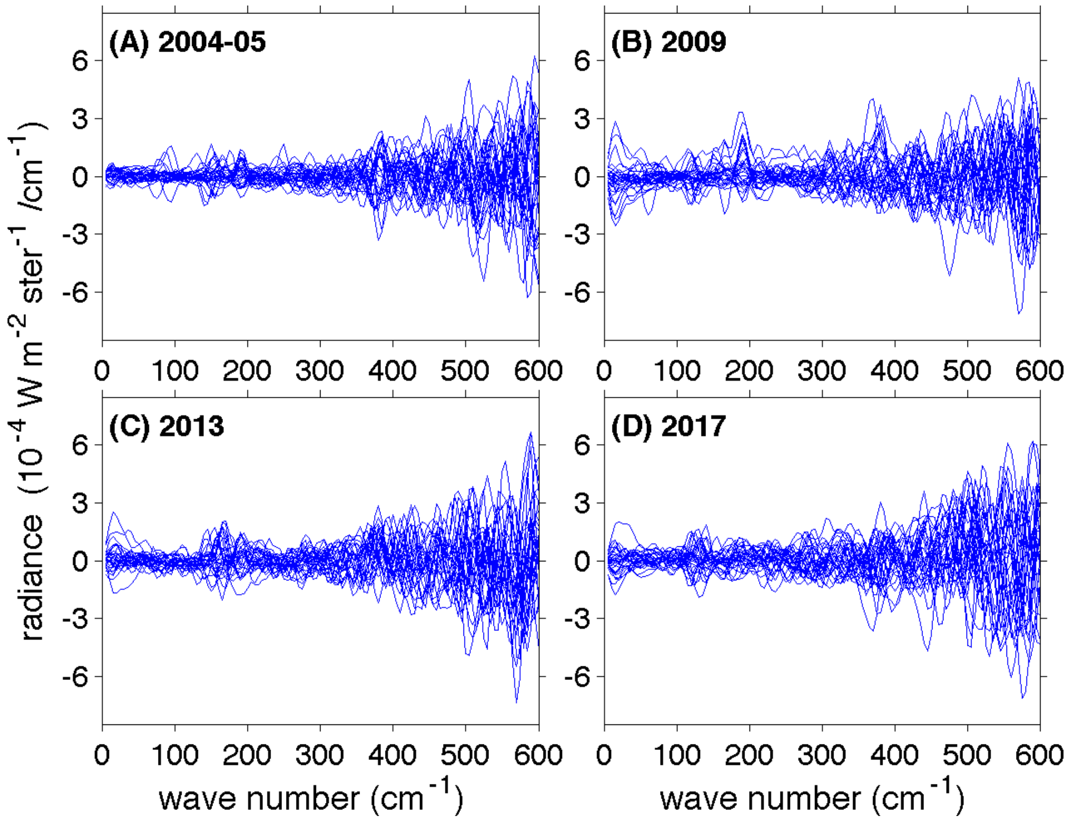

Figure S33. Spectra of deep space in different years. For each year, 100 spectra of deep space were plotted.

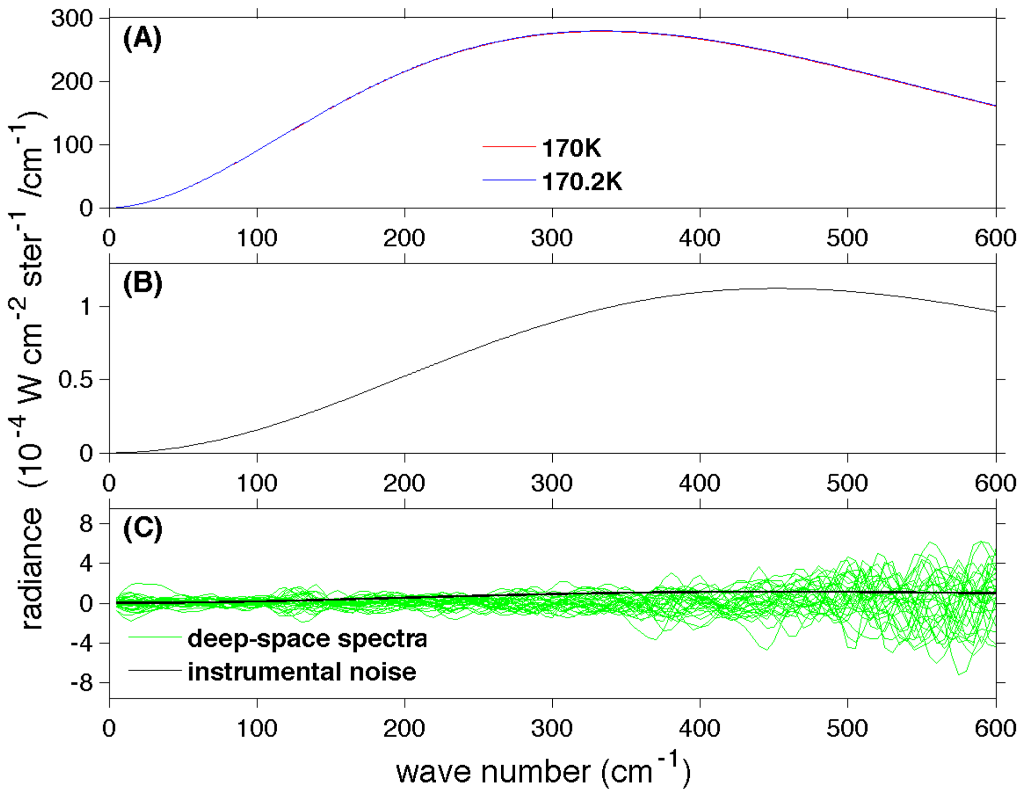

Figure S34. Comparison between the spectral noise related to the temporal control of the CIRS instrument and the spectra of deep space. (A) Spectra of the designed temperature of the CIRS instrument (170 K) and the possible temperature of the CIRS instrument with the temperature control (170.2 K). (B) Difference of the two spectra shown in panel A, which is defined as the spectra noise related to the temporal control of the CIRS instrument. (C) Comparison between spectral noise and typical spectra of deep space.

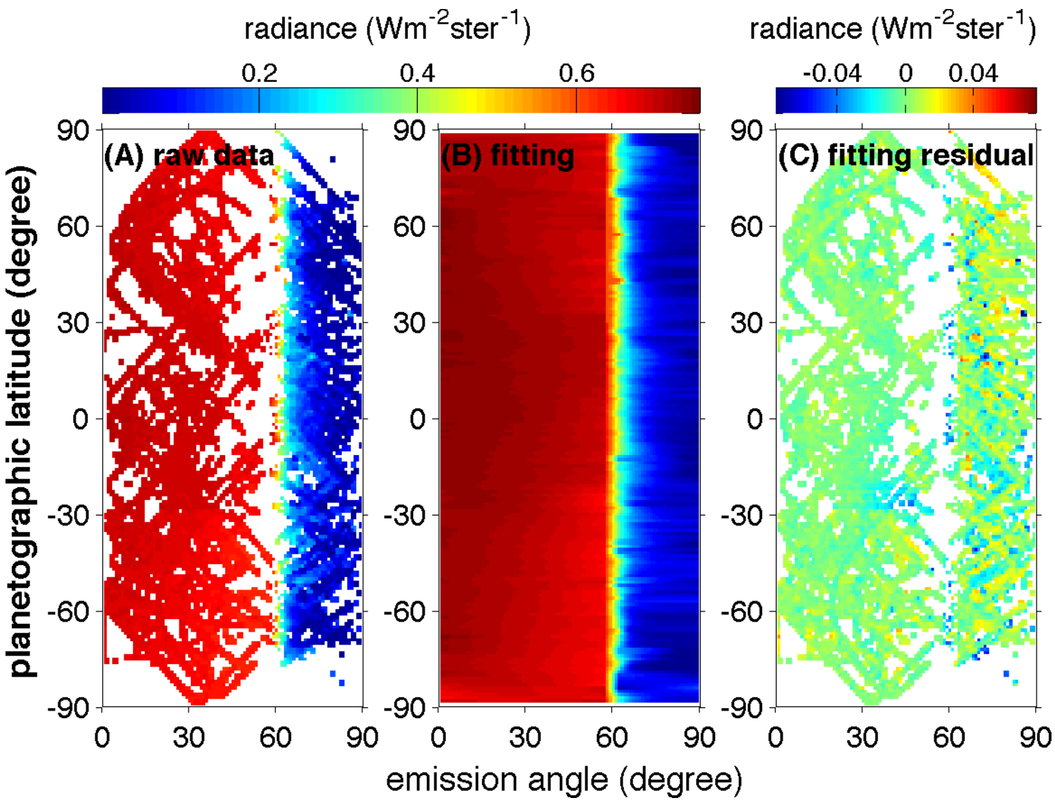

Figure S35. Examples of fitting CIRS data. (A) Raw data. (B) Least squares fitting. (C) Fitting residual. Fitting residual is defined as the difference between the fitted values and raw data.

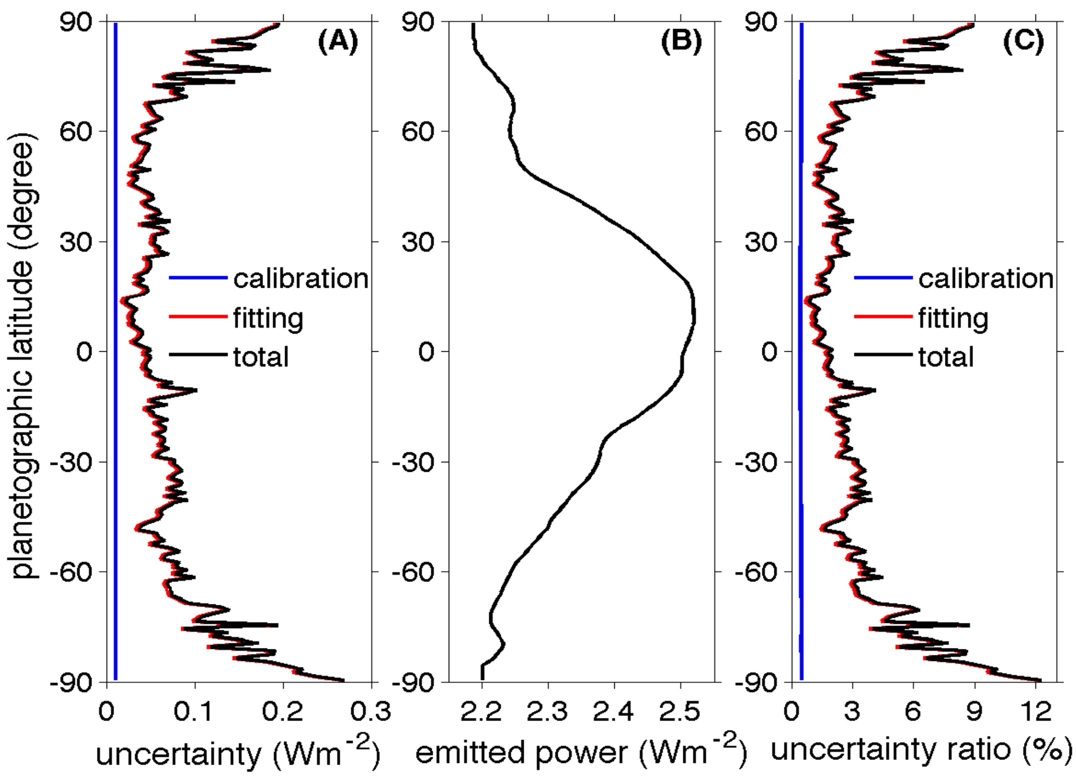

Figure S36. Examples of uncertainties in the measurements of Titan's emitted power. The uncertainty analysis for the CIRS measurements of Titan's emitted power in 2009 is shown. (A) Uncertainties. (B) Titan's emitted power. (C) Ratio between uncertainties (panel A) and the corresponding emitted power (panel B).

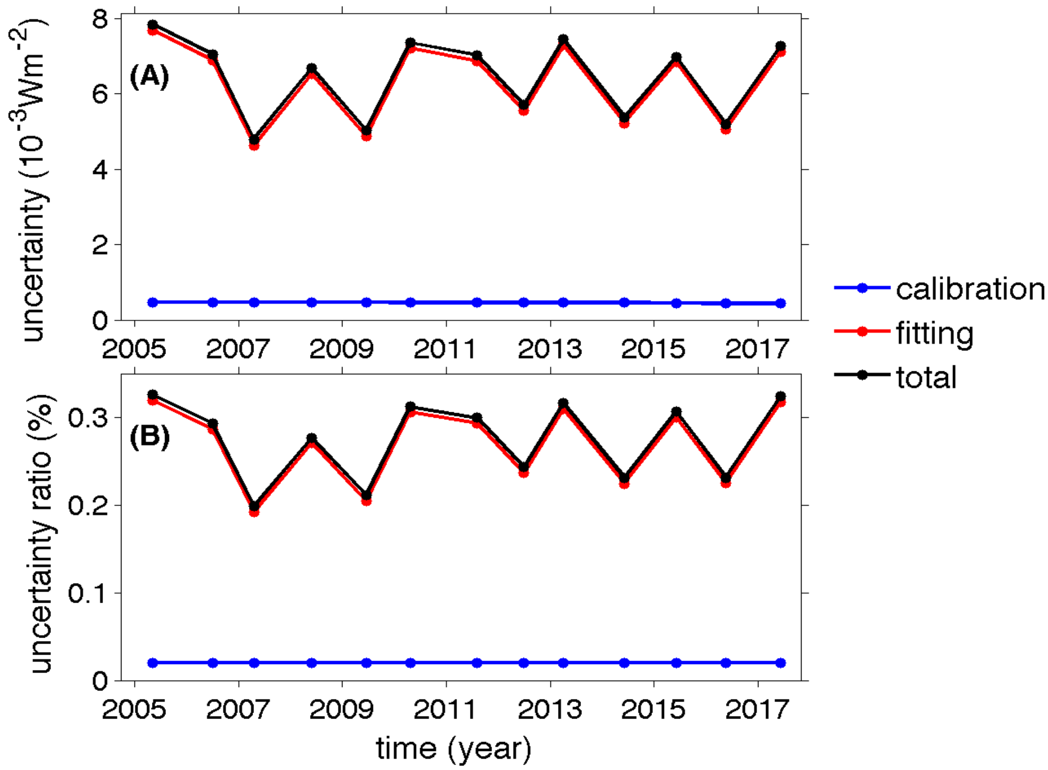

Figure S37. Uncertainties in the measurements of Titan's emitted power during the Cassini epoch. (A) The absolute uncertainties in the measurements of Titan's emitted power. (B) The ratio between the uncertainties (panel A) and Titan's emitted power.

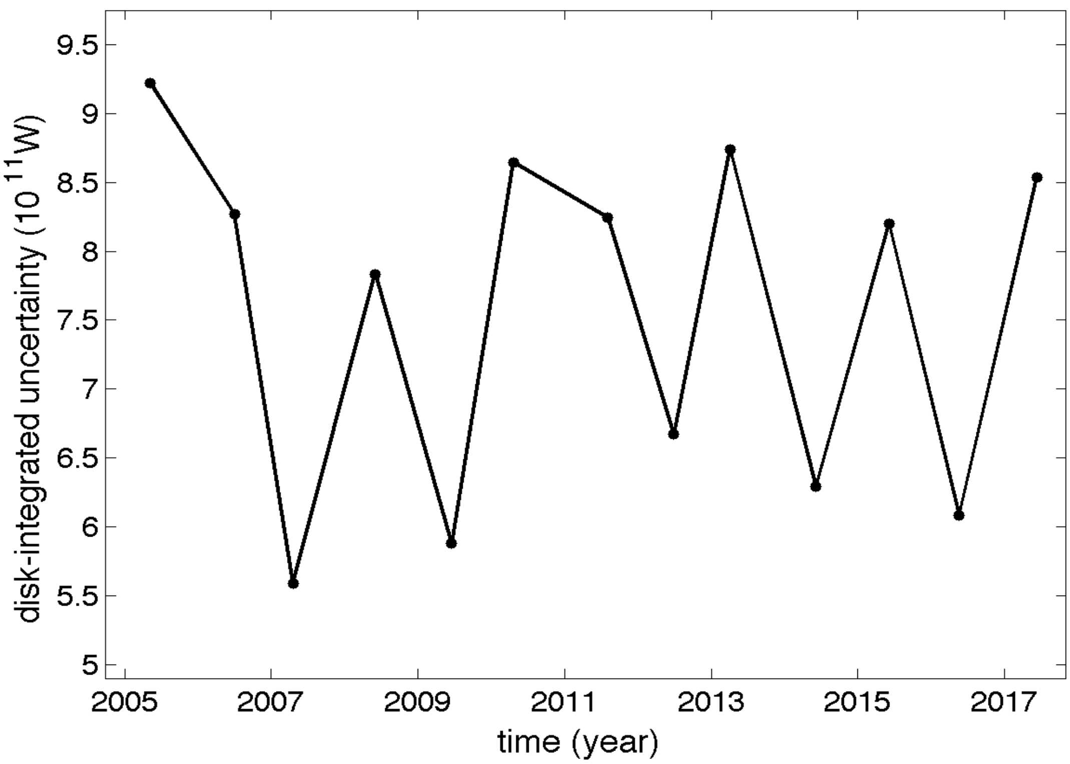

Figure S38. Uncertainties in the measurements of Titan's sphere-integrated emitted power during the Cassini epoch. The uncertainties in the emitted power over a unit area (Fig. S37) are integrated over a sphere with a effective radius 2757+500 km (where 2757 is the radius of solid Titan and 500 km is the effective height to capture all important thermal emission sources).

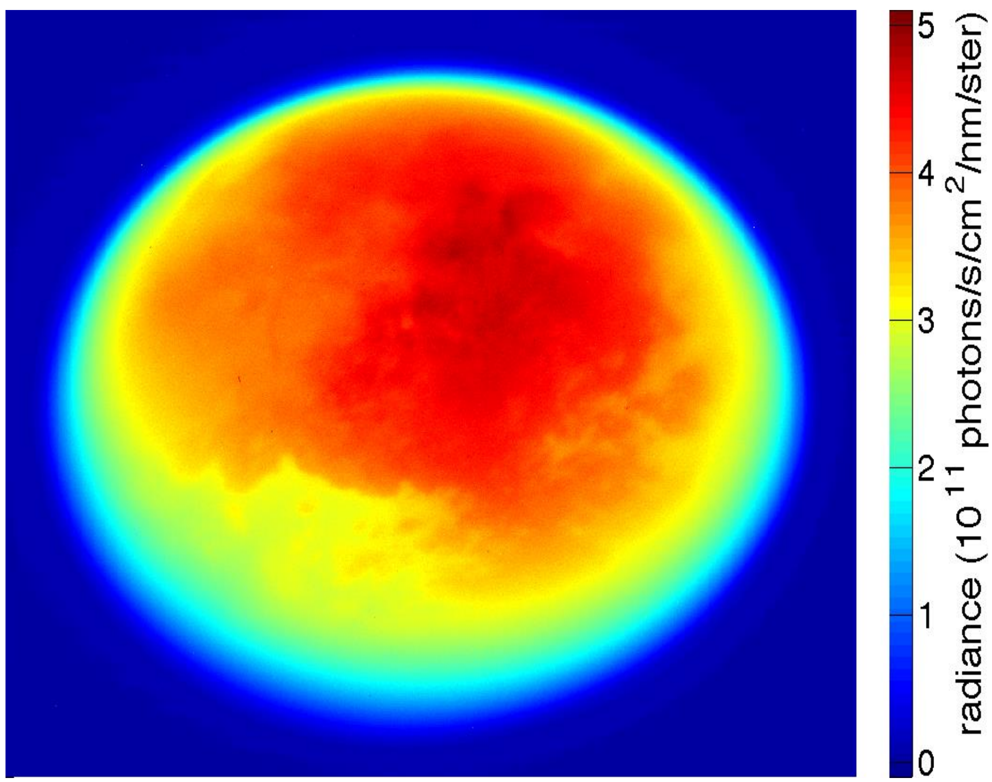

Figure S39. Example of ISS calibrated images with a unit of radiance. The raw image was taken by the ISS CB3 filter on December 11, 2004 with a phase angle ~ 18.15° and a spatial resolution ~ 6.5 km/pixel. The ISS raw images are calibrated by the latest version of the Cassini ISS calibration software.

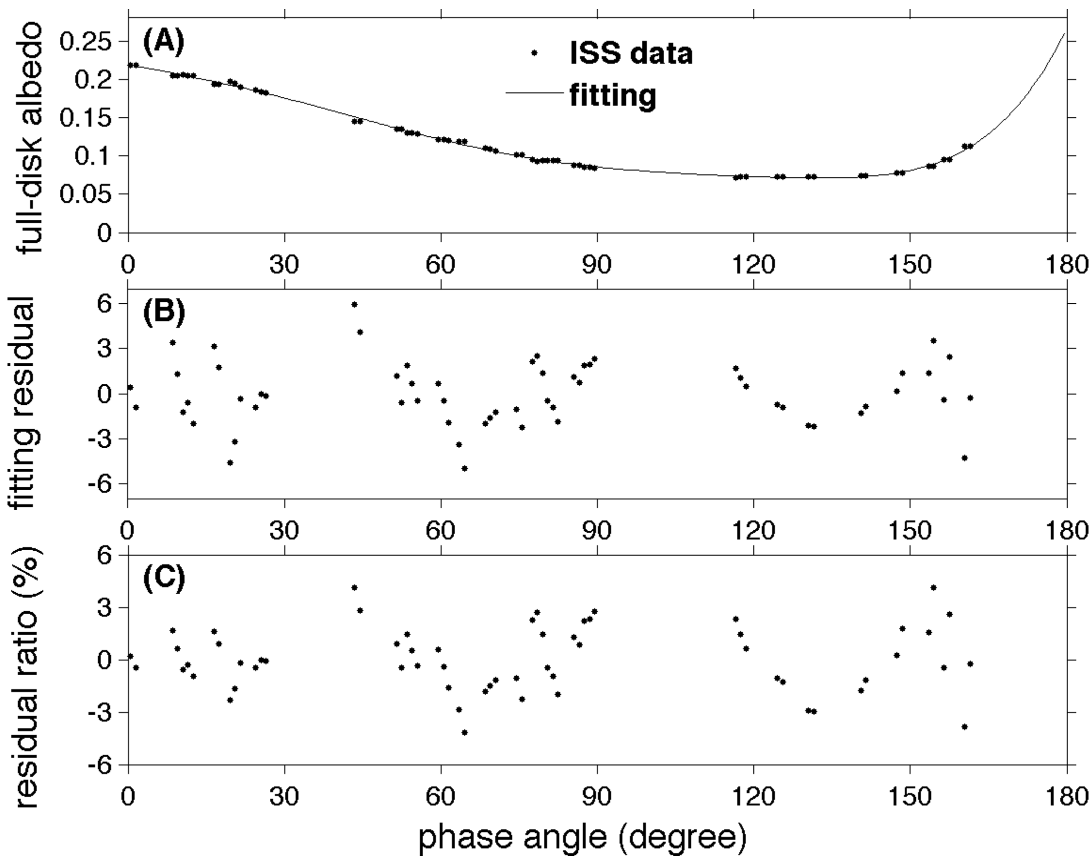

Figure S40. Examples of ISS data fitting and fitting residual. (A) Data fitting shown in Fig. S21. (B) Fitting residuals, which are defined as the difference between the fitting values and raw data. (C) Ratios between fitting residuals and raw data.

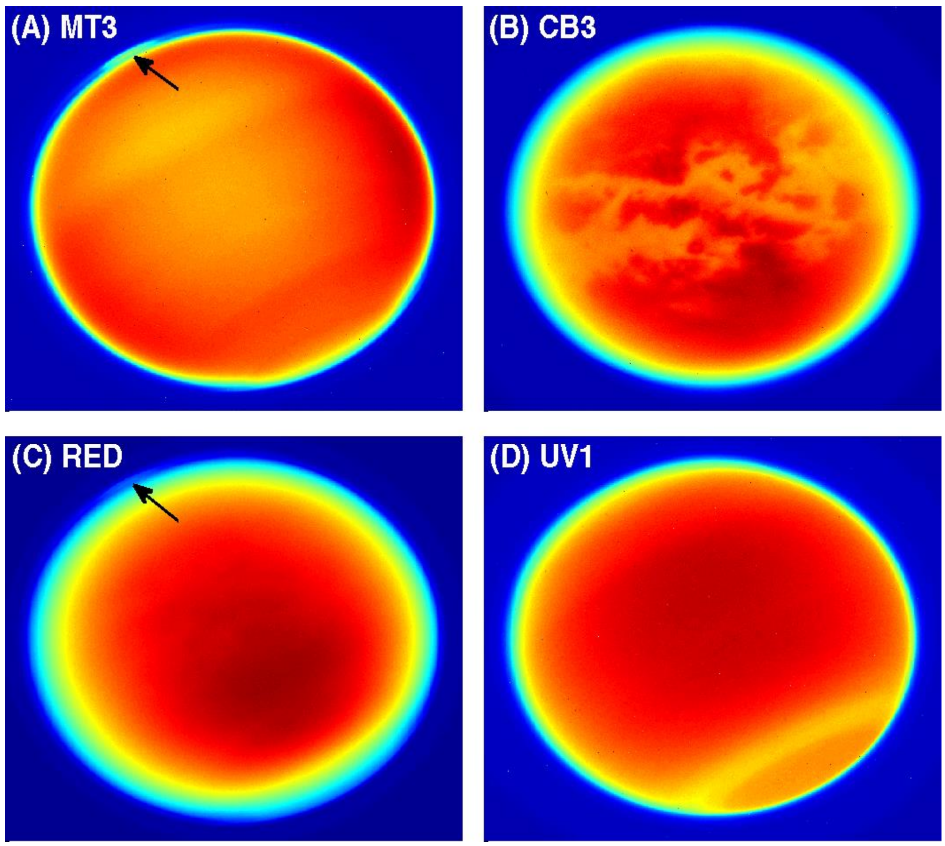

Figure S41. High-altitude haze shown in some filters of the Cassini ISS images. The raw images recorded by the ISS MT3 (panel A), RED (panel C), and UV1 (panel D) filters were taken on April 13, 2013 with a spatial resolution ~ 10.77 km/pixel and a phase angle ~ 4.27°. The image recorded by CB3 filter (panel B) was taken on August 27, 2009 with a spatial resolution ~ 8.62 km/pixel and a phase angle ~ 0.75°. The high-altitude haze is pointed by arrows in panels A and C.

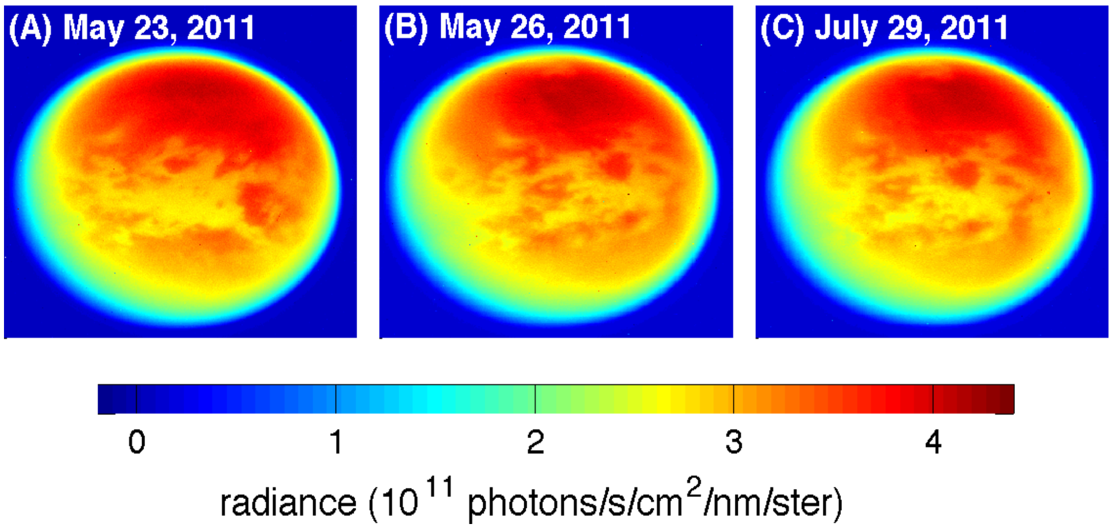

Figure S42. Titan's reflectivity and time variations seen in ISS images at different longitudes and times. All three images in panels A, B, and C were recorded by the ISS CB3 filter with the same phase angle ~ 14°. The spatial resolutions for the three images are 8.84 km/pixel, 17.56 km/pixel, and 18.64 km/pixel, respectively.

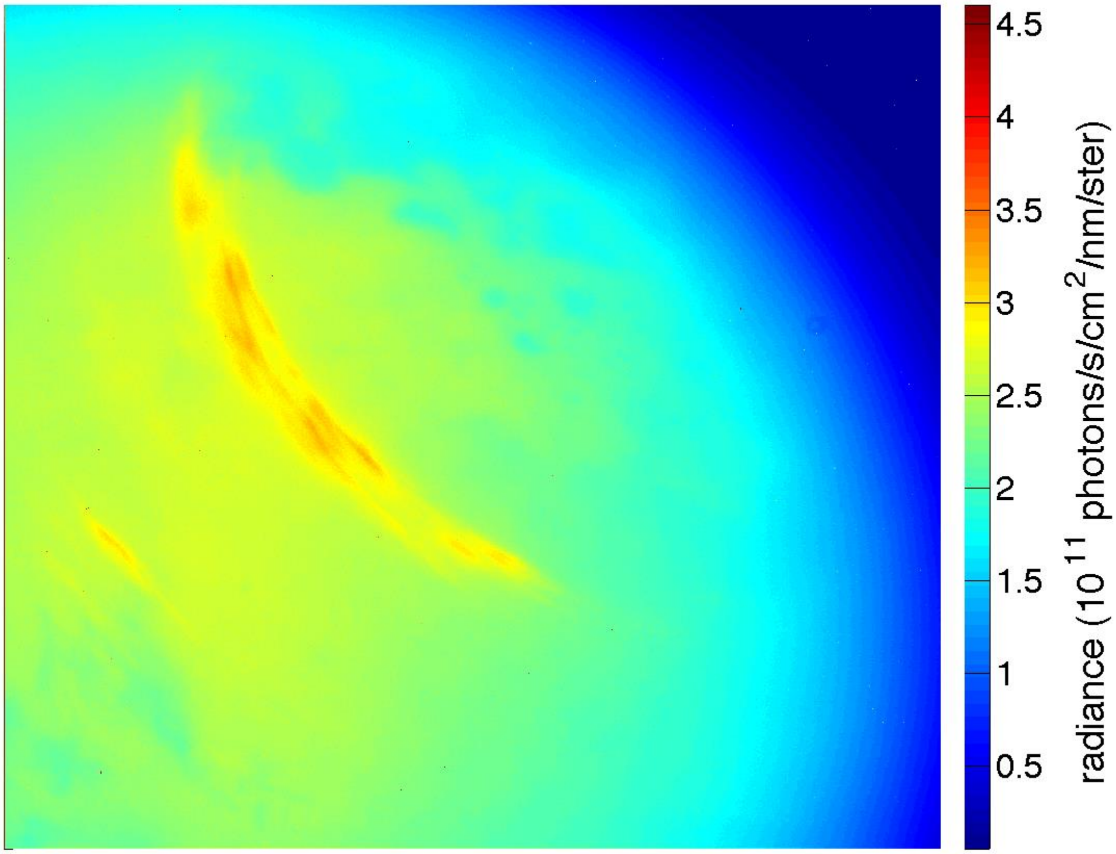

Figure S43. An example of cloud bands on Titan. The raw image was taken by the ISS CB3 filter on May 6, 2017 with a phase angle ~ 14.3° and a spatial resolution ~ 3.1 km/pixel. The ISS raw images are calibrated by CISSCAL software.

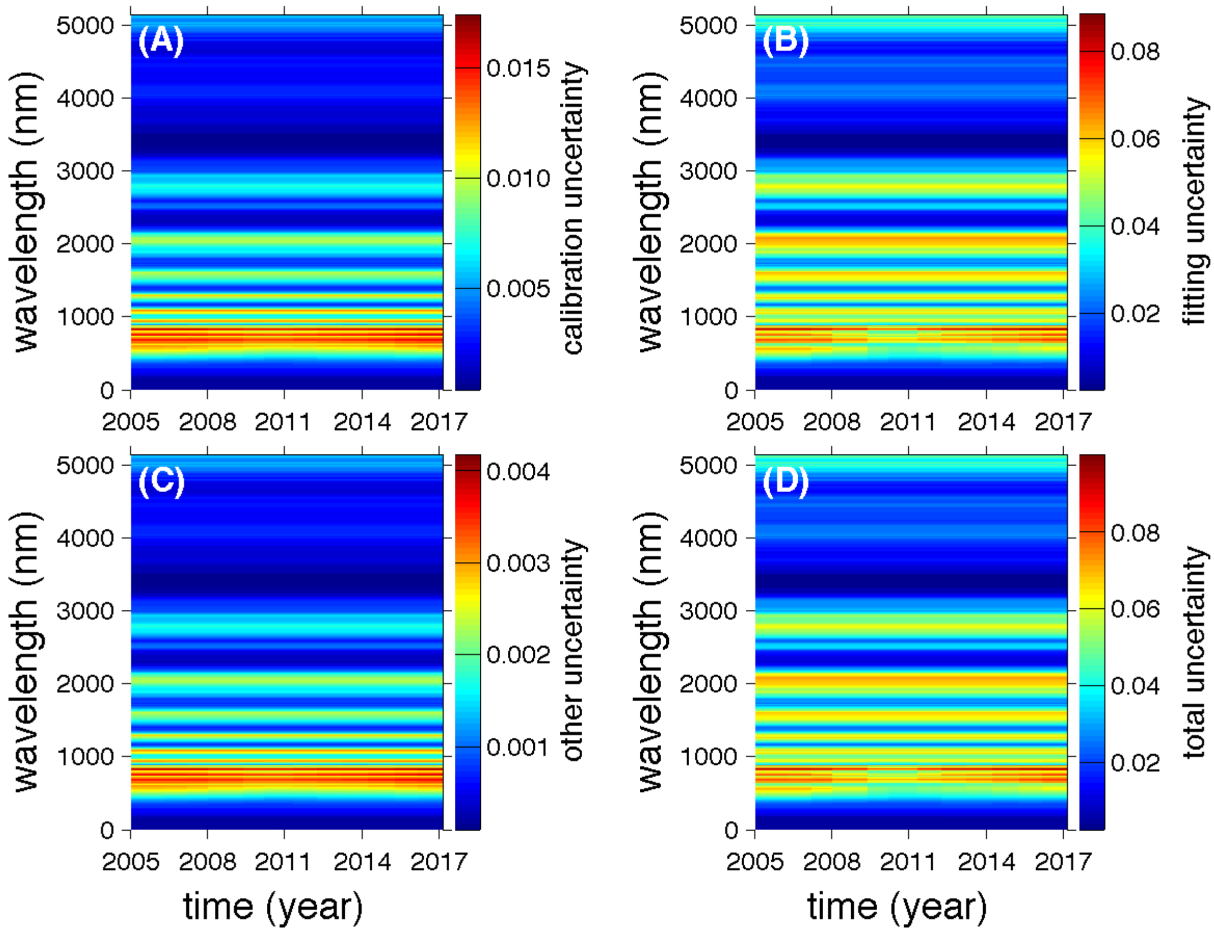

Figure S44. Spectral distribution of the uncertainties in the measurements of monochromic Bond albedo during the Cassini epoch (2004-2017). (A) Uncertainty related to the Cassini data calibration. (B) Uncertainty related to filling observational gaps in phase angle. (C) Uncertainty from other error sources. (D) Total uncertainty by combining the uncertainties in panels A, B, and C.

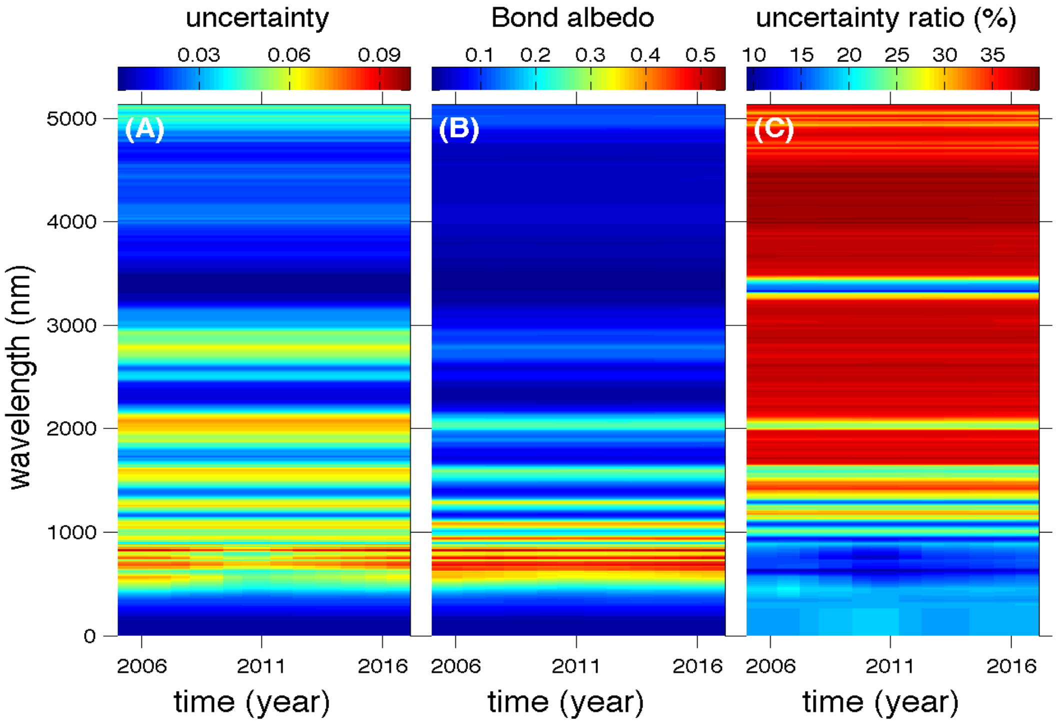

Figure S45. Ratio between the total uncertainty and the corresponding monochromatic Bond albedo during the Cassini epoch (2004-2017). (A) Total uncertainty. (B) Bond albedo. (C) Ratio between the total uncertainty (panel A) and the corresponding monochromatic Bond albedo (panel B). Panels A and B are the same as panel D of Fig. S43 and panel E of Fig. S31, respectively.

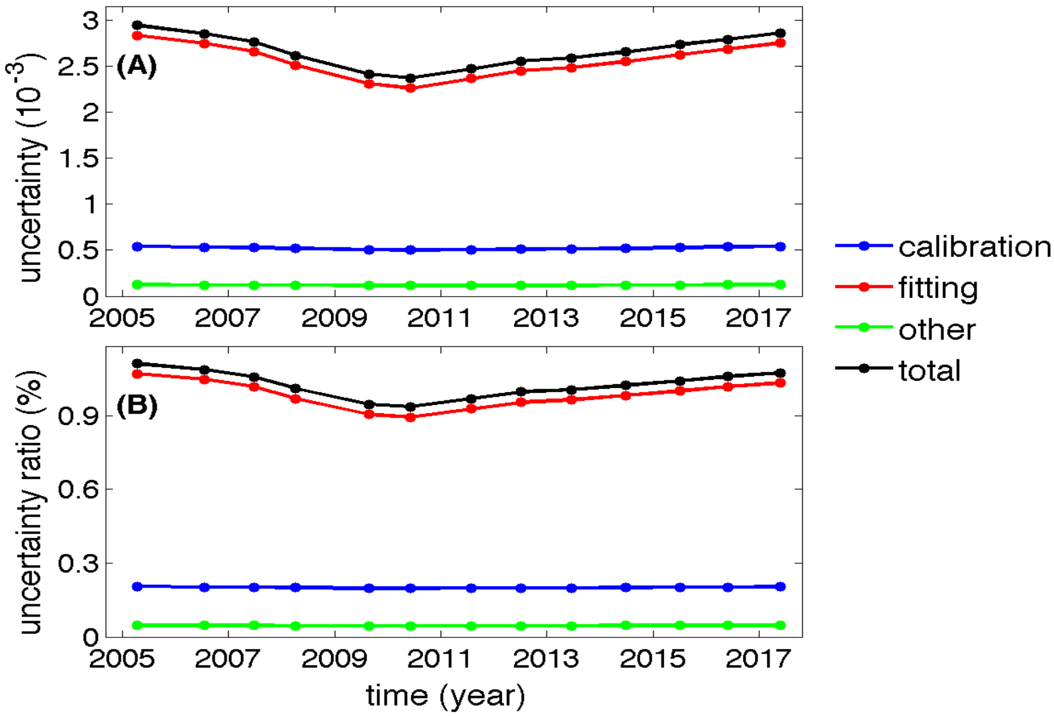

Figure S46. Uncertainties in the measurements of Titan's Bond albedo during the Cassini epoch. (A) Different uncertainties. (B) Uncertainty ratio. The uncertainty ratio is defined as the ratio between the uncertainties shown in panel A and Titan's Bond albedo (Fig. 1 in main text).

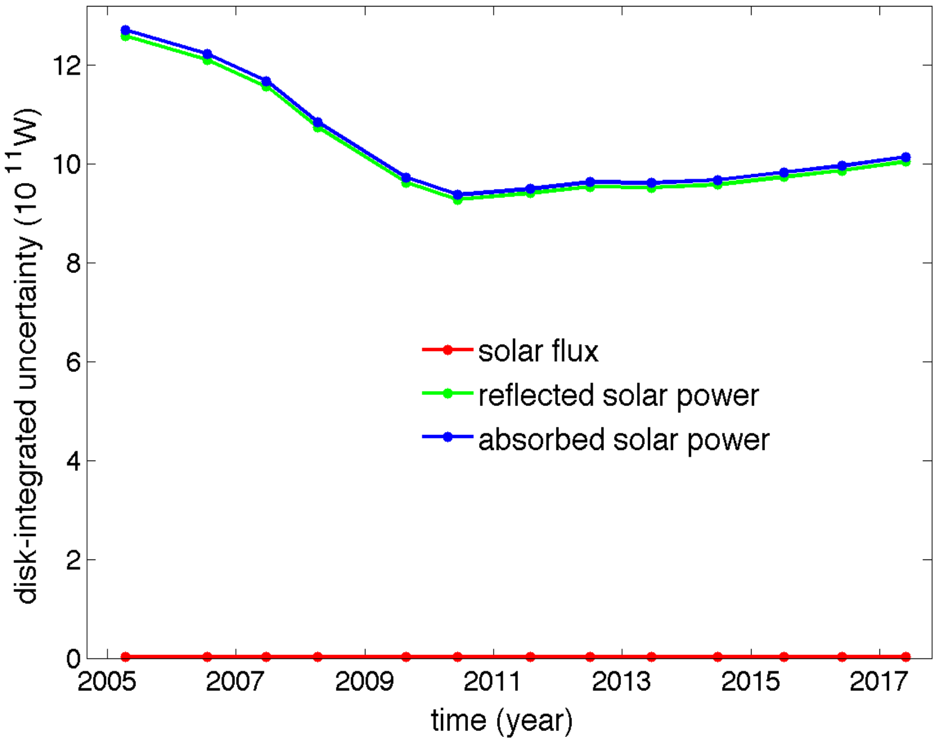

Figure S47. Uncertainties in the disk-integrated solar flux, reflected solar power, and absorbed solar power.

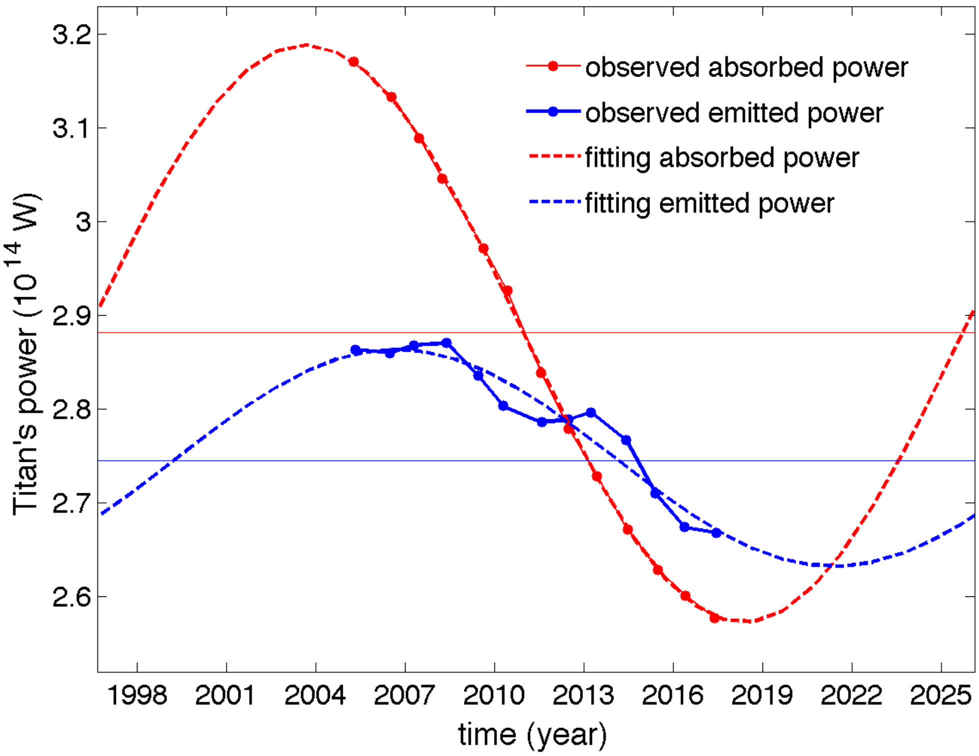

Figure S48. Fitted Titan's absorbed power and emitted power. The observed absorbed power and emitted power are fitted by sine functions with a fixed period – one Titan year (29.424 years). The red and blue horizontal lines represent the annual-mean absorbed power and emitted power, respectively.

Table S1. Observational Data Sets For Measuring Titan's Bond Albedo. The numbers in the parentheses are observational wavelengths and times. The full names of the abbreviations in the table are introduced as below. The ISS, VIMS, and UVIS are three instruments on the Cassini spacecraft. They are Imaging Science Sub-system (ISS), the Visual and Infrared Mapping Spectrometers (VIMS), and Ultraviolet Imaging Spectrograph (UVIS), respectively. The SEE, SORCE, and ASTM are three data sets for the solar spectral irradiance (SSI). They are the Solar EUV Experiment (SEE), the Solar Radiation and Climate Experiment (SORCE), and the American Society for Testing and Materials (ASTM), respectively. The Pioneer 11/IPP represents the Imaging Photopolarimeter (IPP) on the spacecraft Pioneer 11, whose observations were used to measure the phase function of Titan's albedo in a previous study. The HST/FOS and ESO stand for the Faint Object Spectrograph (FOS) of the Hubble Space Telescope (HST) and the European Southern Observatory (ESO), respectively. Their observations also provide the albedo spectra of Titan (see sections "Summary of Observational Data Sets" and "Supplementary Observations and Data" for more details and references).

Variable	Cassini Observations	Other Observations
solar spectral irradiance (SSI)		SEE (0-200nm, 2004-2017), SORCE (200-2400 nm, 2004-2017), ASTM (2400-4000 nm, climatology), and blackbody spectrum (4000-6000 nm)
phase function	ISS (264-939 nm, 2004-2017) and VIMS (350-5131 nm, 2004-2017)	Pioneer 11/IPP (452 nm (blue) and 648 nm (red), 1979).
spectral observations	ISS (264-939 nm, 2004-2017), VIMS (350-5131 nm, 2004-2017), and UVIS (150-190 nm, 2004).	HST/FOS (190-305 nm, 1991 and 1992) and ESO (305-1050 nm, 1993 and 1995)